Flicker Emission of Distributed Wind Power: Analysis and Mitigation Solutions

Moataz Ammar

Department of Electrical and Computer Engineering
McGill University
Montreal, Canada

August 2014

A thesis submitted to McGill University in partial fulfillment of the requirements for the degree of Doctor of Philosophy in Electrical Engineering

Abstract

The objective of this thesis is to analyze and provide solutions to the voltage flicker problem seen upon the connection of wind generators to distribution grids of low short-circuit levels and/or low reactance-to-resistance ratios (X/R ratios). The aim of this work is to mitigate the negative impact on distribution networks power quality and allow for increased penetration of wind power at the distribution level. In this thesis, control schemes for the active and reactive power flows at the wind generator bus of connection as well as planning decisions that can be made by the distribution networks operators are proposed to alleviate the voltage fluctuations impact of the intermittent resource of electric power. More specifically, the following is proposed: a modification to conventional reactive power control schemes in order to treat voltage flicker independent of the steady-state voltage level, and allow for flicker mitigation under injection of reactive power at the wind generators side; the use of a short-term energy storage system at the wind generators bus of connection, the sizing of the energy storage system is based on both the wind speed and the wind turbulence intensity at the installation site, and the control and management of the storage system are tailored to the frequency band of voltage flicker; and finally, network-based planning solutions that increase the connection point flicker suppression capacity. All the proposed solutions are studied from the flicker impact perspective and conclusions are drawn for their effectiveness in light of the given connection point characteristics and size of installed wind power. Sample results for all the proposed schemes are reproduced on a distribution-network model in a real-time simulation platform for verification purposes.

Résumé

L'objectif de cette thèse est d'analyser et de proposer des solutions au problème de papillotement présent au point de raccordement des parcs éoliens connectés à des réseaux de distribution caractérisés par de faibles niveaux de court-circuit et/ou de faibles rapports réactance à résistance (taux X/R). Le but de ce travail est de réduire l'impact négatif sur la qualité de l'onde et d'augmenter le taux de pénétration de la production d'énergie éolienne au niveau de la distribution. Dans cette thèse, des systèmes de contrôle pour régler la puissance active et réactive au point de raccordement du parc éolien ainsi que des approches à la planification des réseaux sont proposés afin d'atténuer les fluctuations de tension causées par cette source d'énergie électrique intermittente. Plus précisément, ce qui suit est proposé: une modification dans les systèmes de contrôle conventionnels de la puissance réactive afin de gérer l'amplitude du papillotement séparément du niveau de la tension en régime permanent et d'atténuer le papillotement lorsque les éoliennes injectent la puissance réactive; l'utilisation d'un système de stockage d'énergie à court terme au point de raccordement du parc éolien, dont le dimensionnement est basé sur la vitesse du vent et l'intensité de sa turbulence sur le site et son système de contrôle est basé sur la bande de fréquence correspondant au papillotement; enfin, des solutions au niveau de la planification du réseau modifiant des éléments qui permettent de changer ses caractéristiques au point de raccordement afin de réduire l'impact du papillotement. Toutes les solutions proposées sont étudiées du point de vue du niveau de papillotement et des conclusions sont tirées quant à leur efficacité. Un échantillon des résultats est reproduit par un modèle d'un réseau de distribution modélisé sur un simulateur en temps réel aux fins de vérification.

Acknowledgements

I would like to express my sincere gratitude to Prof. Géza Joós for his supervision of this thesis and to the NSERC for the financial support provided through the Wind Energy Strategic Network (WESNet).

Special thanks go to all my PhD supervisory committee members: Prof. Benoit Boulet, Prof. Luiz A.C. Lopes and Prof. Francois Bouffard.

I would also like to thank Philippe Venne of Hydro Québec Distribution for his technical advice and all members of the power group (faculty, students and researchers) and the staff of the Department of Electrical and Computer Engineering at McGill for their help and cooperation during my time at McGill.

Finally, I would like to thank my parents, Prof. Dr. Elsayed Ammar and Prof. Dr. Ahdab Elmorshedy, for the values they have instilled into me and my brothers and for their everlasting support along the years, and my brothers for their continuous help and motivation.

Contents

1 Introduction **5**

1.1 Background 5

1.1.1 DG Impact on Distribution Networks 6

1.1.2 Voltage Quality Complications 7

1.1.3 Current Challenges to Distributed Wind Power 7

1.2 Problem Definition 8

1.2.1 Reactive Power Control 8

1.2.2 Active Power Control 9

1.2.3 Network-Based Planning Solutions 9

1.3 Thesis Statement 10

1.4 Literature Review 10

1.4.1 Terminology 10

1.4.2 Flicker Impact and Customer Complaints 11

1.4.3 Flicker Mitigation by Reactive Power Control 11

1.4.4 Flicker Mitigation by Active Power Control 12

1.5 Thesis Contributions 13

1.6 Thesis Summary 13

2 Power System Modeling and Flicker Metrology **15**

2.1 Introduction 15

2.2 Wind Power Flicker Emission 15

2.2.1 WG Topology 16

2.2.2 Network Characteristics 17

2.2.3 Site/Farm Characteristics 18

2.3 Test Power Systems 18

2.3.1 Simplified Network Equivalent 19
2.3.2 Detailed Distribution Network 20
2.4 Wind-Turbine-Generator Modeling 21
2.4.1 Operating Approach of the Wind Turbine 22
2.4.2 Mechanical Model 25
2.4.3 Wind Resource Data 25
2.4.4 Electric Generator Control Modeling 26
2.5 Wind Power Flicker Measurement 27
2.5.1 IEC Flickermeter Modeling 28
2.5.2 Verification of the Conglomerate Power System Setup 29
2.6 Conclusion 31

3 Impact of WGs Reactive Power Behavior on Flicker Emission 32
3.1 Introduction 32
3.2 Fixed Power Factor Control 34
3.3 Voltage Control 40
3.4 Fixed Reactive Power Control 41
3.5 Mitigation Impairment 45
3.6 Decoupled Reactive Power/Variable Power Factor Operation 46
3.6.1 Simplified Network Equivalent 48
3.6.2 Detailed Distribution Network Case Study 50
3.7 Conclusion 53

4 A Short-Term Energy Storage System for Wind Power Flicker Mitigation 54
4.1 Introduction 54
4.2 Storage System Configuration 55
4.2.1 Centralized vs. Distributed ESS Topology 56
4.2.2 AC/DC Voltage Source Converter (VSC) 56
4.2.3 DC/DC Converter 57
4.3 Proposed Storage Sizing Methodology 58
4.3.1 ESS Sizing Requirements 58
4.3.2 Power Sizing 60
4.3.3 Energy Sizing 62

4.4 Storage Unit Flicker Mitigation and Management Control Algorithm . . 63
4.4.1 Current Control Loop 63
4.4.2 Power Control Loop 65
4.4.3 Controller Limits and Design Procedure 69
4.5 Simulation Results 70
4.5.1 Simplified Network/ Design Example (Simulations 1 and Simulations 2) 70
4.5.2 Detailed Distribution Network (Simulations 3) 82
4.6 Conclusion 86

5 Verification of Real-Time Performance and Flicker Mitigation Planning Solutions 87
5.1 Introduction 87
5.2 Real-Time Simulation Models 88
5.3 Real-Time Simulations Results of Chapter 3 and Chapter 4 Control Schemes 89
5.3.1 Real-Time Simulations Results of Investigated Mitigation Approaches 92
5.3.2 Real-Time Simulations Results of the ESS Control Algorithm . . 93
5.3.3 Real-Time Simulations Results of the Network Flicker Profile with the ESS 93
5.4 Mitigation Planning solutions 95
5.4.1 Stipulated Bandwidth of the WG Voltage Controller 95
5.4.2 MV/HV Transformer Size Increase 96
5.4.3 Two MV/HV Transformers in Parallel 97
5.4.4 Distribution Feeder Series Compensation 99
5.4.5 Change of Connection Point 99
5.5 Conclusion 101

6 Conclusions and Future Work 102
6.1 Summary 102
6.2 Conclusions 103
6.2.1 Impact of Reactive Power Control on Flicker Emission 103
6.2.2 Impact of an ESS on Flicker Emission 103
6.2.3 Real-Time Simulations 104
6.2.4 Wind Farm Planning Solutions 105

6.3 Recommendations for Future Work 105

A Wind Speed Data **107**

B Tower Shadow and Wind Shear Mathematical Model **109**

C Sample Results on the Full-Converter Synchronous Generator **111**

D Electric Generator Control **113**

D.0.1 DFIG 113

D.0.2 Full-Converter Synchronous Machine WG 117

E DFIG Rotor-Side Converter Control **120**

F IEC Flickermeter Details **123**

G IEC Flickermeter Model Validation **127**

H Standard Flicker Limits and Grid Codes **131**

H.0.3 Wind Farm Flicker Limit Allocation 132

I Grid-Integration Parametric Studies **135**

J Publications **139**

List of Tables

2.1 Simplified Network Test Cases 20

3.1 Pst Values Under Test Scenarios 51
3.2 Pst Values Under Wind Power Load Interaction 53

4.1 Storage System Parameters 71

B.1 Assumed Wind Turbine Parameters 110

F.1 Flickermeter Filters Constants 124

G.1 Flickermeter Response Characteristics Tests 128
G.2 Tests of Classifier and Statistical Evaluation 130

H.1 Flicker Compatibility Levels 132
H.2 Emission Limits (Individual Wind Farm) 132
H.3 Emission Limits in Sweden 132
H.4 Emission Limits in Denmark 133
H.5 Emission Limits in France 133

List of Figures

1.1 Interconnection of a distributed generator to a distribution network . . . 6

2.1 WG topologies . . . 16
2.2 Effect of wind turbines size and number on flicker emission. . . . 18
2.3 Network model as per IEC standard on WG power quality studies. . . . 20
2.4 Detalied 25 kV test distribution network layout. . . . 21
2.5 Power coefficient vs. pitch angle and tip speed ratio. . . . 23
2.6 $P - \omega$ characteristics of the WG (2 MW DFIG unit). . . . 24
2.7 Pitch control system. . . . 24
2.8 Wind speed data . . . 26
2.9 Wind-turbine-generator control sequence. . . . 27
2.10 Conventional flicker curves . . . 28
2.11 Pst as a function of wind speed and turbulence intensity at SCCR of 15 and X/R ratio of 0.52, 2 MW DFIG. . . . 30
2.12 Pst as a function of SCCR and X/R ratio at wind speed average of 10 m/s and turbulence intensity of 15 %, 2 MW DFIG. . . . 30

3.1 Simplified single-line diagram. . . . 33
3.2 Fixed power factor control. . . . 35
3.3 Pst vs. SCCR, unity power factor. . . . 36
3.4 Pst vs. SCCR, lagging power factor . . . 37
3.5 Flicker mitigation requirement (power factor vs. X/R ratio). . . . 39
3.6 Voltage control droop curve. . . . 40
3.7 Voltage control by droop characteristics. . . . 40
3.8 Pst vs. SCCR, voltage control. . . . 41
3.9 Reactive power consumption at varying SCCR for X/R=0.052 (voltage control). . . . 42

3.10 *Pst* vs. SCCR, fixed reactive power control 43
3.11 *Pst* as a function of leading power factor at an SCCR of 10. 44
3.12 VRMS as a function of leading power factor 45
3.13 Bode plot, decoupled variable power factor reactive power control. 47
3.14 Decoupled variable power factor reactive power control scheme. 47
3.15 Filtered active power reference components 48
3.16 Decoupled reactive power control, unity operation 49
3.17 Decoupled reactive power control, 0.95 lagging operation 50
3.18 RMS voltage at the PCC, reactive power injection and farm rating of 4 MW. 52
3.19 RMS voltage at the PCC, zero steady-state reactive power exchange and farm rating of 6 MW. 52
3.20 RMS voltage at the PCC, reactive power absorption and farm rating of 10 MW. 52

4.1 Employed ESS configuration. 56
4.2 ESS VSC control. 57
4.3 Impact of the 3p torque oscillations on output power of a WG 59
4.4 Proposed storage unit power rating as a function of wind speed average and wind turbulence intensity (2 MW DFIG). 62
4.5 Proposed storage unit energy rating as a function of wind speed average and wind turbulence intensity (2 MW DFIG). 63
4.6 Current control loop. 65
4.7 Power control loop. 68
4.8 Storage system control small-signal model. 68
4.9 Bode plot of the current control loop 73
4.10 Bode plot of the power control loop 74
4.11 Small-signal model response 75
4.12 ESS operation (Supercapacitor side) 78
4.13 ESS operation (VSC side) 79
4.14 Power spectral density of active power components. 80
4.15 Flicker measurement at the PCC with and without the ESS. 80
4.16 *Pst* sensitivity to energy rating 81
4.17 *Pst* sensitivity to management frame length 82

4.18 Pst values vs. wind power capacity at Bus 16 of the detailed network. . . 83
4.19 Vector diagram of voltage changes after active power injection. 85
4.20 Short-term profile of Bus 16 RMS voltage under different flicker mitigation approaches (6 MW rating scenario). 85

5.1 Wind farm distribution network segregation in RT-LAB (ESS case). . . . 90
5.2 Wind farm distribution network segregation in RT-LAB (Reactive power control cases). 91
5.3 Sample Pst values and cases for real-time simulations. 92
5.4 IFL and Pst (real-time simulations, 6 MW scenario). 93
5.5 ESS control real-time performance 94
5.6 Network flicker profile with the ESS (real-time simulation, 6 MW rating scenario). 94
5.7 Voltage control droop curve for different permissible bandwidths of voltage changes. 95
5.8 Pst vs. the bandwidth of the wind farm voltage controller. 96
5.9 Pst values across the network buses for different MV/HV transformer MVA ratings. 97
5.10 Typical MV/HV substation transformers configuration. 98
5.11 Pst values across the network buses for two identical MV/HV substation transformers of 15 MVA operating in parallel. 98
5.12 Pst values across the network buses for different levels of series reactive compensation. 100
5.13 Pst values across the network buses for different connection points. . . . 100

A.1 Weibull-distributed 10-minute wind speed profile 108

C.1 Pst vs. SCCR, full-converter synchronous generator 112
C.2 IFL, full-converter synchronous generator 112

D.1 DFIG control schematic. 114
D.2 Voltage source converter. 115
D.3 Grid-side converter control block diagram. 116
D.4 Rotor-side converter control block diagram. 117
D.5 Overall performance of the DFIG unit 118
D.6 Machine-side converter, full-converter synchronous generator. 118

D.7 Machine-side control, full-converter synchronous generator. 119

F.1 IEC flickermeter block diagram. 126

H.1 Flicker Allocation Pie 134

I.1 Effect of wind turbines spacing on equivalent wind speed and turbulence intensity 136

I.2 Active power generation for a 10 MW wind farm (lumped vs. spaced wind power production). 137

I.3 Pst values for lumped and spaced wind power production. 137

I.4 Wind power production under varying levels of turbulence intensity. . . . 137

I.5 Pst values at the connection bus as the turbulence intensity changed. . . 138

List of Acronyms

AC	Alternating Current
DC	Direct Current
DFIG	Doubly Fed Induction Generator
DG	Distributed Generation
ESS	Energy Storage System
ESR	Equivalent Series Resistance
FACTS	Flexible AC Transmission System
FS	Fixed Speed
GS	Grid Side
HV	High Voltage
IEC	International Electrotechnical Commission
IEEE	Institute of Electrical and Electronics Engineers
IFL	Instantaneous Flicker Level
MPPT	Maximum Power Point Tracking
MV	Medium Voltage
OLTC	On-Load Tap Changer
PCC	Point of Common Coupling
PI	Proportional-Integral
PLL	Phase-Locked Loop
PSD	Power Spectral Density
PWM	Pulse Width Modulation
RMS	Root Mean Square
RS	Rotor Side
SCCR	Short Circuit Capacity Ratio
SoC	State of Charge
STATCOM	Static Synchronous Compensator
SVC	Static Var Compensator
VS	Variable Speed
VSC	Voltage Source Converter
WG	Wind Generator

List of Symbols

Pst	Short-Term Flicker Index
Plt	Long-Term Flicker Index
Z_l	Equivalent Network Impedance
MVA_{sc}	Short-Circuit Level at the Point of Connection
R	Resistance
X	Reactance
P	Active Power
Q	Reactive Power
I	Line Current
V	Line Voltage
A	Area Swept by the Wind Turbine Blades
ρ	Air Density
C_p	Power Coefficient
v	Wind Speed
λ	Tip-Speed Ratio
β	Blade Pitch Angle
L	Inductance
r	Turbine Blade Radius
ω	Rotational Speed
Λ	Flux
i	Phase Current
θ	Angular Position
δ	Voltage Angle between Sending and Receiving Buses
ΔV	Difference in Voltage Magnitude between Sending and Receiving Buses
ϕ	Generator Phase Angle
V_r	Voltage Reference for Droop Curve
Q_r	Reactive Power Consumption at Voltage Reference for Droop Curve
k	Voltage Droop Coefficient
τ	Filter Time Constant
t_{ur}	Turbulence Intensity

σ	Standard Deviation
C	Capacitance
D	Duty Cycle
Δd	Small-Signal Duty Cycle
Δi	Small-Signal Current
Δv	Small-Signal Voltage

Subscripts

mes	Measured Value
$scmes$	Supercapacitor Storage Measured Value
$rated$	Rated Value
opt	Optimal value
a	Phase a
b	Phase b
c	Phase c
gs	Grid Side
d	Direct-Axis
q	Quadrature-Axis
s	Stator
r	Rotor
ref	Reference
dc	DC Link
max	Maximum
min	Minimum
fil	Filter
w	Wind Power
sc	Supercapacitor
res	Rated Energy Storage
se	Sending End
$char - disch$	Charging/Discharging

List of Definitions

Distribution Network Strength	A term that designates a distribution network connection point immunity to voltage fluctuations resulting from the interconnection of an electric facility.
Grid Code	A document detailing the technical requirements that a facility (load or generator) must meet in order to be connected to the integrated electric power system. The grid code ensures the safe and proper operation of the integrated electric power system.
Wind Turbulence Intensity	A term that designates the severity of deviations of a wind speed profile from its average wind speed value.
WG Leading Power Factor	A WG control mode in which the flow of reactive power is from the power system to the WG and the WG acts as a reactive power sink.
WG Lagging Power Factor	A WG control mode in which the flow of reactive power is from the WG to the power system and the WG acts as a reactive power source.
3p Oscillations	A term that designates the cyclic pulsations that occur in three-bladed turbines (at three times the rotor frequency) due to the tower shadow and wind shear effects.

Chapter 1

Introduction

1.1 Background

Recently and with the promotion and increased adoption of Distributed Generation (DG), power quality concerns became increasingly important to electric utilities, standing in many cases as an obstacle hampering the integration of renewable energy generators to distribution networks. DG refers to small-scale power generation that – and in contrast to conventional large-scale centralized generation – is connected to low-voltage or medium-voltage distribution networks in the vicinity of the consumers of electric energy. The introduction of DG in the generation mix was motivated by conceptual and environmental concerns such as the minimization of transmission losses, ease of integration in remote rural areas and sought increased penetration of renewable-energy-based power generation [1] (a significant share of DG [2]). Yet, and as expected, new concerns emanate from the advent of new trends and strategies. The increase in the number and size of DG projects resulted in a parallel increase in the number of WGs connected to distribution grids (wind energy has the biggest share of power generation from renewable sources, reaching a total worldwide installed capacity of 360 GW in 2014 [3]). The increased adoption of wind power at the distribution level was marked by utilities and distribution network operators concerns about the repercussions of the fluctuant source of power and the foreseen deterioration in voltage quality upon the integration of WGs.

1.1.1 DG Impact on Distribution Networks

The introduction of DG was accompanied by a spectrum of distribution network operational complications and deterioration in the quality of supplied power [4, 5, 6, 7]. This was in part due to the nature of distribution networks, that are generally of a resistive nature and low-short-circuit-level connection points when compared to the mostly reactive high-short-circuit-level transmission systems, and in part due to the original design of distribution networks that assumed a unidirectional flow of power. The unidirectional topology of power flow from the grid (transmission/subtrasmission levels) to the electricity consumers was then altered to an unanticipated situation of reverse power flow from the consumer-end backwards to the grid. Figure 1.1 shows the typical configuration of a distribution network with and without the interconnection of DG.

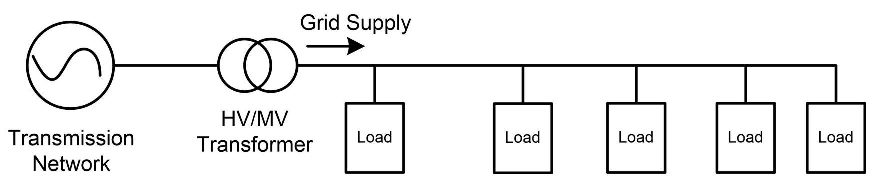

(a)

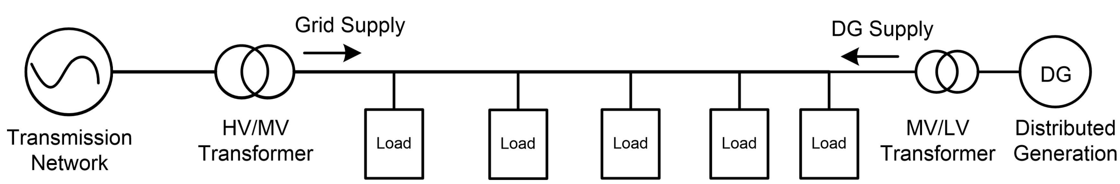

(b)

Figure 1.1: Interconnection of a distributed generator to a distribution network: a) unidirectional flow of power, b) introduction of DG and bidirectional flow of power.

More specifically, the operational problems could be classified as follows: 1) problems due to the electric current flowing in the distribution network being a combination of the grid currents and the connected DG currents (problems from a protection switchgear perspective) [4], 2) problems due to the altered voltage profile over the feeder as a result of the injection of active power (problems as viewed from the On-Load Tap-Changers

(OLTCs) and other voltage regulation equipment perspective) [5], and finally 3) problems from a power quality perspective under the integration of inverter-based units and generators with intermittent supply such as wind generators (WGs) and photovoltaic panels [6].

1.1.2 Voltage Quality Complications

The presence of intermittent-resource power generation accounts for fluctuations in the voltage waveforms that become dependent, as viewed on a global network level, on both the fluctuations originating at the fluctuating load buses as well as the fluctuations originating at the distributed generators buses. Therefore, upon the integration of wind power in the form of DG, the host networks are prone to voltage quality problems that negatively impact the utilization of electric power and its consumers. Wind power fluctuations rarely constituted a voltage quality problem at transmission levels as connections were made at relatively strong Points of Common Coupling (PCCs) with relative high short-circuit capacities and grid reactance-to-resistance ratios (X/R ratios). Conversely, with the increase in the number and size of distributed WGs and connection to medium-voltage levels below 40 kV, the fluctuations account for more serious problems and their impact becomes more pronounced and of increasing concern to electric utilities [8, 9].

1.1.3 Current Challenges to Distributed Wind Power

In order to connect wind power to distribution networks, operation-binding grid codes have to be satisfied [10], imposing a limitation on the size of a distributed wind farm should the standards be violated. This results in impaired penetration of wind power in distribution networks. The power quality limits have to be respected by the WGs, which can be achieved either by a fit-and-forget approach by simply restricting the size of wind power penetration or by adopting supplementary and modified machine controls to facilitate the integration with less hampering of the prospective size of penetration. The resulting voltage fluctuations associated with wind power generation – and as treated by grid codes – can be seen in two frames: 1) slow fluctuations that alter the steady-state voltage level of the distribution network, and 2) fast fluctuations around the steady-state voltage level that result in flicker emission. Both problems constitute main concerns to utilities in the planning phase of a distributed wind power project. On one hand not to violate the steady-state voltage limits and compromise the life-time of the OLTCs and on the other hand to avoid flicker-triggered customer complaints. The short-term fluctuations of wind power and the resulting flicker emission are the main subject treated in this work.

In order to confront such voltage quality challenges and meet current grid codes, the behavior of the flicker emission of WGs under the different possible machine control approaches has to be identified and new control schemes need to be proposed to overcome the limitations of the conventional control schemes. This would not only help relieve utilities from flicker-related customer complaints but would also relax the restrictions on the permissible amount of wind power penetration in a distribution network and allow for more flexibility with the choice of connection point.

1.2 Problem Definition

Wind power interconnection at the distribution level introduces voltage flicker problems that impose size restrictions on the amount of wind power penetration in distribution networks and negatively impact the customers on the same distribution feeder. Solutions to the problem are typically viewed from two perspectives, a reactive power control perspective and an active power control perspective. It also has to be noted that network upgrading/reinforcement and wind farm planning decisions are potential solutions to the voltage flicker problem whenever viable and implementable.

1.2.1 Reactive Power Control

From a reactive power control perspective, contemporary wind turbine installations are of the Variable-Speed (VS) type and boast the capability of adjusting their reactive power consumption through different possible converter control modes. Those VS WG are generally required to be capable of both absorbing and injecting reactive power based on the voltage level at the connection point. Flicker mitigation is shown in previous works to be achievable through absorption of reactive power at the WG bus by means of the machine converters control or by the use of STATCOMs at the connection point. Those techniques do not necessarily present a feasible solution for a given wind power interconnection point and have remarkable limitations. The use of STATCOMs is cost-prohibitive in distribution networks and the reactive power absorption requirement for flicker mitigation increases as the network X/R ratio decreases, placing a burden on the network reactive sources as well as limiting the reactive power capability of the machine to leading power factor operation. It is thus necessary to delineate the flicker behavior under all possible reactive power control modes of the WG in order to conceive control solutions that overcome the shortcomings of the current mitigation approaches and allow for more flexibility with the machine reactive power behavior by not having it dictated by the flicker emission concern.

1.2.2 Active Power Control

From an active power control perspective, the flicker emission of a WG theoretically vanishes if a means of eradicating the flicker-producing wind power network injections is provided. Active power control can be achieved either by the machine controls, if operated in a manner that counteracts the flicker-producing changes, or by an energy buffer (storage unit) such that a smoothing stage exists between the wind power generation stage and the network injection stage. The former implies a deviation from the Maximum Power Point Tracking (MPPT) algorithm while the latter implies an increase in incurred costs. For the nonce, energy storage units were primarily investigated for purposes of increasing the wind power capacity at the PCC with respect to the steady-state voltage rise. Such investigations have proved economically futile on many occasions due the massive increase in capital cost associated with the long-term storage units and the low price of energy in the intended storage periods (high generation and low load conditions) rendering the cost of implementation a major concern [11]. Yet, if the storage used is of short-term nature and sized only for a proportion of the output power spectrum (fluctuations amounting for the flicker-emission), energy storage may then present a feasible solution to meet the grid codes [12], especially in cases where reactive power control approaches are impaired.

1.2.3 Network-Based Planning Solutions

Flicker mitigation planning solutions can also be adopted by distribution network operators. More specifically, the distribution network operator could opt for any of the following: a change of the bandwidth of the direct voltage controller stipulated in the operative grid code and implemented by the distributed wind farm, MV/HV substation transformers upgrading, series line compensation, or as a last resort, the change of the wind farm connection point.

1.3 Thesis Statement

The thesis first defines the necessary factors to be taken into consideration in order to carry out a sound flicker study. The thesis then analyzes the sensitivity of the flicker emissions to the different possible WG reactive power control modes and yields recommendations on the suitability of each control mode for flicker mitigation based on the connection network characteristics and utility regulations. Based on the ascertained limitations of conventional reactive power control in flicker mitigation, solutions are proposed in the form of reactive and active power controls. The solutions are viewed in terms of an extensive range of connection point characteristics, and emulation of real-life scenarios by testing the proposed solutions on a detailed real-life 25 kV distribution feeder for verification and completeness purposes. The following tools have been used to produce the results documented in this thesis:

1. Distribution system analysis software CYMDIST (detailed 25 kV distribution network parameters and power flow studies).
2. MATLAB script coding (control design, small-signal analysis, spectral analysis, parameter loading and sequential simulations programming).
3. Power system time-domain simulations software (MATLAB SimPowerSystems toolbox).
4. Real-time simulation software environment (RT-LAB professional).
5. Real-time simulator (OPAL-RT Technologies).

1.4 Literature Review

1.4.1 Terminology

Voltage flicker is defined by IEEE standard 1453-2011 [13] as voltage fluctuations on the electric power system that give rise to noticeable illumination changes. Such voltage fluctuations are the result of various possible incidents that include the switching of electrical appliances, connection of electric motors with variable loads, and recently the interconnection of DG [14]. In the context of wind power, voltage flicker is a result of the generated active power fluctuations that occur in frequencies in the range producing light flicker.

1.4.2 Flicker Impact and Customer Complaints

Utilities acknowledge the presence of flicker problems upon customer complaints, that are reported to be predominantly flicker-related in distribution networks [15, 16]. As the malfunction of lighting installations is the most perceivable by customers as a flicker-induced problem, voltage flicker is assessed based on its impact on lighting equipment. The sensitivity of lighting equipment to voltage changes is quite variable based on the lamp characteristics. This implies that the same flicker levels on two different networks may or may not lead to corresponding customer complaints based on the nature of the lighting installations on both networks. The impact of voltage flicker on different types of lamp technologies is investigated in [17]. The results show that different lamp technologies have different degrees of sensitivity to dynamic voltage changes and over different frequency ranges. The human eye is shown in [18] to be most sensitive to changes in incandescent lamps and least sensitive to fluorescent lamps.

1.4.3 Flicker Mitigation by Reactive Power Control

Flicker mitigation is conventionally achieved by reactive power compensation that is done locally at the PCC. This presents the general trend in mitigating wind power flicker problems in distribution networks. The reactive compensation manifests in two forms: 1) conventional flicker mitigation equipment suitable for Fixed-Speed (FS) and VS WGs, and 2) flicker mitigation specific to VS WGs. Both groups employ reactive power compensation to compensate the active power fluctuations. The former utilizes FACTS installations like STATCOMs and SVCs [19] while the latter utilizes the reactive power control capabilities of the power electronic interface in the VS WGs. The most widely adopted flicker mitigation scheme by FACTS installations is the STATCOM. The use of the STATCOM for flicker mitigation in a DFIG-based wind farm was studied in [20]. The results showed that the STATCOM is an effective means of mitigating wind power flicker severity irrespective of the wind speed average and size of the wind farm. Yet, STATCOMs may not present an economically feasible solution in distribution networks [21]. VS WGs have their own reactive power management capabilities by virtue of their embedded power electronic grid interface and can be operated in either of the following modes: 1) fixed power factor control mode, 2) terminal voltage control mode and 3) fixed reactive power control mode. Fixed power factor control is the conventional control scheme in which the WG maintains either a leading or a lagging fixed power factor over the entire range of operation. Conversely, in voltage control mode, the reactive power demand on the WG is determined by a measured voltage deviation from a reference voltage setpoint. Voltage control, however, is a less preferred option in distributed generation [22] due to the fact that it may interfere with the utility-imposed feeder voltage control mechanisms, typically OLTC operation [5]. The third option is to have the machine continuously inject or absorb a fixed amount of reactive power.

Reactive power control is reported to have flicker mitigating impacts in [23, 21, 24]. Yet, the flicker mitigation capacity of reactive power control is limited by the following, often overlooked, operational considerations: 1) the increase in reactive power requirement as the grid X/R ratio decreases, 2) system operators preference for a unity power factor and a minimum leading power factor of 0.95 [25, 26], 3) incapability of supplying reactive power to the grid due to the necessity of operation at a leading power factor or dedication of the machine reactive power control to flicker mitigation [27].

1.4.4 Flicker Mitigation by Active Power Control

As the impedance angle (X/R ratio) of a distribution network decreases, the flicker mitigation reactive power demand on the WG increases, to the extent that it either exceeds the rating of the WG power electronic converters or places an infeasible burden on the network reactive sources. In such situations, a different approach for flicker mitigation can be seen in the control of active power fluctuations. This can be done by eliminating the WG active power fluctuations responsible for the flicker emission. This was shown possible in VS full-converter synchronous generators by means of modified control of the machine converters and continuous adjustment of the DC link voltage reference [28, 29]. This approach would typically be limited by the size of the DC link capacitor and the corresponding permissible deviation from the voltage setpoint and involves a deviation from the MPPT algorithm. An alternative approach was proposed in [30], in which the pitch control scheme of the DFIG wind turbine was modified to counteract active power dips by maintaining a reserve margin for active power increase by the turbine blades. The flicker mitigation achieved through those approaches was shown partial due to active power smoothing targeting only a fraction of the flicker-producing fluctuations of the WGs.

1.5 Thesis Contributions

The work of this thesis contributes the following:

1. Identification of conventional reactive power control approaches feasibility, limitations and extent of use in flicker mitigation in distributed wind power, as viewed in terms of enforced grid codes and distribution networks X/R ratios.

2. Proposal of a flicker-range-based variable power factor reactive power control scheme as a flicker mitigation approach, making it possible to achieve flicker mitigation under injection of reactive power from the WG, as opposed to conventional necessity of reactive power absorption.

3. Proposal of a combined flicker control/storage management algorithm for a short-term supercapacitor-based ESS to allay the typical wind power short-term power quality concern of voltage flicker, and proposal of a short-term energy storage power sizing methodology based on average wind speed and turbulence intensity at the installation site.

1.6 Thesis Summary

The rest of this thesis is structured as follows:

Chapter 2 of the thesis provides insight into the modeling of the wind energy conversion schemes and test power systems employed to verify the results of the proposed methodologies and controls. Chapter 2 also details the standard flicker metrology recommended in both IEC and IEEE standards and adopted in the industry. The operation and proper behavior of the developed models are verified and the results are documented.

Chapter 3 investigates the flicker impacts of the different possible reactive power control schemes of a VS WG and proposes a control scheme that overcomes the shortcomings of those conventional approaches with respect to flicker mitigation.

Chapter 4 proposes power sizing, flicker control and storage management algorithms for a short-term energy storage unit (supercapacitor) for flicker mitigation purposes.

Chapter 4 also provides technical description and mathematical analysis for the obtained results in comparison to the reactive power control approaches presented in Chapter 3.

Chapter 5 features real-time simulation studies of the proposed controls, involving emulation of real-life wind farm/distribution network integration scenarios. The superior computational abilities of the real-time simulator are also utilized in testing various flicker mitigation planning solutions.

Chapter 6 provides a conclusion for the work presented in this thesis and reflects on the potential contributions that could serve as a continuation of the presented work.

Chapter 2

Power System Modeling and Flicker Metrology

2.1 Introduction

In this chapter, the nature of wind power flicker emission is explained by defining its sources, and the influence the turbine topology, the host network characteristics and the site considerations can have on aggravating the severity of the emission. The currently adopted flicker metrology is then explained and the test models on which the studies were performed are explained in detail.

2.2 Wind Power Flicker Emission

WGs deliver fluctuating output power due to the fluctuating nature of wind. The fluctuations in the output power will account for voltage flicker if they occur in the range of lamp sensitivity (0.05 to 35 Hz (230 V/50 Hz system) and 0.05 to 42 Hz (120 V/60 Hz system)). These fluctuations are due to wind speed changes, wind shear and tower shadow impacts at the turbine blades. With respect to flicker emission, wind power projects can be evaluated in terms of the following three main factors:

- WG topology
- network characteristics
- site/farm characteristics

The impact of each of those factors is described in the following subsections.

2.2.1 WG Topology

Wind power projects are first viewed in terms of the WG topology either FS or VS, Figure 2.1.

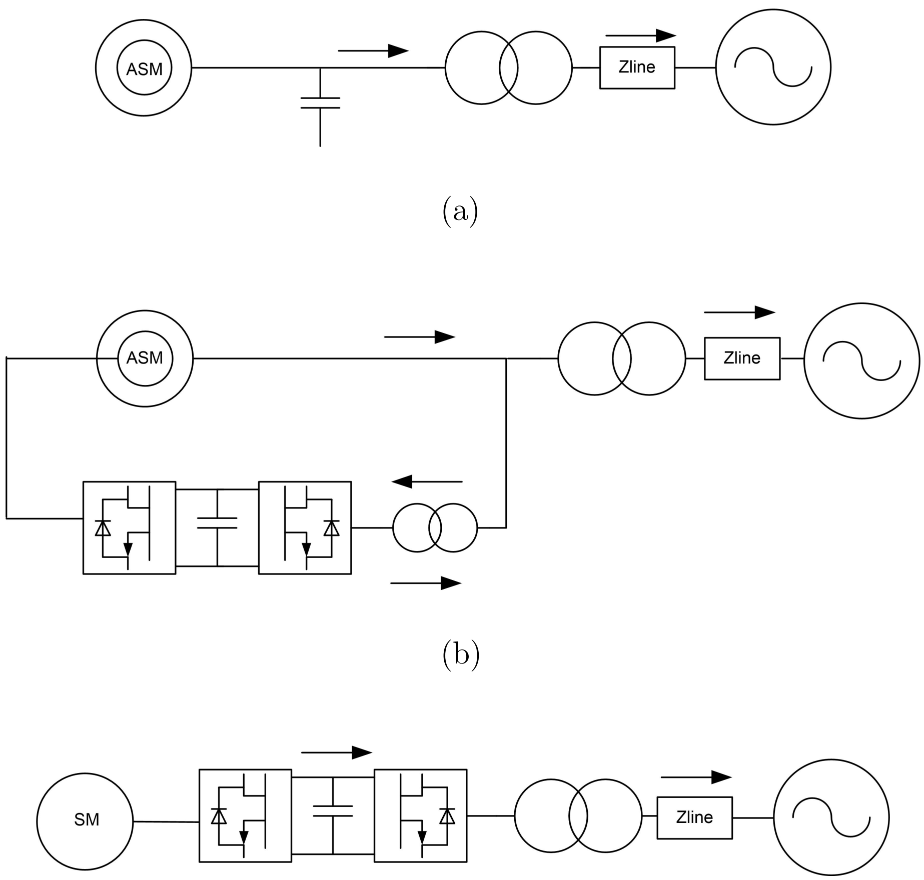

(c)

Figure 2.1: WG topologies: (a) fixed-speed induction generator, (b) variable-speed doubly-fed induction generator, (c) variable-speed synchronous generator.

For the same WG size, the flicker problem is highly aggravated with FS WGs that are known to have much higher flicker emissions than their VS peers [31]. The reduced flicker emission of VS WGs is attributed to the added ability of smoothing the machine torque oscillations. The presence of rotor speed control is claimed to highly suppress the 3p torque oscillations (0.5-1.5 Hz) bringing the tower shadow effect to marginal levels [32]. A comparison between FS and VS installations on a rural feeder (20 kV, 40 MVA PCC) shows that up to 50 % more wind power can be delivered at the same PCC with VS turbines without violating the power quality limits on the rural network [8]. Further detail on the construction of the different WG topologies can be found in [33].

2.2.2 Network Characteristics

For a given turbine topology, the emissions can then be viewed in the context of the following distribution network connection point characteristics:

- short-circuit capacity ratio (SCCR)
- network reactance-to-resistance ratio (X/R ratio)

Such characteristics determine the strength of the network or its ability to buffer the injected active power fluctuations. In other words, when the MV network is characterized by low short-circuit capacity at the PCC and relative high rating of wind power and/or low X/R ratio, the network is considered a weak network. Such networks are the most susceptible to wind-power-produced voltage flicker. Several studies were dedicated to investigate the dependability of the flicker trends on the above mentioned characteristics. For instance, in [31], the flicker emission of wind power installations is shown to increase steadily with an increase in the ratio of rated wind power to the short-circuit level at the PCC. While a study on a wind park connected to a grid of high wind power penetration shows that the effect of the X/R ratio or the grid impedance angle is very influential in determining the flicker severity, showing that an X/R ratio of 0.5 results in at least 5 times the flicker produced at an X/R ratio of 2 [34]. In [9], the authors investigate the impact of a wind power plant connection to a weak 11 kV residential feeder in Brazil. The network has 15 buses for potential wind power integration with short-circuit levels ranging from 32 MVA to 20 MVA. The study shows, that at all buses, the technical limitation on the amount of wind power penetration was primarily imposed by respecting the allowed flicker emissions.

2.2.3 Site/Farm Characteristics

Wind turbines produce higher flicker emissions with the increase in average wind speed in the range below farm rated output [23]. Accordingly, a site with an annual average of 10 m/s would have higher emissions than another with an average of 6 m/s. The number of turbines and the spacing between turbines are also factors in attenuating or aggravating the flicker emissions. For instance, if one turbine is used to produce the full rating of a 5 MW farm, the flicker emission at the same PCC would be attenuated with two spaced 2.5 MW turbines. This is a result of having the turbines undergo time-shifted wind speed profiles resulting in non-synchronizing power fluctuations and attenuating the resultant fluctuation in the total wind farm output. The effect of such grouping of wind turbines is reported to have an attenuating effect of $\sqrt{n}$, where n is the number of turbines [34, 35] and meaning that an assembly of n wind turbines of the same size would result in a flicker emission of $\sqrt{n}$ that of a single unit, Figure 2.2.

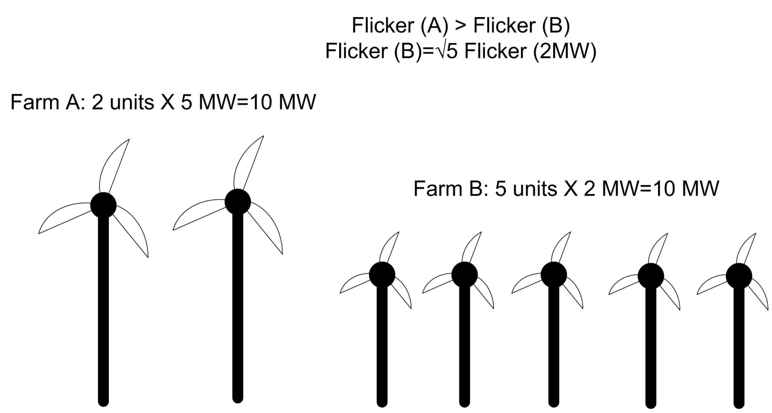

Figure 2.2: Effect of wind turbines size and number on flicker emission.

2.3 Test Power Systems

As seen in the previous section, it is evident that the flicker severity is highly dependent on the connection point characteristics in terms of both the short-circuit level and the equivalent X/R ratio. Accordingly, in order to perform sound flicker studies, a spectrum of such characteristics has to be accounted for. The work presented in this thesis is intended for MV distribution networks with typical low short-circuit levels at the point of connection and expected high penetration of wind power. Therefore, the test 25 kV distribution systems described below were chosen as the network models to encompass a wide spectrum of connection points characteristics, on which the proposed control schemes were verified.

2.3.1 Simplified Network Equivalent

Typical X/R ratios seen in 25 kV distribution networks were assumed in the studies and the SCCRs were chosen to represent situations where VS wind power is expected to account for considerable flicker contribution. The simplified test system consists of a grid impedance specified by the short-circuit level at the PCC and the given voltage level (25 kV). The values of the grid resistance and reactance were determined based on arbitrary MV X/R ratios, generating a family of connection point characteristics. The base WG unit used is of 2 MW rating and the SCCRs assumed are 15, 10, 7.5 and 5 representing 30, 20, 15 and 10 MVA short-circuit levels respectively. By simply substituting the short-circuit levels in (2.1), the corresponding values of the equivalent line impedance for all cases can be obtained, and from (2.2), the values of X and R for each corresponding X/R ratio are calculated. The test cases are summarized in Table 2.1.

$$Z_l = \frac{V^2}{MVA_{sc}} \tag{2.1}$$

$$R = \sqrt{Z_l^2 - (R\,ratio)^2} \quad , \quad ratio = \frac{X}{R} \tag{2.2}$$

$$R = \sqrt{\frac{Z_l^2}{1 + ratio^2}} \tag{2.3}$$

The test values of X and R are plugged into the network of Figure 2.3 which represents the standard IEC test network for flicker assessment [36]. The flicker assessment is carried out for the voltage waveform of $V_{PCC}(t)$ (at the PCC).

By configuring the above cases, a spectrum of connection point characteristics, representing a total of 16 test connection points, is employed to obtain the flicker trends under the investigated WGs operational control modes and proposed supplementary con-

Table 2.1: Simplified Network Test Cases

SCCR	Voltage Level (kV)	Test (X/R) Ratios
5	25	(0.52, 0.95, 1.8, 3.2)
7.5	25	(0.52, 0.95, 1.8, 3.2)
10	25	(0.52, 0.95, 1.8, 3.2)
15	25	(0.52, 0.95, 1.8, 3.2)

trol schemes.

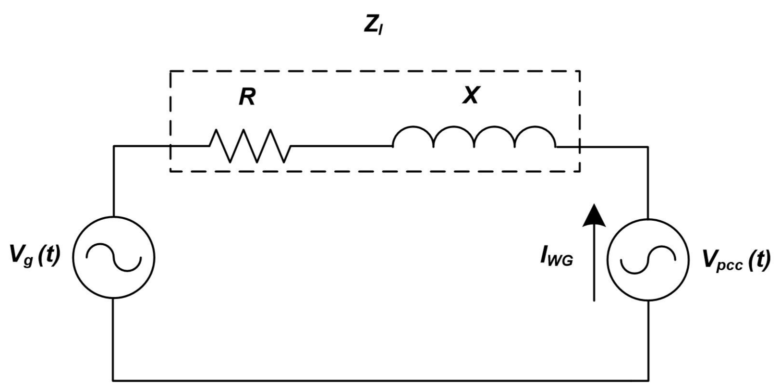

Figure 2.3: Network model as per IEC standard on WG power quality studies.

2.3.2 Detailed Distribution Network

A flicker-susceptible 25 kV distribution network is employed to reflect the work results on real-life scenarios of distributed wind power. The detailed network also allows the study of flicker measurements at different buses and lengths of a distribution network rather than just at the PCC. The peak network loading is 11.11 MW and 1.14 MVAR, a capacitor bank of 1.2 MVAR is present near the end of the network feeder for voltage support purposes. The network layout is shown in Figure 2.4. The network has 16 buses and three types of distribution conductors with a total length of 47.9 km. The dominant conductor over the feeder is of an X/R ratio of 3.4, a lateral of shorter sections has an X/R ratio of 1.3841 and finally a section of an X/R ratio of 0.899. The HV/MV transformer is of 15 MVA and has an X/R ratio of 10, the LV/MV transformers are identical and of 2.5 MVA and an X/R ratio of 10 each. Given that distributed wind farms are typically constructed in remote rural areas, the farthest and weakest point on the feeder was chosen to serve as a potential connection point for a MW-sized wind farm. The short-circuit level at the base test point of connection (Bus 16, Figure 2.4) is 29 MVA and the voltage level at the point of connection under peak load prior to wind power integration is 0.955 pu.

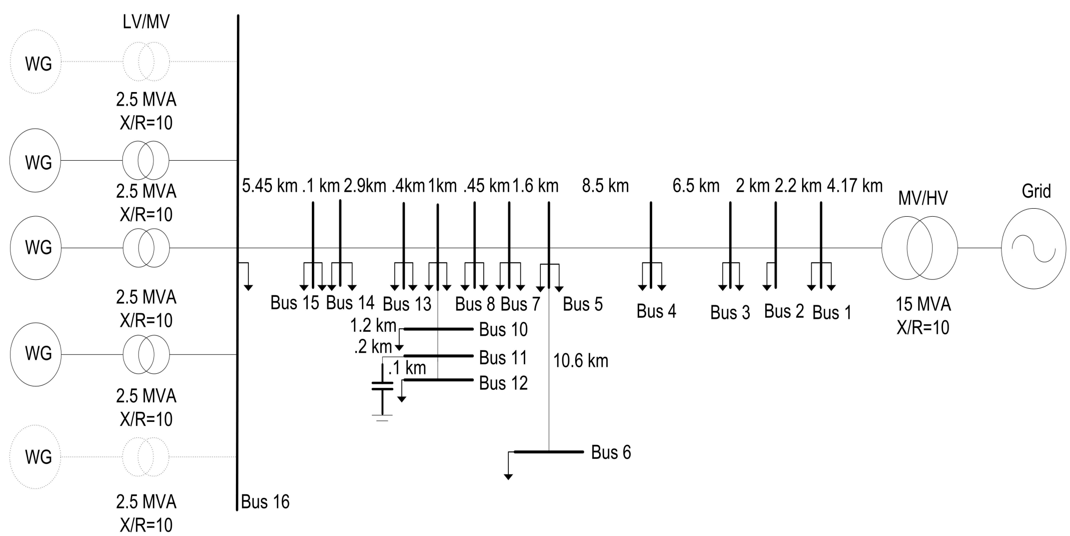

Figure 2.4: Detalied 25 kV test distribution network layout.

2.4 Wind-Turbine-Generator Modeling

The level of modeling required for studying the flicker impact of wind turbines can be studied in the frame of the following systems:

- operating approach of the wind turbine
- mechanical model structure
- wind resource data
- electric generator control modeling

2.4.1 Operating Approach of the Wind Turbine

The implementation of different approaches to achieve the MPPT operation is shown to have an impact on the frequency components of the output wind power spectrum and therefore the flicker emission [37, 38]. Prior knowledge of the MPPT control approach of a VS wind generator would be an asset for accurate evaluation of its flicker emission. Yet, any MPPT approach would be suitable for studying the efficiency of flicker mitigation controls. The machine model, as implemented, adheres to an MPPT curve by continuously adjusting the tip speed ratio λ to achieve the maximum power coefficient C_p possible at the given pitch angle β. The basic equation of the power yield of a wind turbine involves a proportional relation between the power coefficient C_p and the generated active power (2.4),

$$P_w = 0.5\rho C_p A v^3 \tag{2.4}$$

where P_w is the power yield of the turbine, A is the area swept by the turbine blades, ρ is the air density, v is the wind speed and C_p is the power coefficient. Accordingly, for a given wind speed, the amount of output active power of a WG is determined based on the value of C_p. The value of C_p is in turn a function of two variables, the tip speed ratio λ and the blade pitch angle β. The tip speed ratio is governed by (2.5),

$$\lambda = \frac{\omega r}{v} \tag{2.5}$$

where ω is the rotational speed of the turbine and r is the blade radius. The pitching of the blades is employed to regulate the mechanical input power to the WG at speeds above rated speed and below the cut-out speed. The pitching angle β is generally set to zero or very low values in the region of MPPT (typically between 5 m/s to 13 m/s). The determination of the optimal tip-speed ratio λ_{opt} is then based on the λ value maximizing the C_p coefficient. The C_p coefficient can be calculated utilizing several versions of empirical formulae, the one employed in this work is of the form of (2.6).

$$C_p = \frac{C_1(C_6\lambda + (-C_4 - C_3(2.5+\beta) + C_2(\frac{1}{\lambda + C_7(2.5+\beta)} - \frac{C_8}{1+(2.5+\beta)^3}))}{\exp(C_5(\frac{1}{\lambda + C_7(2.5+\beta)} - \frac{C_8}{1+(2.5+\beta)^3}))} \tag{2.6}$$

where C_1= 0.6450, C_2=116, C_3=0.4, C_4=5, C_5=21, C_6=0.00912, C_7= 0.08 and C_8=0.035.

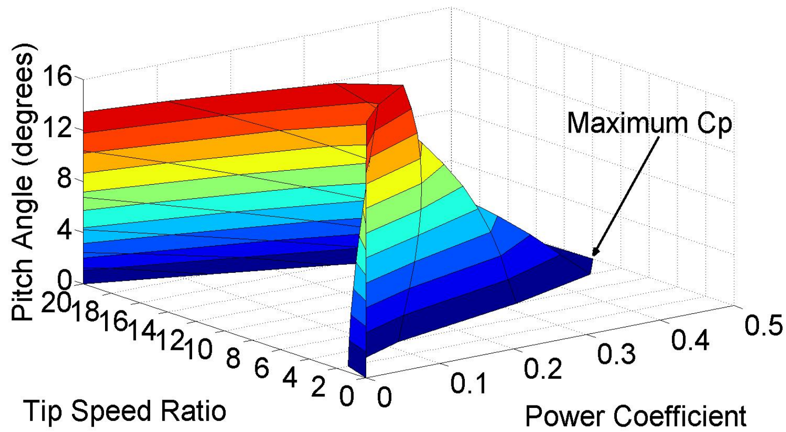

Figure 2.5: Power coefficient vs. pitch angle and tip speed ratio.

Figure 2.5 shows the relation between the three variables (tip-speed ratio, pitching angle and power coefficient) in a three-dimensional plot demonstrating how the three variables change in relation to one another. In accordance with Figure 2.5, the wind turbine is set to operate at a pitch angle of 0° in the MPPT region with the optimal value of the tip speed ratio being tracked by the machine speed control. As the generator reaches its maximum rotational speed, the machine enters the pitching region, in which the machine does not pursue the MPPT curve. Rather, the aim is to maintain the rotational speed and the active power generation at maximum operational values.

The $P - \omega$ characteristics can be best realized by exploring Figure 2.6 that shows the machine rotational speed and active power generation as a function of the wind speed for the 2 MW DFIG units in use in this thesis.

As the measured output power P_{mes} or rotational speed ω_{rot} of the machine exceeds the maximum values of P_{rated} and ω_{max} respectively, a positive error is generated, driving the pitch controller to maintain the outputs at the maximum values. A low-pass filter is used to account for the dynamics of the pitch actuator system. The pitch control system is shown in Figure 2.7.

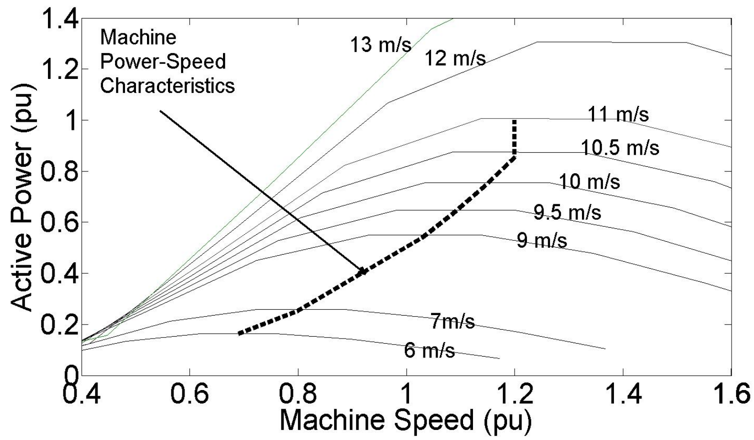

Figure 2.6: $P - \omega$ characteristics of the WG (2 MW DFIG unit).

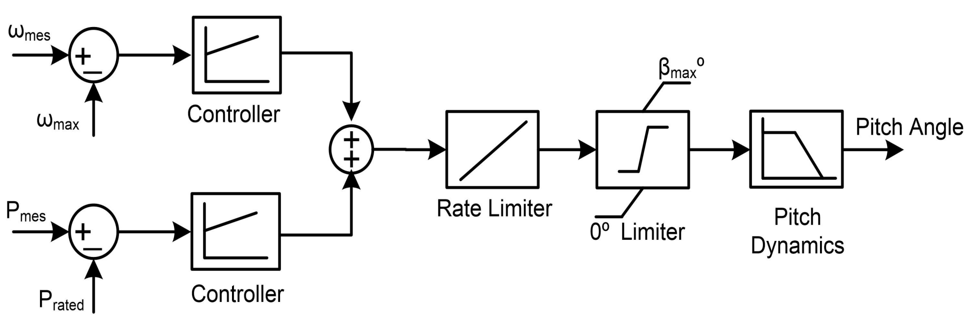

Figure 2.7: Pitch control system.

2.4.2 Mechanical Model

The combined inertias of the turbine and the generator determine the frequency range of wind speed changes seen in the output wind power. But generally, it is assumed that wind turbines can transfer frequency components up to 10 Hz in the wind speed profile to the output power spectrum [39]. Accordingly, a wind speed profile sampled at 0.1 s and a proper inertial model reflecting the WG rating would be suitable for flicker studies. Frequencies higher than 10 Hz are assumed to be suppressed by the low-pass filtering action of the drive train.

A two-mass model is used in this thesis to represent the WG drive-train in terms of two inertias, the low-speed mass (turbine) inertia constant H_{tu} and the high-speed mass (generator) inertia constant H_g. The two masses are linked by the shaft stiffness K_{sh}. The mutual damping D_m is included to represent the mechanical damping present in the drive-train (2.7), (2.8). More details on drive-train modeling can be found in [40].

$$2H_{tu}\frac{d\omega_t}{dt} = T_{tu} - K_{sh}(\theta_t - \theta_g) - D_m(\omega_t - \omega_g) \tag{2.7}$$

$$2H_g\frac{d\omega_r}{dt} = T_{ele} - K_{sh}(\theta_g - \theta_t) - D_m(\omega_g - \omega_t) \tag{2.8}$$

2.4.3 Wind Resource Data

A short-term wind speed profile representative of raw short-term wind speed measurement was used, more on the wind speed profile can be found in Appendix A. In order to reflect the aerodynamics at the turbine blades into the electric power output of the generator, the raw wind data had to be manipulated to account for the wind shear and the tower shadow impacts. The mathematical model of the 3p oscillations (tower shadow and wind shear effect) developed in [41] was employed for this purpose. The tower shadow occurs at a cyclic rate linked to the rotational speed of the turbine mass. Thus, the rotational speed of the turbine was fed to the mathematical model so that the frequency of the 3p torque oscillations would change as the machine speed changes. More on the mathematical model of the 3p torque oscillations can be found in Appendix B. The assumed base wind speed average in this work is 10 m/s. This is the highest wind speed provided in a turbine manufacturer IEC flicker test [36]. The wind data constitutes of 6000 data points representing a 10-minute time frame with wind data sampled at 0.1 s.

The wind time series has turbulence intensity of 0.15 (typical turbulence intensity values are > 0.1 and < 0.3). The raw wind measurement and the mathematically modified profiles are shown in Figure 2.8. Utilizing equations (2.4)-(2.8), the power yield of the turbine can be continuously updated under the imposed wind regime. The full implementation of the mechanical and aerodynamic models in the turbine-generator control sequence is shown in Figure 2.9.

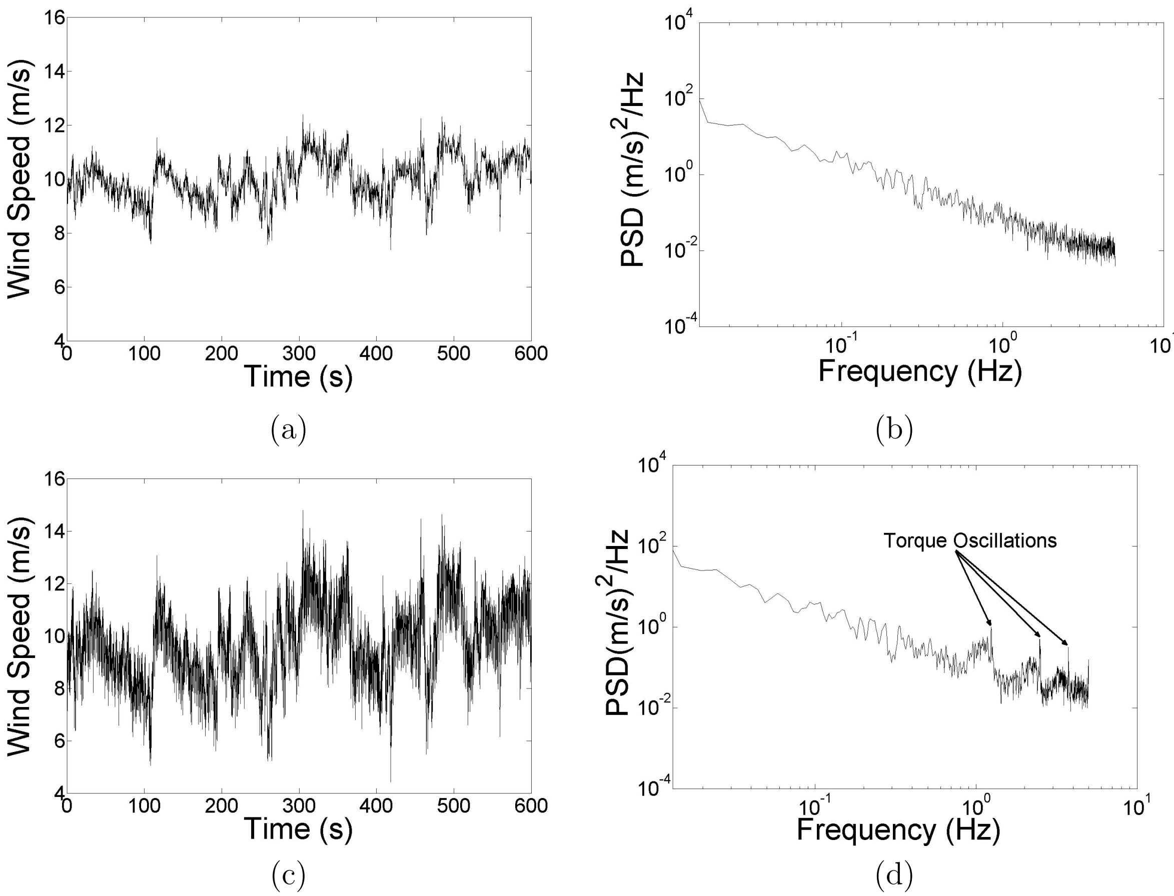

Figure 2.8: Wind speed data: (a) raw wind speed time-series, (b) raw wind speed power spectral density, (c) modified wind speed with 3p torque oscillations time-series, (d) modified wind speed power spectral density.

2.4.4 Electric Generator Control Modeling

The WGs targeted by this work are VS WGs that are mostly featured either as doubly-fed induction generators (DFIG) or full-converter synchronous generators. Due to the DFIG popularity, emanating from its reduced converter size and wide speed range operation [42, 43], the DFIG is the standard case in all the work presented in this thesis. Sample results are provided for the full-converter synchronous generator for the sake of completeness and generalization, this is provided in Appendix C. The details of the salient aspects of both generators modeling and control are provided in Appendix D.

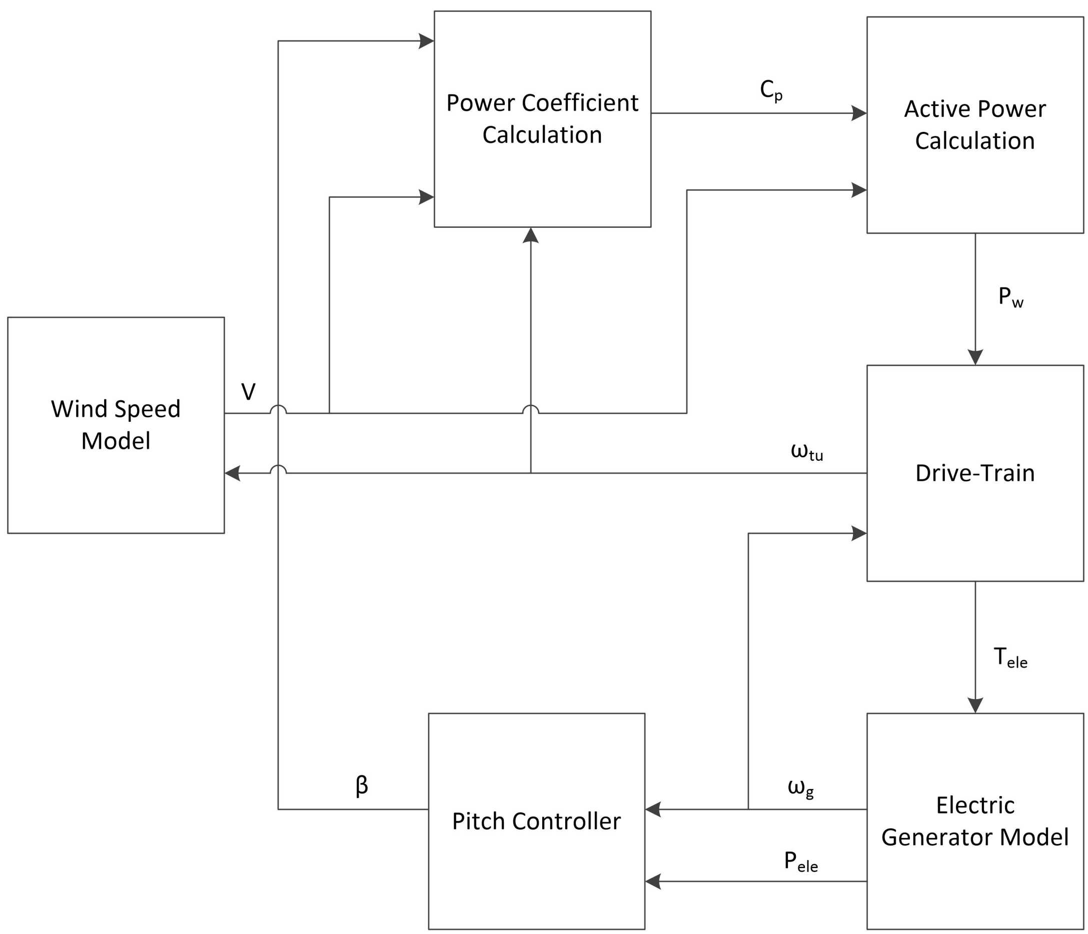

Figure 2.9: Wind-turbine-generator control sequence.

2.5 Wind Power Flicker Measurement

In this section, the flicker metrology employed in this thesis is explained to aid in the understanding of the results presented in the following chapters. Conventional flicker measurements were carried out by means of flicker curves that provided limits for the frequency (rate of repetition) of voltage changes as a function of the percentage voltage change in voltage amplitude, Figure 2.10. The use of flicker curves is not best suited to wind power installations or intermittent-resource power generation in general. Those flicker curves were based on flicker estimation from single-frequency disturbances (electric motor switching for instance), while the output spectrum of wind power consists of a range of varying frequencies. Moreover, conventional curves only provided a flicker limit in the form of the number of allowed voltage changes per a given time frame and did not provide a quantitative measure of the flicker severity applicable to flicker-sources like WGs.

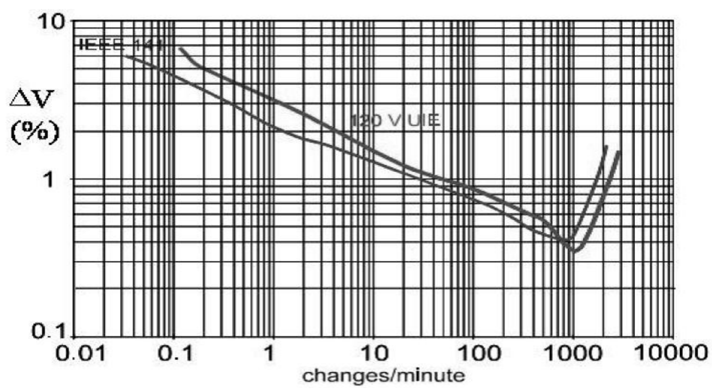

Figure 2.10: Conventional flicker curves, IEEE and IEC [13].

Flicker quantification from WGs is rather a complex process that requires high precision measurements. The guidelines of [44] outline the recommended design for a flickermeter as was introduced by the IEC and currently adopted by the IEEE and was therefore used as the flicker measuring apparatus in this thesis.

2.5.1 IEC Flickermeter Modeling

The operation of the IEC flickermeter is based on the emulation of the eye-brain response to light flicker induced by voltage fluctuations in incandescent lamps and interpretation in measurements representative of the irritation experienced by humans. The flickermeter processes the flicker-modulated voltage waveform over a time window and provides an index representative of the flicker severity for all frequencies of voltage amplitude fluctuations combined. The measurements can be performed for both short-term and long-term time frames. The short-term frame is of a 10-minute length and yields a short-term flicker severity index Pst. A long-term index Plt can be obtained from 12 consecutive short-term flicker measurements (2.9) [44]. More on the details of the flickermeter operation can be found in [44] and Appendix F.

$$P_{lt} = \sqrt[3]{\frac{1}{12}\sum_{k=1}^{12} P_{stk}^3} \tag{2.9}$$

The flickermeter was modeled as per [44]. It has to be outlined that the IEC flickermeter was the subject of scrutiny in some works and that modifications were proposed to improved its performance [45, 46, 47, 48, 49]. Yet, it is the currently accepted flicker metrology by utilities and grid codes. The compliance of the IEC flickermeter model used in this works was validated by conducting the tests detailed in Appendix G.

2.5.2 Verification of the Conglomerate Power System Setup

The verification process involved a number of parametric studies to ensure the proper behavior of the combined WG-distribution-network-flicker-measurement setup. The parametric studies were conducted for wind regimes of turbulence intensity ranging from 5 % to 30 % and average wind speed from 7 m/s to 10 m/s and connection point characteristics of X/R ratio ranging from 0.5 to 3.2 and SCCR ranging from 5 to 15. The summary of the results obtained from the parametric studies on the test system with the 2 MW DFIG unit are presented in Figure 2.11 and Figure 2.12. The conducted studies were realized by observing the measured flicker severity as the wind speed, turbulence intensity and the characteristics of the distribution network connection point changed. The obtained results reflected the proper behavior of the power system setup. The Pst values were found to be proportional to the wind speed average and the turbulence intensity and inversely proportional to the increase in the network X/R ratio and SCCR, reflecting the anticipated impact of varying such parameters, as ascertained in the previous studies of [23, 31, 34].

A summary of grid codes stances toward flicker from DG is presented in Appendix H to help provide guidance in understanding the nature of the flicker emission problem.

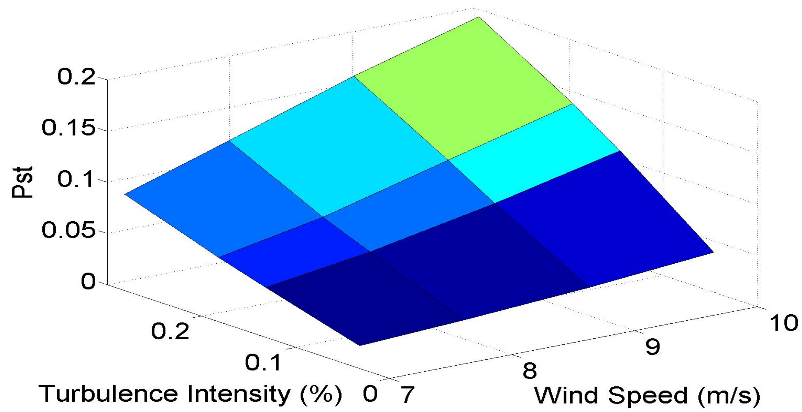

Figure 2.11: Pst as a function of wind speed and turbulence intensity at SCCR of 15 and X/R ratio of 0.52, 2 MW DFIG.

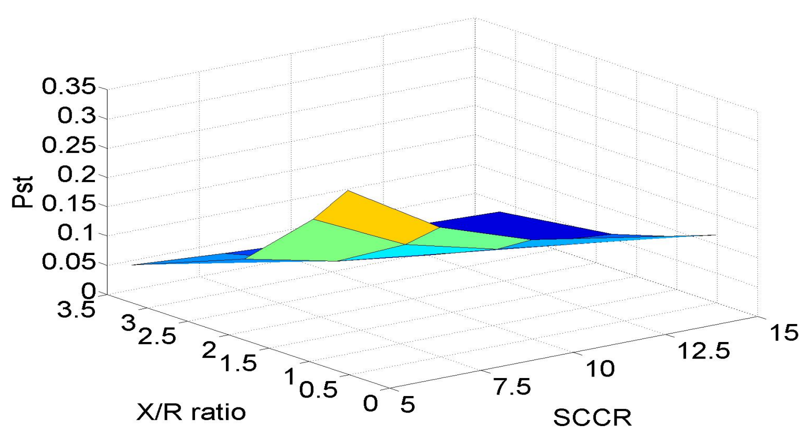

Figure 2.12: Pst as a function of SCCR and X/R ratio at wind speed average of 10 m/s and turbulence intensity of 15 %, 2 MW DFIG.

2.6 Conclusion

Distribution-connected WGs result in voltage flicker problems that restrict the amount of wind power admissible to a given distribution network. The flicker emission severity is affected by the turbine topology and the network/farm characteristics. In order to study the flicker emission of WGs, those factors need to be taken into consideration to identify the dependability of the flicker severity on the connection point characteristics and the consequent effectiveness of a potential flicker mitigation control scheme. The preconnection studies of a distributed WG therefore include the modeling of the wind-turbine-generator, the site wind conditions, the flicker metrology and the connection point characteristics. The entire modeling process required for those studies was described as implemented. This included the development of simplified and detailed distribution network models, a WG flicker-oriented model and a model of the IEC flickermeter. Extensive parametric studies were conducted on the conglomerate power system setup and the flicker severity was seen to follow the anticipated trends as reported in earlier works. The power system setup and the detailed distribution network described in this chapter are the ones used in the following chapters to verify the functionality of the proposed flicker mitigation control schemes.

Chapter 3

Impact of WGs Reactive Power Behavior on Flicker Emission

3.1 Introduction

WGs reactive power control is achieved via the control of the power electronic grid-interface converter and following a designated reactive power control scheme. More specifically, the machine can be operated in either of the three following possible reactive power control schemes: 1) fixed power factor control mode, 2) terminal voltage control mode or 3) fixed reactive power control mode. The most conventional of which is the fixed power factor control mode, in which the reactive power controls of the machine only respond to changes in the machine active power production, and hence to voltage changes exclusively prompted by the machine active power production variation. Conversely, voltage control aims at the control of the voltage magnitude at a bus of concern, typically the PCC. Therefore, the voltage control mode changes the WG reactive power reference in response to voltage changes induced by variations in the WG active power production as well as those induced by variations in the network loading conditions. The least common option is to have the machine inject or absorb a fixed amount of reactive power irrespective of its level of active power generation. The simplified two-bus single-line diagram shown in Figure 3.1 can be utilized to express the voltage changes at the PCC in terms of both active and reactive power flows at the PCC providing an explanation for how reactive power control impacts the PCC voltage variations and therefore the WG flicker severity. The voltage at the PCC can be expressed in terms of the grid voltage $\vec{V}_g$

(MV substation voltage level) and the line current $\vec{I}$ as in (3.1);

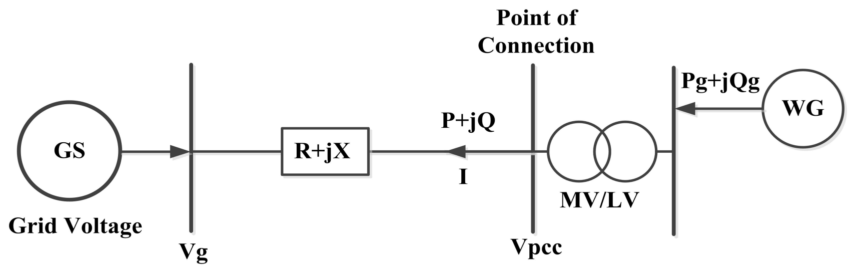

Figure 3.1: Simplified single-line diagram.

$$\vec{V_{pcc}} = \vec{V_g} + \vec{I}(R + jX) \tag{3.1}$$

where $\vec{V_{pcc}}$ is the PCC voltage, R and X are the line resistance and reactance respectively. Substituting the line current $\vec{I}$ in terms of the apparent power at the PCC (active power flow P and reactive power flow Q) and considering $\vec{V_g}$ to be the reference voltage with angle 0° and $\vec{V_{pcc}}$ to have an angle δ, (3.2) is derived.

$$V_{pcc}\cos\delta + jV_{pcc}\sin\delta - V_g = \frac{P - jQ}{V_{pcc}\cos\delta - jV_{pcc}\sin\delta}(R + jX) \tag{3.2a}$$

$$(V_{pcc}\cos\delta)^2 + (V_{pcc}\sin\delta)^2 - V_g(V_{pcc}\cos\delta - jV_{pcc}\sin\delta) = (PR + QX) + j(PX - QR) \tag{3.2b}$$

$$(V_{pcc})^2(\cos^2\delta + \sin^2\delta) - V_gV_{pcc}\cos\delta + jV_gV_{pcc}\sin\delta = (PR + QX) + j(PX - QR) \tag{3.2c}$$

$$(V_{pcc})^2 - V_gV_{pcc}\cos\delta + jV_gV_{pcc}\sin\delta = (PR + QX) + j(PX - QR) \tag{3.2d}$$

$$V_{pcc}(V_{pcc} - V_g cos\delta) + jV_gV_{pcc}\sin\delta = (PR + QX) + j(PX - QR) \tag{3.2e}$$

Separating and equating the real and imaginary terms of (3.2e), (3.3) and (3.4) are obtained.

$$V_{pcc}(V_{pcc} - V_g cos\delta) = (PR + QX) \tag{3.3}$$

$$V_g V_{pcc} \sin\delta = (PX - QR) \tag{3.4}$$

As the value of the angle δ diminishes to approach negligible values as assumed in distribution networks, the change in voltage magnitude between the PCC and the grid voltage can be expressed as (3.5).

$$\Delta V \approx \frac{PR + QX}{V_{pcc}} \tag{3.5}$$

Equation (3.5) is the basis of power-factor-control-based voltage level compensation as well as flicker emission mitigation in DG. Equation (3.5) is thus used to describe the voltage changes in a fixed power factor control mode and is based on the fact that any connection point of a detailed network can be studied by reducing the network to its equivalent impedance, at the point of connection, to study the impact of DG on voltage changes. Furthermore, to better tailor the equation to the definition of voltage flicker and help aid in the explanation of voltage changes, (3.5) is rewritten as a relative voltage change and the active and reactive power flows causing the change after connection are expressed as active power changes ΔP and reactive power changes ΔQ respectively (3.6). Equation (3.6) is thereafter used to describe the voltage changes over the feeder.

$$\frac{\Delta V}{V_{pcc}} \approx \frac{\Delta PR + \Delta QX}{V_{pcc}^2} \tag{3.6}$$

3.2 Fixed Power Factor Control

The implementation of fixed power factor control is shown in Figure 3.2. The WG has a filter to suppress the switching voltage harmonics. The reactive power contribution of that filter capacitor Q_{fil} is negligible but is added to the term $P_{ref} \tan\phi$ (where ϕ is the fixed WG phase angle) for the sake of preciseness such that the power factor control setting refers to that at the WG connection terminals. The machine is assumed to be capable of operating at 0.9 power factor for the full range of operation either lagging or leading such that Q_{max} is 0.485 pu (3.7).

$$Q_{ref} = \pm min\{|P_{ref} \tan\phi + Q_{fil}|, 0.485\} \tag{3.7}$$

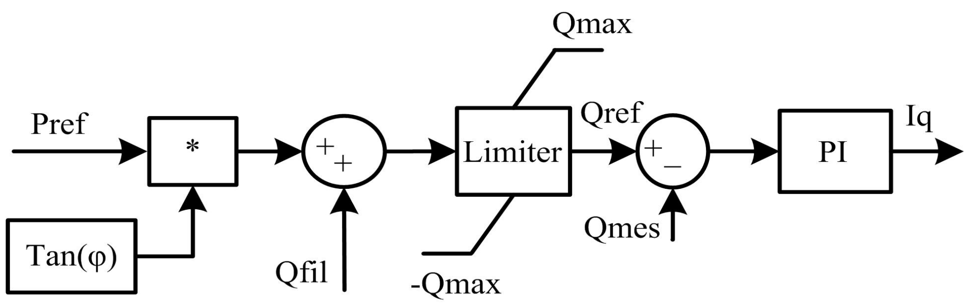

Figure 3.2: Fixed power factor control.

The operation of the WG under a fixed power factor can assume any of the following modes:

1. Unity Power Factor: This is the preference of all utilities that recommend unity power factor for WGs and can be regarded as a reference case to which the different reactive power management schemes can be compared with respect to flicker emission severity. The WG reactive consumption is zero at all times and (3.6) reduces to (3.8).

$$\frac{\Delta V}{V_{pcc}} \approx \frac{\Delta PR}{V_{pcc}^2} \tag{3.8}$$

A change in active power ΔP results in a voltage change ΔV only governed by the line resistance R and increases in magnitude as the line resistance increases. The corresponding Pst values obtained at the PCC for the contemplated test cases of Table 2.1 on the simplified network equivalent of Figure 2.3 are shown in Figure 3.3.

The feeder with the highest resistance (X/R=0.52) at any given SCCR undergoes the highest Pst values. The percentage increase in Pst is higher for the weaker feeders as the SCCR decreases. For instance, a 173 % increase is observed in Pst for X/R=0.52, increasing from 0.115 at an SCCR of 15 to 0.3142 at an SCCR of 5 while the increase is around a 100 % for the strongest feeder (X/R=3.2), for the

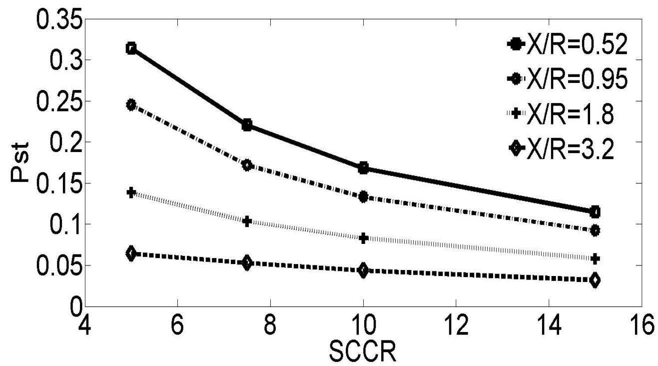

Figure 3.3: Pst vs. SCCR, unity power factor.

same range of SCCRs, increasing from 0.0321 to 0.0644. What can be inferred about this mode of operation is that the increase in flicker severity will be much less sensitive to SCCR changes as the network X/R ratio increases

2. Lagging Power Factor: This is the case if the wind farm is required to assist the OLTC in compensating the voltage drop in lengthy, heavily-loaded feeders or in cases where reactive power injection by DG is utilized as means of minimizing the reactive burden on the transmission level sources [50]. The change in voltage in this case is affected by both the feeder resistance and reactance (3.9). The corresponding Pst values are shown in Figure 3.4 for the typical utility-imposed lower limits of 0.95 and 0.9 lagging power factors [51].

$$\frac{\Delta V}{V_{pcc}} \approx \frac{\Delta PR + \Delta PX|\tan\phi|}{V_{pcc}^2} \tag{3.9}$$

As can be seen, lagging power factor operation in utility specified ranges highly aggravated the flicker severity as the feeder X/R ratio increased. This is due to the fact that a change in WG active power injection, either an increase or a decrease, prompts a corresponding change in reactive power (increase or decrease) to maintain the fixed power factor setting, and in both cases the reactive and active power flows are from the WG to the network and the change in voltage magnitude is amplified by the prompted reactive power response. As the value of X increases, the feeder becomes more sensitive to any change in reactive power and the amplified flicker severity is more conspicuously seen for the higher-X/R-ratio feeders. The

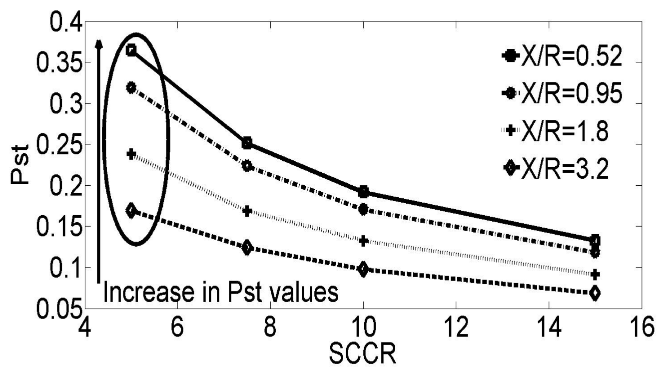

(a)

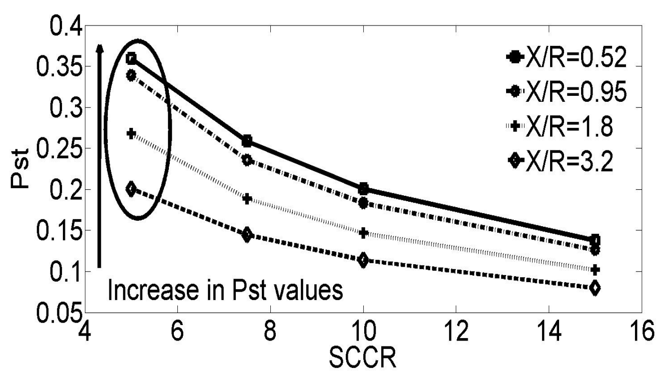

(b)

Figure 3.4: Pst vs. SCCR, lagging power factor: a) 0.95 lagging, b) 0.9 lagging.

highest Pst value for the strongest feeder (X/R=3.2) at an SCCR of 5 was 0.0664 under unity power factor operation. This value amplified to 0.2008, increasing by 202.409 %, as the WG supplied reactive power to the network at 0.9 lagging power factor. Generally, all feeders underwent higher Pst values with lagging operation, except that the percentage increase in Pst decreased as the X/R ratio decreased. The weakest feeder (X/R=0.52) had the lowest percentage increase, increasing from 0.314 to 0.3595 at 0.9 lagging operation at an SCCR of 5. A general remark regarding this mode of operation is that with the increase in the X/R ratio, there is less probability of voltage rise problems due to DG and consumption of reactive power is not generally a demand on the WG, rather injection can be a requirement. Flicker severity should be closely examined in such cases to identify the increase in its severity with lagging power factor operation of the WG.

3. Leading Power Factor: The purpose of this mode is generally to reduce the PCC voltage rise emanating from the installation of DG. Implementation is the same in principle as lagging power factor except that the machine is required to absorb reactive power rather than injecting it, (3.10).

$$\frac{\Delta V}{V_{pcc}} \approx \frac{\Delta PR - \Delta PX|\tan\phi|}{V_{pcc}^2} \tag{3.10}$$

This mode of operation is reported to be effective in flicker mitigation by theoretically adjusting ϕ in relation to the network X/R ratio [23, 24]. The reactive power consumption of the WG has to be adjusted to a value of $R\Delta P/X$ (where ΔP refers to the total WG active power production causing the voltage change at the PCC) so that the voltage changes are minimized by attempting to maintain the fixed PCC preconnection voltage magnitude, (3.11).

$$\frac{\Delta V}{V_{pcc}} \approx 0 \tag{3.11}$$

Operational constraints that hamper this approach in achieving flicker mitigation include:

(a) Power factor grid code limits: this is illustrated by inspecting Figure 3.5 that shows the value of the power factor required to nullify the voltage change at the PCC as a function of the X/R ratio of the connection network impedance.

It is evident that as the grid X/R ratio decreases, the power factor setting of the machine has to decrease to nonoperational values. Under a limit of 0.95 leading power factor, the mitigation curve based on (3.11) will be satisfied down to an X/R ratio of 3.04 while if a limit of 0.9 leading is allowed, the curve will be satisfied down to an X/R ratio of 2.0647.

(b) Connecting feeder losses: assuming $Vpcc \approx 1$ pu, the increase in machine current associated with leading power factor as defined by (3.11) can be described by (3.12), and the associated increase in line losses by (3.13).

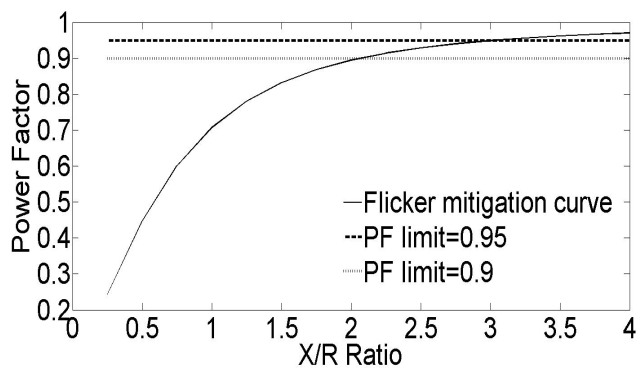

Figure 3.5: Flicker mitigation requirement (power factor vs. X/R ratio).

$$\Delta|I| = P(\sqrt{1+\tan^2\phi} - 1) \tag{3.12}$$

$$\Delta Loss = P^2(1+\tan^2\phi) - P^2 = P^2\tan^2\phi \tag{3.13}$$

This would increase the feeder losses by 400 % for an X/R ratio of 0.5 for instance.

(c) Machine limits: The machine is required to absorb significant amounts of reactive power, for instance 1 pu of reactive power at rated machine output for an X/R ratio of 1 and 2 pu for an X/R ratio of 0.5, rendering this implementation operationally infeasible as the X/R ratio decreases.

3.3 Voltage Control

The conventional voltage control scheme is by droop characteristics, the methodology is based on predefining a characteristic curve that assigns the reactive power setpoint of the WG in response to voltage measurement at the control point (PCC in this work), (3.14), Figure 3.6.

$$V = V_r - k(Q - Q_r) \tag{3.14}$$

Where V_r is the reference voltage, Q_r is the reference reactive power at V_r and k is the droop coefficient. The droop coefficient is in kV/MVAR and is set to result in gradual reactive power changes to limit the magnitude of voltage changes to its limits. The range of voltage changes assumed in this work is ± 6 % of V_r [51]. The droop gain for the specified voltage band and a maximum reactive power consumption of 0.48 pu is 8.0717. The implementation of the voltage controller is shown in Figure 3.7.

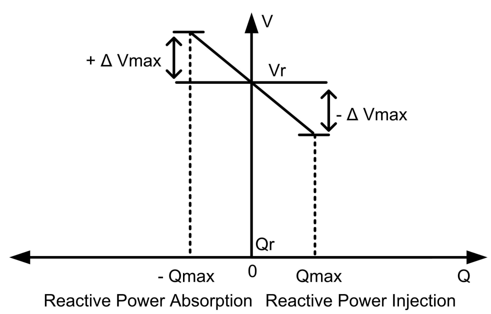

Figure 3.6: Voltage control droop curve.

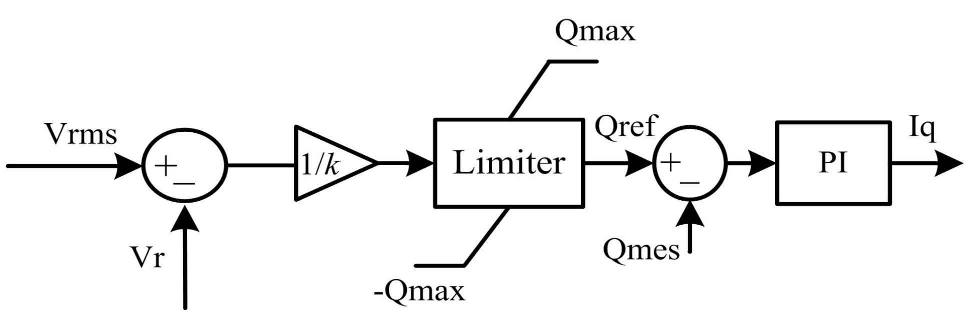

Figure 3.7: Voltage control by droop characteristics.

The Pst values are shown in Figure 3.8 for all test cases under the WG voltage control mode, where V_r is set to 1 pu and corresponding Q_r to zero. The results show that the effectiveness of voltage control in decreasing the flicker severity at the PCC increases as the X/R ratio of the network increases. The flicker values are almost controlled to a constant value over the entire range of SCCRs for both the feeders of X/R ratios of 1.8 and 3.2.

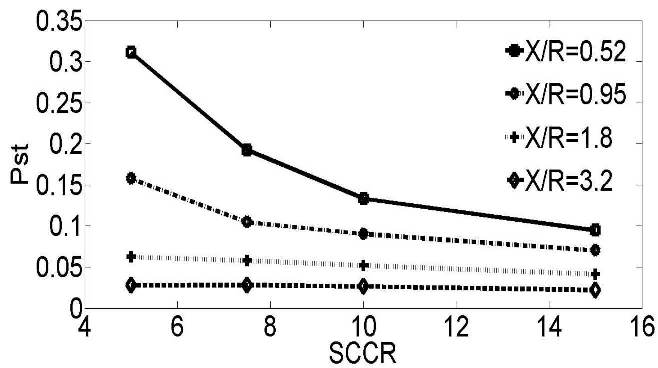

Figure 3.8: Pst vs. SCCR, voltage control.

The impaired flicker mitigation for the lower-X/R-ratio feeders as the SCCR decreases can be attributed to the nature of the voltage control action that responds to the steady-state voltage level at the PCC which to be compensated for the lower-X/R-ratio feeders, considerable reactive power is required to be absorbed. But Q_{ref} to the machine is limited by its maximum value and hence is consumed at its limit, thus any increase in voltage cannot be counteracted by a corresponding change in reactive power as $Q_{ref} = Q_{mes} = Q_{max}$ and the error fed to the reactive current controller is zero in that case, Figure 3.9. It is worth mentioning that if the machine is not limited by a cap of reactive power consumption and allowed to absorb whatever the capability curve permits, the reduction in Pst values as the SCCR decreases for the feeders of X/R=0.52 and X/R=0.95 will be more remarkable than that shown in Figure 3.8.

3.4 Fixed Reactive Power Control

In this control mode, Q_{ref} is specified explicitly irrespective of the WG active power production and the requirement is to have the WG continuously inject or absorb a fixed

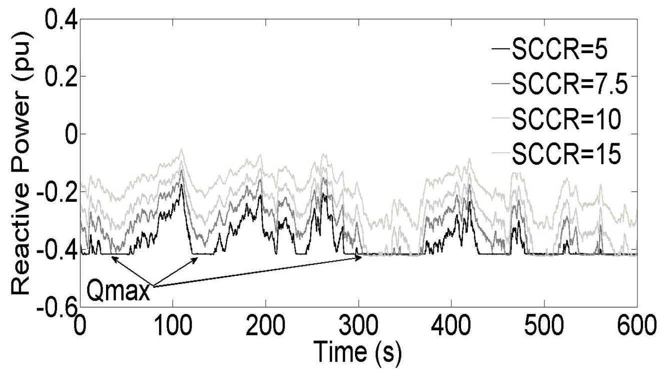

Figure 3.9: Reactive power consumption at varying SCCR for X/R=0.052 (voltage control).

amount of reactive power. Two reactive power reference settings were assumed in the studies in which the WG Q_{ref} was set to 0.25 pu and – 0.25 pu. No major differences in flicker severity were detected in reference to the case of unity power factor, Figure 3.10. A sound explanation for this is that flicker severity is only affected by the reactive power flow if the reactive power changes occur in response to WG active power changes, and in the case of fixed reactive power control, the reactive power of the WG is a constant value that does not respond to the WG active power production. The change in voltage magnitude can only be seen in the steady-state level and the effective flicker severity behavior is equivalent to that described by (3.8) where a flicker-producing active power change is left uncompensated by reactive power and the severity of the voltage change is only governed by the line resistance.

By contemplating the theoretical basis and operational aspects of the above mentioned conventional WG reactive power control schemes, it can be inferred that flicker mitigation can be achieved by either operating the WG under terminal voltage control or under leading power factor control. Nevertheless, the operation under those schemes has limitations that must be accounted for either in terms of WG reactive power capability limits or in terms of enforced grid codes. With respect to the latter, it should also be noted that the trend of flicker emission severity behaves differently than that of the steady-state voltage level as the leading power factor setting decreases. In other words, as the leading power factor setting decreases, the steady-state voltage level will continuously decrease, conversely an optimal power factor setting exists at which flicker severity reaches a minimum and beyond which flicker severity increases. This is a result of the

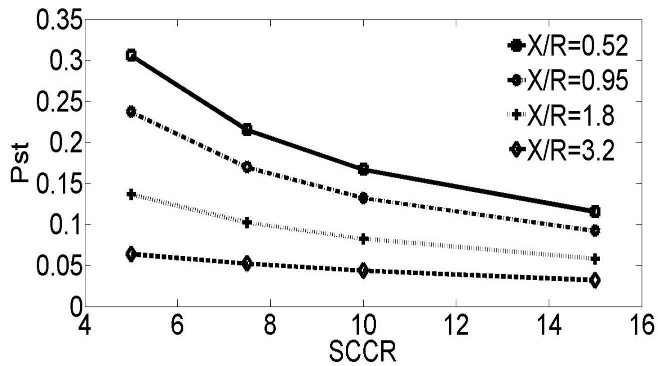

(a)

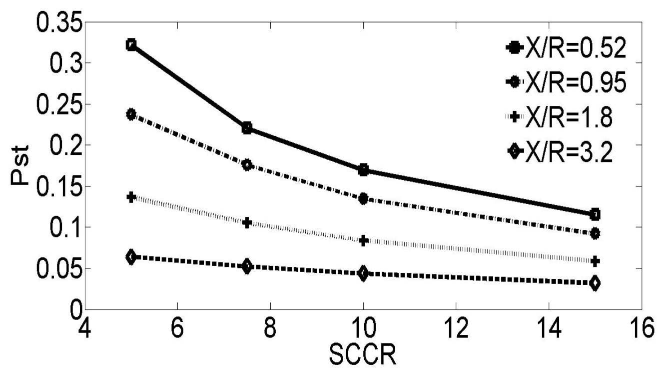

(b)

Figure 3.10: Pst vs. SCCR, fixed reactive power control: a) 0.25 pu injection, b) 0.25 pu absorption.

voltage changes causing flicker being overcompensated by reactive power and yielding a negative voltage change rather than a nullified voltage change, as aimed for in (3.11), and hence exacerbating the flicker severity as overcompensation increases (decrease in power factor setting). This can be clearly seen in Figure 3.11 and Figure 3.12 in which both the Pst values and RMS voltage levels are plotted respectively for a range of fixed leading power factor settings of 1-0.86 for feeder X/R ratios of 3.2 and 1.8 at an SCCR of 10.

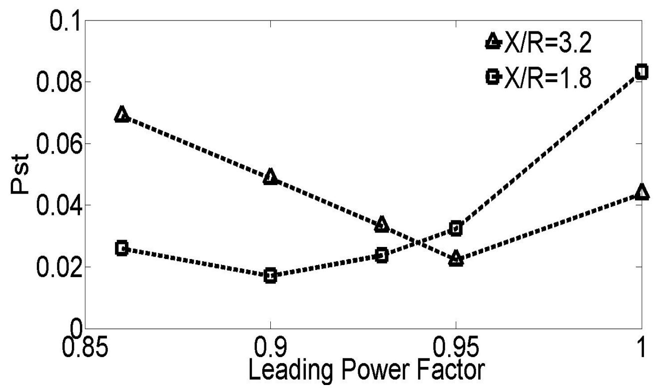

Figure 3.11: Pst as a function of leading power factor at an SCCR of 10.

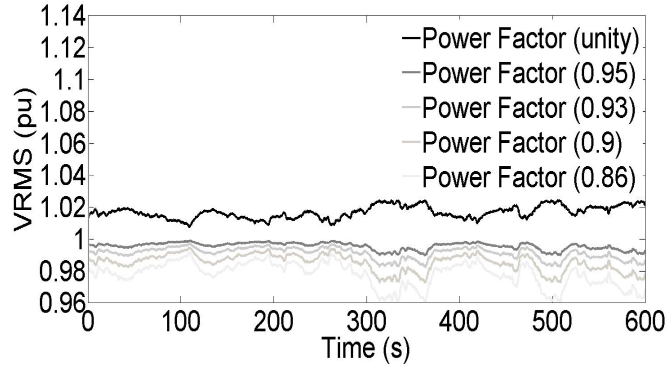

(a)

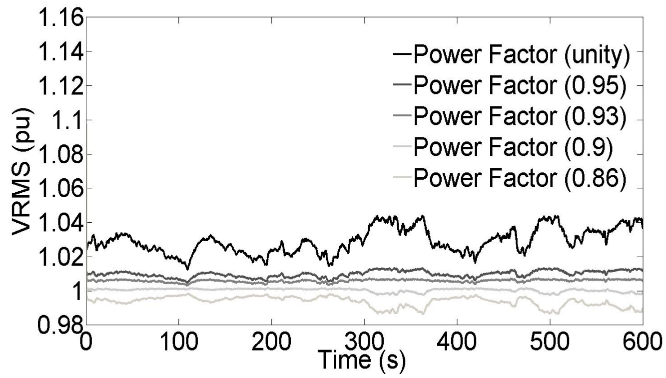

(b)

Figure 3.12: VRMS as a function of leading power factor at an SCCR of 10: a) $X/R = 3.2$, b) $X/R = 1.8$.

3.5 Mitigation Impairment

The following can be summarized as the impairing factors in achieving the sought WG flicker mitigation by means of reactive power control:

1. Inability to achieve mitigation while injecting reactive power (lagging power factor operation).

2. Infeasibility of leading power factor operation and voltage control as the X/R ratio decreases, in terms of consumed reactive power, increased line currents and losses.

3. Presence of grid codes restrictions on both leading power factor and voltage control modes.

4. Conflicting operation of steady-state voltage level compensation and flicker mitigation.

To address the above limitations, a flicker-range-based variable power factor reactive power control scheme is proposed.

3.6 Decoupled Reactive Power/Variable Power Factor Operation

A decoupled frequency-selective reactive power control scheme is proposed in which the WG reactive power behavior is in a variable power factor operation mode varying around a fixed steady-state power factor setting. The fixed setting yielding the desired relation between the steady-state machine active and reactive power, thus being capable of operating in either a leading or a lagging fashion, conforming to the desired features of conventional fixed power factor control. The induced deviations from that fixed setting are dedicated to the flicker range, being only invoked by the estimated undesired flicker content induced in the voltage waveform. The essence of the proposed control is to manipulate the flicker-producing active power fluctuations irrespective of the nonflicker-producing active power changes, or in other words splitting (3.6) into two frequency spectrums, a flicker-producing spectrum and a nonflicker-producing spectrum. In this manner, the WG can mitigate the impact of the flicker-producing changes in its output irrespective of the general desired reactive power steady-state behavior of the WG and its level of active power generation. In that case, the WG reactive power reference takes the form of (3.15),

$$Q_{ref}(s) = K(\frac{P_{ref}(s)\tau s}{1+\tau s}) + N(\frac{P_{ref}(s)}{1+\tau s}) + Q_{fil}(s) \tag{3.15}$$

where τ is a time constant denoting the start of the flicker frequency range, K is the ratio of changes in Q_{ref} in response to the flicker-producing changes in P_{ref} and N is the ratio of changes in Q_{ref} in response to the nonflicker-producing changes in P_{ref}. With respect to voltage flicker based on current IEC and IEEE standards, only frequencies above 0.05 Hz contribute to flicker severity, Figure 3.13. Thus an appropriate value for τ is 3.18 s. The desired control can be realized by setting the value of N in (3.15) in accordance with the utility requirement on the WG reactive power, such that the desired reactive

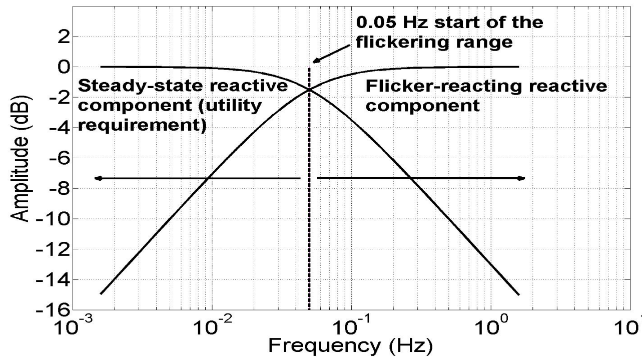

Figure 3.13: Bode plot, decoupled variable power factor reactive power control.

power injection or absorption behavior of the WG is achieved, and setting the value of K in reference to the network X/R ratio, such that the flicker content is suppressed. It has to be noted that if the flicker-producing content in P_{ref} is to theoretically vanish, the WG operates at the specified fixed power factor setting of N ($\tan\phi$) in a fixed power factor control mode, Figure 3.14. The two filtered components of P_{ref} (shown in Figure D.5 (c)) are shown in Figure 3.15, where P_{ref} is the output active power of the WG as estimated in the MPPT block. The impact of this control scheme on flicker mitigation is demonstrated on the test power systems in the following sections.

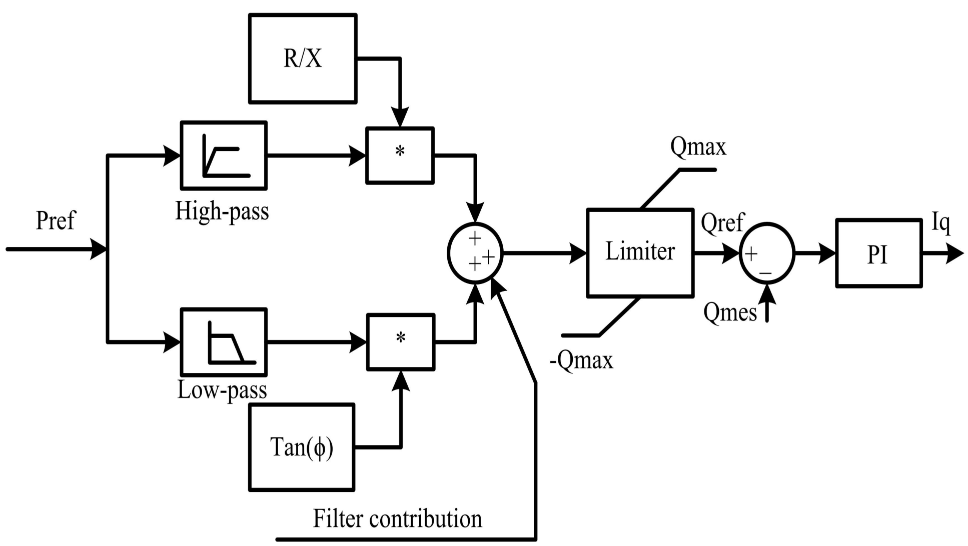

Figure 3.14: Decoupled variable power factor reactive power control scheme.

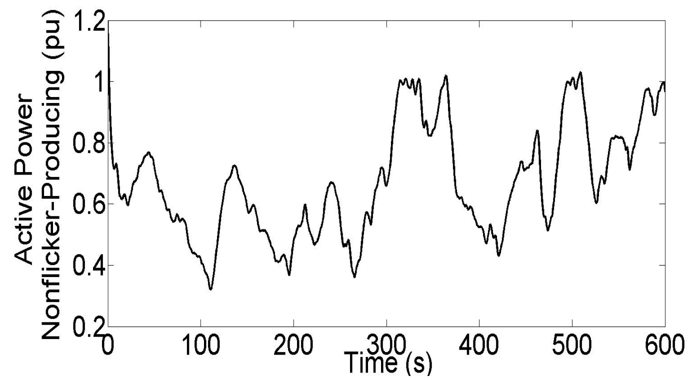

(a)

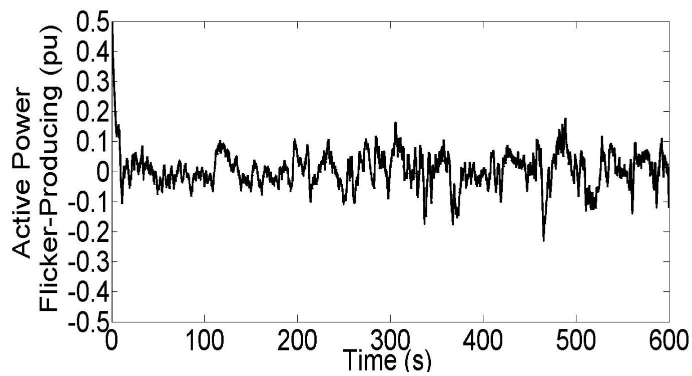

(b)

Figure 3.15: Filtered active power reference components: (a) nonflicker-producing component, (b) flicker-producing component.

3.6.1 Simplified Network Equivalent

Of prime importance is the demonstration of the feasibility of the proposed scheme in mitigating flicker under zero steady-state reactive power exchange with the grid and injection (supply to the grid) of reactive power, as opposed to conventional mitigation by WG reactive power absorption. Thus, two scenarios are profoundly tested on the simplified network equivalent, 1) the steady-state reactive power consumption is zero ($\phi = 0°$), Figure 3.16, and 2) the injection is centered around 0.95 lagging power factor ($\phi = 18.2°$), Figure 3.17. Those scenarios are tested on the simplified network equivalent and all reactive power behavior scenarios are tested on the detailed distribution network on a wind farm level (connection at Bus 16 of the network of Figure 2.4).

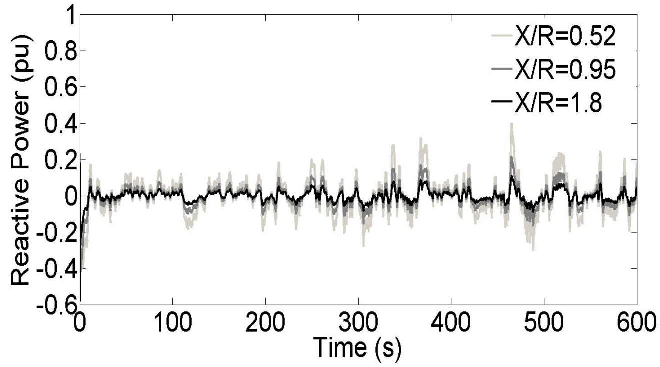

(a)

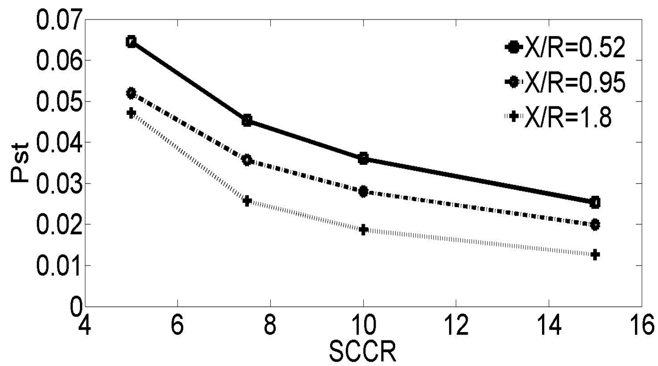

(b)

Figure 3.16: Decoupled reactive power control, unity operation: (a) reactive power consumption, (b) Pst vs. SCCR.

In Figure 3.16 (a), the reactive power consumption of the WG for three different X/R ratios is shown. In all the three cases, the WG is shown to operate around a unity power factor with deviations from that setting corresponding to the fluctuations of Figure 3.15 (b). The level of deviations from that setting for the same active power injection is seen inversely proportional to the X/R ratio of the impedance (bigger deviations for lower X/R ratios). The Pst values are shown to be significantly mitigated for all cases as compared to the conventional unity power factor operation in Figure 3.3. Similarly, the sought flicker mitigation and performance are observed for the case of WG reactive power injection in Figure 3.17, except that the steady-state reactive power behavior of the WG in that case is of lagging power factor operation.

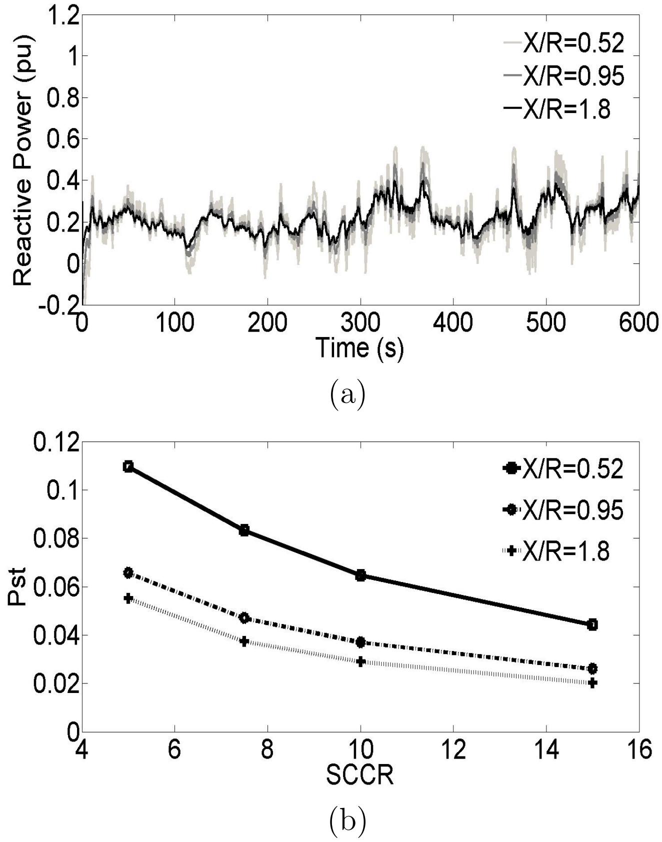

Figure 3.17: Decoupled reactive power control, 0.95 lagging operation: (a) reactive power injected, (b) Pst vs. SCCR.

3.6.2 Detailed Distribution Network Case Study

In order to effectively test the proposed control scheme on the detailed distribution network, a number of hypothetical scenarios were assumed such that the rating of the wind farm takes a range of values resulting in different voltage levels at the PCC. Accordingly, different requirements on the reactive power behavior of the WGs were assumed, such that the PCC voltage is kept around a typically desired 1 pu level. More specifically, the following cases were considered: Case 1), a 4 MW, 8 m/s farm (2 units) is assumed for a case of low voltage at the point of connection and requirement on the WGs to raise the voltage at a lagging power factor of 0.9; Case 2), a 6 MW, 10 m/s farm (3 units) and an 8 MW, 10 m/s farm (4 units) are assumed for no reactive power requirement on the WGs; and Case 3), a 10 MW, 10 m/s farm (5 units) is assumed for leading power factor operation of 0.99. The Pst values for all scenarios under fixed power factor control, voltage control and decoupled reactive power control are shown in Table 3.1.

Table 3.1: Pst Values Under Test Scenarios

Generation Scenario	Pst (Fixed Power Factor)	Pst (Voltage Control)	Pst (Decoupled Control)
2 units (4 MW)	0.1199	0.0601	0.027
3 units (6 MW)	0.1475	0.0654	0.038
4 units (8 MW)	0.1739	0.0656	0.049
5 units (10 MW)	0.1155	0.0622	0.066

The results obtained from the tests conducted on the detailed network were coherent with those on the simplified network equivalent model for all modes. The decoupled operation either under injection of reactive power, no reactive requirement or absorption of reactive power is shown to present its flicker-mitigating capability. The corresponding voltage waveforms to the three reactive power scenarios corresponding to Table 3.1 are shown in the figures below. Figure 3.18 shows the voltage profile at the PCC for the 4 MW wind power generation scenario (case 1) under three reactive power control approaches: conventional unity, conventional reactive power injection (0.9 lagging) and decoupled reactive power injection (0.9 lagging). This case shows that the flicker content can be mitigated despite the lagging operation and injection of reactive power by the wind farm generators. As can be seen, the voltage waveform under the decoupled reactive power injection is the smoothest and the lowest in flicker content. The voltage profile at the PCC for the 6 MW wind power generation scenario (case 2) under zero steady-state reactive power exchange between the farm and the grid is shown in Figure 3.19. It is seen that the voltage waveform under the decoupled control is not very different, steady-state-level-wise, from that under the conventional unity operation. It is, however, characterized by a smoother profile due to the fact that the decoupled control mitigated the voltage impacts of the flicker-producing active power variations. The same holds true for the line currents that are maintained at their same steady-state values except for the hikes at the instants a flicker-producing change was counteracted.

Finally, Figure 3.20 illustrates the operation under decoupled absorption of reactive power. In the absence of the decoupled control scheme, the reactive power absorbed is bound by the lower voltage limit and hence a 0.99 leading power factor is sufficient to keep the voltage magnitude within permissible limits and partial flicker mitigation is achieved

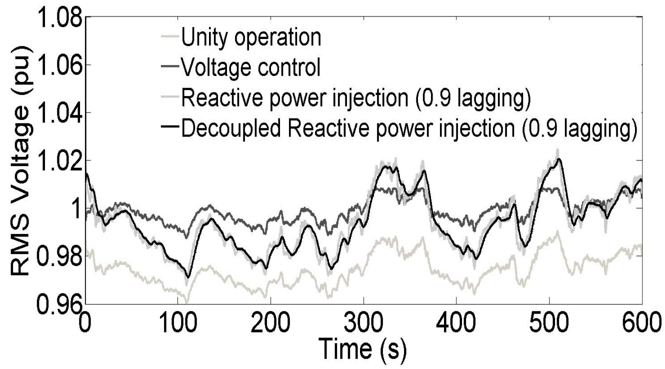

Figure 3.18: RMS voltage at the PCC, reactive power injection and farm rating of 4 MW.

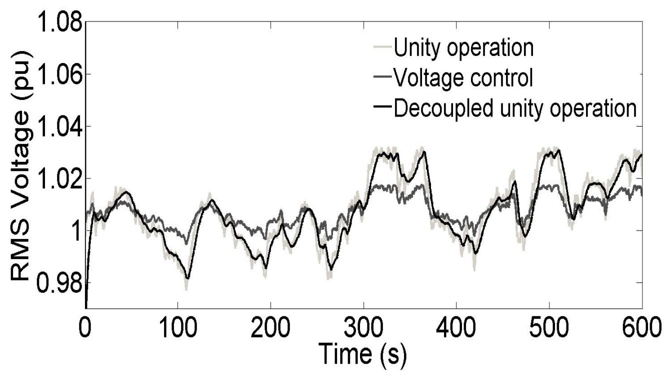

Figure 3.19: RMS voltage at the PCC, zero steady-state reactive power exchange and farm rating of 6 MW.

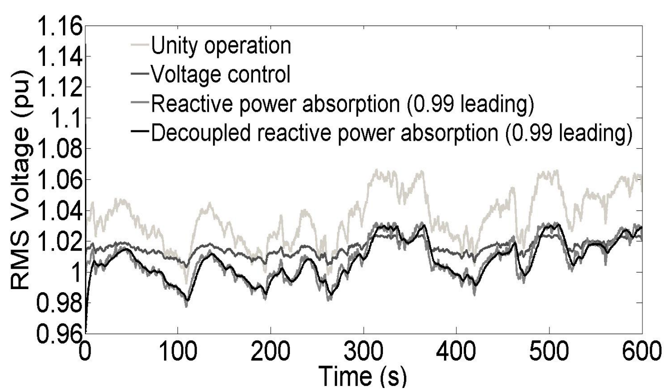

Figure 3.20: RMS voltage at the PCC, reactive power absorption and farm rating of 10 MW.

as expected. However, the operation under decoupled reactive power control makes it possible to achieve even larger mitigation while neither compromising the voltage level nor drawing unnecessarily excessive reactive power from the network.

The interaction with network loads was also studied by introducing a voltage-sensitive load of 500 kW/-250 kVAR at buses 15 and 16 alternately for Case 3 (3 units scenario). The results are tabulated in Table 3.2.

Table 3.2: Pst Values Under Wind Power Load Interaction

Connection Bus	Pst (Fixed Power Factor)	Pst (Voltage Control)	Pst (Decoupled Control)
Bus 15	0.1533	0.0679	0.0401
Bus 16	0.1551	0.0688	0.0409

It is seen from Table 3.2 that the presence of the voltage-sensitive load has a contribution to the new flicker levels, measured at the point of connection, and that that contribution is a function of the proximity of the load to the wind farm integration bus (increases by increase of proximity). The proposed decoupled control scheme still maintained its flicker mitigation capability in that case.

3.7 Conclusion

The flicker emission severity of a distributed WG was closely investigated in reference to the behavior and levels of reactive power exchange between the grid and the WG. It was shown that the flicker severity will only be affected, either amplified or mitigated, if the reactive power changes occur in correspondence to active power flicker-producing changes. The results showed that the flicker emission aggravates when the WG is operated under lagging power factor signifying the need to achieve flicker mitigation if such operation is desired. In order to make that possible, reduce the reactive power requirement for flicker mitigation as well as meet utility preferences for zero reactive power exchange as a generic case and to avoid resorting to voltage control with its complications, a variable power factor reactive power control scheme was proposed. In the proposed scheme, the flicker-producing changes in active power are dealt with independent of the steady-state reactive power behavior of the WG. The proposed control scheme was tested for a spectrum of practical system configurations and demonstrated its flicker mitigation capacity.

Chapter 4

A Short-Term Energy Storage System for Wind Power Flicker Mitigation

4.1 Introduction

The use of reactive power in flicker mitigation is limited by its availability [50, 52], the grid codes limitations on WGs reactive power control capability [51] and is highly restrained by the network X/R ratio [28, 53] that are all decisive factors in determining the feasibility of reactive power control as a flicker mitigation approach.

Bearing in mind the high dependence of flicker severity on the network X/R ratio and the power factor setting of the flicker source as explained in [54], active power smoothing provides a flicker-mitigation solution that is independent of the network impedance as well as the sought renewable generator reactive power behavior.

Active power smoothing as a flicker mitigation solution was particularly studied in [28, 30]. In [28], the DC link of the full-converter synchronous generator was used as the storage device and in [30], the pitch control scheme of the DFIG wind turbine was modified to counteract the active power dips by maintaining a reserve margin for active power increase by the turbine blades. The limitations of the former can be seen in the limited energy storage capacity the machine DC link can provide and the latter necessitates a sacrifice of the energy captured by the wind turbine and both techniques require distributed controls at each individual WG in a wind farm. Due to the outlined limitations, the aforementioned works only targeted the tower-shadow fraction of the flicker-inducing active power fluctuations. The flicker contribution from that fraction is deemed highly alleviated by the contemporary WG variable speed control [32] rendering the wind speed fluctuations the major source of induced flicker emission. With respect to a short-term ESS, the works of [55, 56, 57, 58, 59, 60] signified the capability of flywheel-based and supercapacitor-based ESSs in WG output power leveling in very short time frames. Particularly, the works of [56, 57, 58] proposed a hybrid long-term (battery-based)/short-term (supercapacitor-based) ESS to smooth the wind power fluctuations that are faster than the response time of the battery unit. The presence of the supercapacitor unit was shown by a week-long study to remarkably extend the life time of the battery unit [58]. Yet, the question of necessary controls, sizing foundation and physical need for the short-term ESS from a voltage quality perspective was yet to be posed as no power quality benchmark assessment was in question.

This chapter complements the above mentioned studies by the following contributions: 1) proposing a combined control/management algorithm for a supercapacitor-based short-term ESS to allay the wind power short-term power quality concern of voltage flicker and 2) proposing an ESS power sizing methodology as a function of the wind speed average and turbulence intensity at the installation site. The chapter concludes the results by deducing a network-equivalent-based foundation for determining the superior performance that the ESS can present over the currently adopted reactive-power-based flicker mitigation approaches.

The nature of the wind power fluctuations addressed in this work necessitates the utilization of a fast-response, high efficiency and high number of charge/discharge cycles storage technology. A supercapacitor storage unit manifests as a promising choice to attain those features [58, 59] and is hence considered as the anticipated storage technology.

4.2 Storage System Configuration

In this section, the details of the ESS configuration are presented in terms of storage topology, power-electronic interface requirement and proposed control.

4.2.1 Centralized vs. Distributed ESS Topology

A thorough performance comparison of centralized (at the wind farm point of grid connection) and distributed (storage unit connected to the DC link of each WG converter) wind power ESSs was carried out in [61]. The two schemes were shown to be equally capable of smoothing short-term wind power fluctuations with an anticipated reduction in ESS power rating for centralized storage as the number of WGs increases, benefiting from the smoothing effect of multi-WG assemblies in a wind farm. Moreover, contemporary WGs are typically featured either as DFIGs or fully-rated converter synchronous generators. In the fully-rated converter WGs, the total wind power generation traverses the fully-rated converter, while the converter is rated at 20 % to 30 % of the machine rating in DFIGs. Therefore, if storage is to be connected to the machine DC link as in [57, 62], the storage allowed rating in case of the DFIG is lower and limited by the rating of the converter (20 % to 30 % of the machine rating).

Taking the above factors into consideration, a centralized ESS is thought to be more practical and is assumed for generalization purposes. Two power electronic converters are thus employed, an AC/DC converter and a DC/DC converter, Figure 4.1.

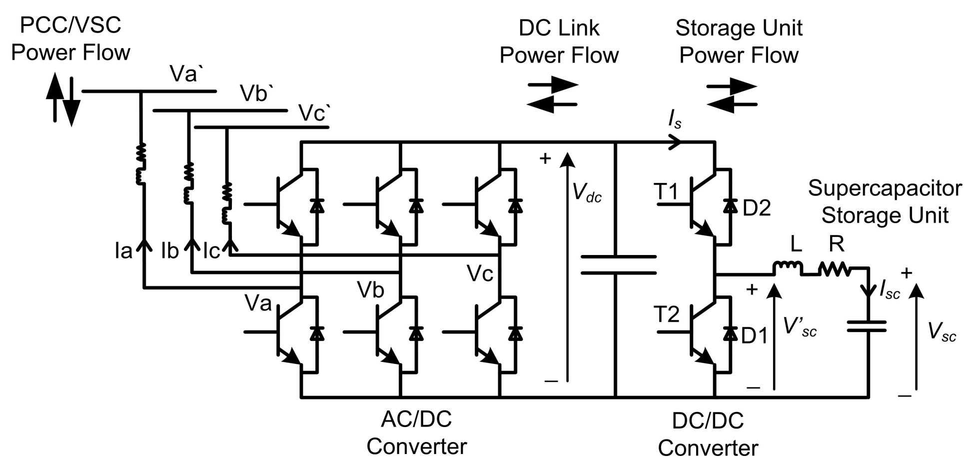

Figure 4.1: Employed ESS configuration.

4.2.2 AC/DC Voltage Source Converter (VSC)

The control of the VSC is implemented in decoupled two-coordinate *dq* frame such that the active and reactive power flows of the ESS are controlled independently. The basic equations describing the VSC control are the same as those explained in Appendix D. The VSC is controlled such that a constant DC link voltage is maintained, while the DC/DC converter assumes control of the supercapacitor power flow. The VSC control scheme is shown in Figure 4.2.

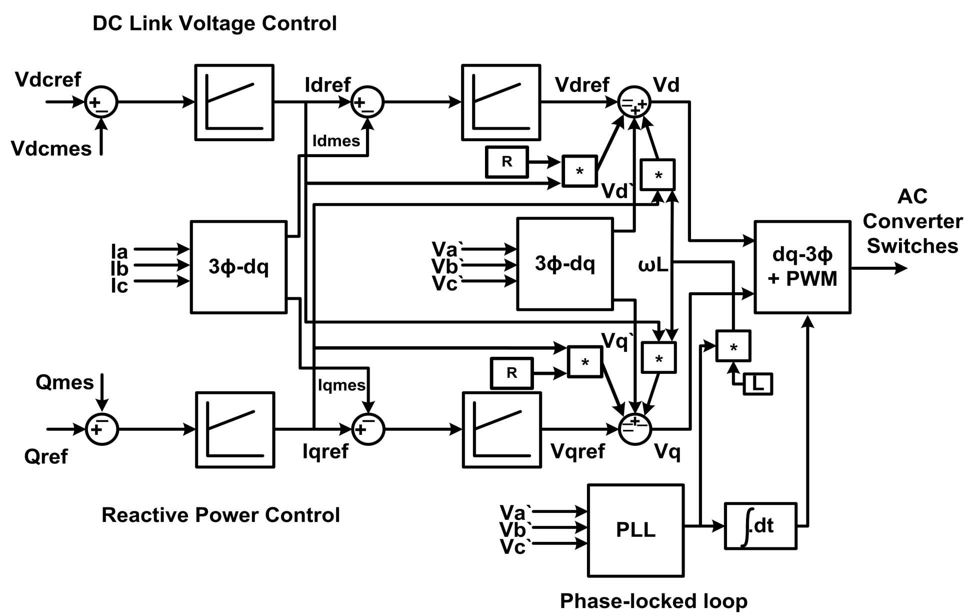

Figure 4.2: ESS VSC control.

4.2.3 DC/DC Converter

A two-quadrant converter controls the flow of power from and to the supercapacitor unit. When switch T1 (Figure 4.1) is on, the DC link voltage is imposed on the supercapacitor branch and the flow of power is from the PCC to the supercapacitor unit, while if T2 is on, the current reverses direction and the voltage across the storage unit branch is zero. If switch T2 is switched off, the current flowing in the switch is conducted through D2 until it drops to zero transferring power from the supercapacitor to the PCC. The average voltage across the storage unit branch and the unit current are governed by (4.1),

$$V'_{sc} = DV_{dc} \tag{4.1a}$$

$$I_{sc} = \frac{I_s}{D} \tag{4.1b}$$

where V'_{sc} is the average storage branch voltage, D is the duty cycle, V_{dc} is the DC link voltage, I_{sc} is the supercapacitor branch current and I_s is the average input current to the DC/DC converter. Due to the high computational burden of the required Pst-calculation 10-minute simulation runs, an average switching model utilizing (4.1) was used in a subset of the presented results in this chapter.

4.3 Proposed Storage Sizing Methodology

4.3.1 ESS Sizing Requirements

The estimated amplitude and duration of the wind power flicker-producing fluctuations are employed as the determinants of the ESS power and energy ratings. Wind power flicker-producing fluctuations can be classified either as turbine-dimensions-dependent torque oscillations or impacts of wind speed fluctuations as described earlier in Chapter 2. The amplitude of wind power variations due to the torque oscillations is a function of the wind turbine mechanical design (tower height, tower radius etc. [41], Appendix B) rendering it difficult to quantify without precise knowledge of the wind turbine detailed specifications and the resulting flicker contribution is lower than that resulting from wind speed variations under contemporary WG speed control [32]. A comparison between the impacts of the two flicker-producing components on the active power generated by the WG is demonstrated in Figure 4.3. Figure 4.3 demonstrates the PSD of both the wind speed data and the WG active power output with and without the inclusion of the 3p torque oscillations in the wind turbine model. As can be seen from Figure 4.3 (b) and with the aid of the dashed horizontal lines, the amplitude of active power fluctuations due to the 3p torque oscillations is smaller than that of the wind speed variations above 0.05 Hz and hence a flicker mitigation scheme based on torque oscillations will result in only partial alleviation of the flicker severity [28, 30].

The amplitude of short-term wind power fluctuations due to wind speed variations can rather be attributed to the wind power installation site and can hence be estimated

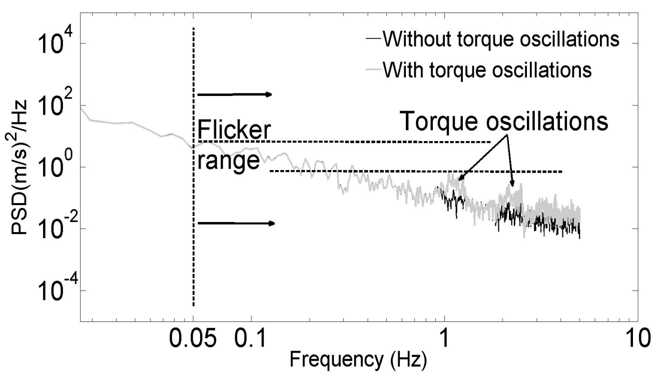

(a)

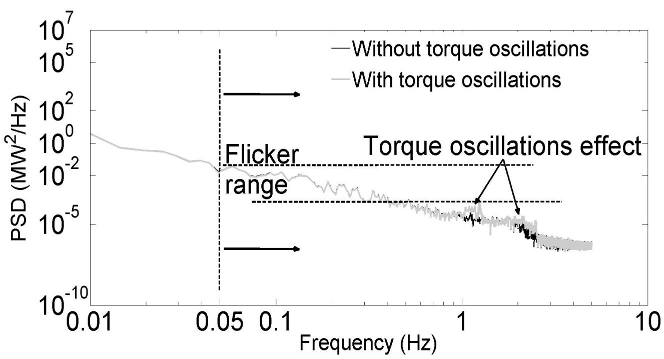

(b)

Figure 4.3: Impact of the 3p torque oscillations on output power of a WG: a) wind speed data PSD with and without the 3p toque oscillations effect, b) output power PSD with and without the 3p toque oscillations effect (10 m/s, 2 MW DFIG).

from historical wind data. More specifically, by knowledge of the dominant average wind speed (determined from historical short-term wind data) and the wind turbulence intensity (a function of the installation site terrain), an estimation of the likely magnitude variations in wind speed can be derived and a translation into wind power output level changes can be employed to define the power sizing and consequently the energy sizing of the short-term storage unit.

4.3.2 Power Sizing

The relation between the output power of a WG and wind speed at the turbine blades is governed by (4.2) which can be expressed as (4.3) in the MPPT range (below rated wind speed and at maximum power coefficient). This is the range most important for flicker studies, as the pitch control is reported to help alleviate the flicker severity [23].

$$P_w = 0.5\rho C_p A v^3 \tag{4.2}$$

$$P_w = kv^3, \qquad where \qquad k = \frac{P_{wrated}}{v^3_{rated}} \tag{4.3}$$

Where P_{wrated} is the rated WG power and v_{rated} is the rated wind speed and the rest of symbols as defined in Sec.2.4.1.

For any change in wind speed, the post-change wind speed value (v_{new}) can be expressed in terms of the pre-change value (v_{old}) and the magnitude of the change (Δv), (4.4). Similarly, the wind power generation can be expressed in terms of the pre-change value (P_{old}), post-change value (P_{new}) and magnitude of change in wind power output (ΔP) as in (4.5) and an expression for the magnitude of change in wind power can be written in terms of the wind speed change as in (4.6).

$$v_{new} = v_{old} + \Delta v \tag{4.4}$$

$$P_{new} = P_{old} + \Delta P \tag{4.5}$$

$$kv^3_{new} = kv^3_{old} + kM, \qquad where \qquad M = v^3_{new} - v^3_{old} \tag{4.6}$$

The term kM in (4.6) represents the magnitude of change in wind power (ΔP) that needs to be offset should it occur at a flicker-producing frequency. In order to quantify the value of M in (4.6) and hence the likely flicker-producing magnitude changes in wind power, the turbulence intensity at the installation site and the average wind speed are utilized. Wind turbulence is linked to the average wind speed by the standard deviation σ (4.7) and the standard deviation by its definition signifies the magnitude of likely deviations of a set of data from its average value. A deviation from the average wind speed value is thus likely to be $\pm\sigma$ of the recorded wind data and (4.8) can express the post-change wind speed value,

$$t_{ur} = \frac{\sigma}{\bar{v}} \tag{4.7}$$

$$v_{new} = \bar{v} \pm t_{ur}\bar{v} \tag{4.8}$$

where t_{ur} is the wind speed turbulence intensity, σ is the standard deviation of the wind data and $\bar{v}$ is the average wind speed.

M as expressed in (4.6) can either be a positive or a negative value, but given the cubic exponent effect (4.2), a higher magnitude change in wind power is seen for a positive change in v ($\Delta v = +t_{ur}\bar{v}$) or an increase in wind speed ($v_{old} < v_{new}$) rather than for a negative change of the same magnitude ($\Delta v = -t_{ur}\bar{v}$). The likely magnitude increase in wind speed is therefore used to define the storage unit power rating.

With $\bar{v}$ being the reference wind speed around which changes are to be offset by storage charging and discharging, the value of M can be determined by (4.9) and the power rating of the storage unit calculated accordingly in terms of the installed WG rating, average wind speed and turbulence intensity by (4.10),

$$M = (\bar{v} + t_{ur}\bar{v})^3 - \bar{v}^3 \tag{4.9}$$

$$P_{res} = kM = \frac{P_{wrated}}{v_{rated}^3}(t_{ur}\bar{v}^3(3 + 3t_{ur} + t_{ur}^2)) \tag{4.10}$$

where P_{res} is the power rating of the storage unit.

The storage unit power rating per the proposed methodology is plotted in Figure 4.4 as a function of the average wind speed and the turbulence intensity for the test 2 MW DFIG. It can be clearly seen that the higher the wind speed average and the higher the turbulence intensity, the higher the required storage unit power rating. This is in line with wind power flicker severity behavior that increases as both wind speed average and turbulence intensity increase (increase in magnitude of wind power fluctuations as was shown in Figure 2.11).

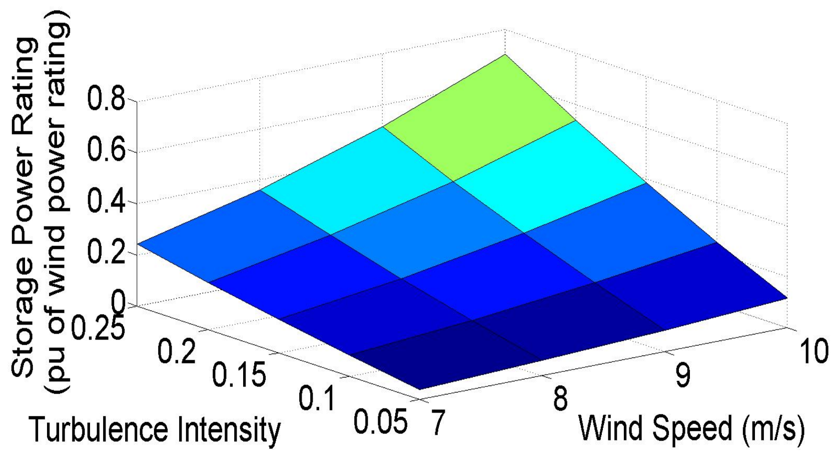

Figure 4.4: Proposed storage unit power rating as a function of wind speed average and wind turbulence intensity (2 MW DFIG).

4.3.3 Energy Sizing

In terms of long-term storage energy sizing, optimization studies are typically carried out given a wind farm output scheduling scheme, daily forecasted wind profiles and a minimization of a cost function [63, 64]. Energy sizing optimization in that case is seen in light of the network load profile variations and consequent wind farm dispatch command. In case of the short-term ESS studied in this work, the load profile is constant and an optimal energy sizing for the ESS requires a precise analysis of the higher-frequency spectrum of wind speed data over extended time periods (months as done in [63] for the lower-frequency spectrum). Another approach is to employ a mathematical time-domain representation of the wind speed in the short-term frame of study (order of seconds), yet, no standard mathematical model is agreed upon to describe the time dependency of the short-term fluctuations [65, 66]. Thus and in order to release the energy sizing of the short-term ESS from the wind speed modeling dependency and given that the economical concern in the 10-minute frame is allayed [67], the short-term energy sizing has previously been done empirically as in [58], arbitrarily as in [56, 68, 69] or operational requirements were set forth as criteria to define the maximum energy storage capacity of the ESS as in [57]. A combination of the two approaches utilized in [57] and [58] are employed in this work. First an operational requirement defines the storage energy rating E_{res} by the ability of the ESS to store its rated power P_{res} under the longest possible flicker-producing change at a frequency of 0.05 Hz and a duration of 20 s. Second, a parametric study is carried out by reduction of the ESS energy rating to observe the Pst sensitivity to the rating changes.

The required energy rating for the ESS as per the above methodology is plotted in Figure 4.5 as a function of the wind speed average and the turbulence intensity.

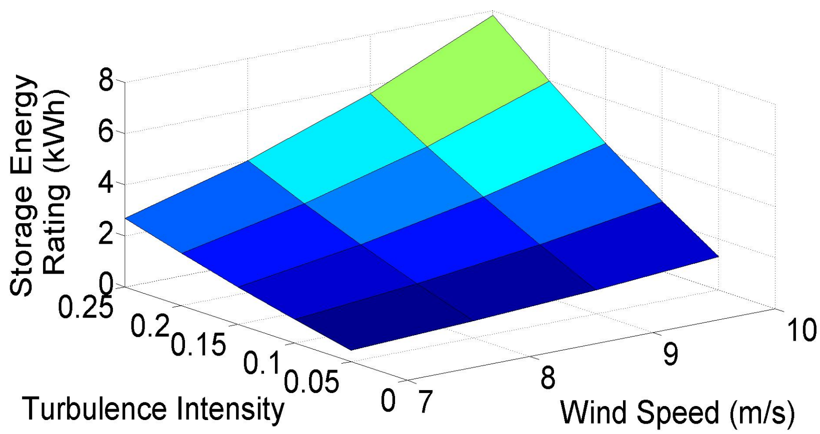

Figure 4.5: Proposed storage unit energy rating as a function of wind speed average and wind turbulence intensity (2 MW DFIG).

4.4 Storage Unit Flicker Mitigation and Management Control Algorithm

The proposed control for the DC/DC converter is realized in two levels: 1) a level at which the storage duty cycle D is controlled (current control loop), and 2) a level at which the storage unit power consumption is controlled (power control loop).

4.4.1 Current Control Loop

A current control loop acts on the DC/DC converter switches to track the supercapacitor reference current setting. The supercapacitor is represented by a capacitance and a series resistor in wind power studies as indicated in [56, 62] and is discharged through an inductor. By considering that representation, the states of the DC/DC converter of Figure 4.1 can be written as (4.11),

$$V_{dc}(t) = L\frac{dI_{sc}(t)}{dt} + I_{sc}(t)R + \frac{1}{C}\int I_{sc}(t)dt \tag{4.11a}$$

$$0 = L\frac{dI_{sc}(t)}{dt} + I_{sc}(t)R + \frac{1}{C}\int I_{sc}(t)dt \tag{4.11b}$$

where C is the supercapacitor stack capacitance, R is its series resistance and L is the discharging inductance.

The small-signal representation defining the operation of the current controller can be found by introducing small changes in the supercapacitor current $\Delta i_{sc}(t)$, duty cycle $\Delta d(t)$ and the input voltage $\Delta v_{dc}(t)$ (4.12).

$$V_{dc} + \Delta v_{dc}(t) = L\frac{d(I_{sc} + \Delta i_{sc}(t))}{dt} + (I_{sc} + \Delta i_{sc}(t))R + \frac{1}{C}\int (I_{sc} + \Delta i_{sc}(t))dt \tag{4.12a}$$

$$0 = L\frac{d(I_{sc} + \Delta i_{sc}(t))}{dt} + (I_{sc} + \Delta i_{sc}(t))R + \frac{1}{C}\int (I_{sc} + \Delta i_{sc}(t))dt \tag{4.12b}$$

The averaged states relation over a switching cycle can then be obtained as a function of the duty cycle D (4.13).

$$(D + \Delta d(t))(V_{dc} + \Delta v_{dc}(t)) = L\frac{d(I_{sc} + \Delta i_{sc}(t))}{dt} + (I_{sc} + \Delta i_{sc}(t))R + \frac{1}{C}\int (I_{sc} + \Delta i_{sc}(t))dt \tag{4.13}$$

With V_{dc} being controlled by the AC/DC converter controls, the change $\Delta v_{dc}(t)$ can be neglected and by removing the products of the DC quantities and small changes in (4.13), the small-signal relation between the duty cycle and the supercapacitor current can be written as (4.14).

$$G_1(s) = \frac{\Delta i_{sc}(s)}{\Delta d(s)} = \frac{V_{dc}Cs}{LCs^2 + RCs + 1} \tag{4.14}$$

The characteristic equation for the current control loop is thus obtained by multiplying (4.14) by the pulse-width-modulation gain PWM_{gain} and a unity feedback (4.15).

$$1 + PWM_{gain}G_1(s) = 0 \tag{4.15}$$

The closed-loop transfer function of the current controller after the addition of a controller $C_1(s)$ is in the form of (4.16), Figure 4.6.

$$T_1(s) = \frac{C_1(s) PWM_{gain} G_1(s)}{1 + C_1(s) PWM_{gain} G_1(s)} \tag{4.16}$$

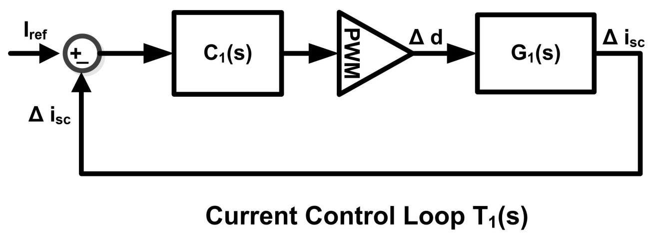

Figure 4.6: Current control loop.

The current control loop responds to a current reference set by an outer control loop (power control loop) whose controlled plant and characteristic equation are defined by a simultaneous flicker mitigation and storage management control algorithm as described below.

4.4.2 Power Control Loop

The active power command to the storage unit is formulated such that two purposes are fulfilled, 1) offsetting undesired wind power flicker-producing fluctuations at the PCC (achieved by a flicker power command $P_{flicker}$), and 2) continuously maintaining a level of stored energy in the unit to allow the sought offsetting (achieved by a storage management charge/discharge power command $P_{char-disch}$ defined over an ESS management time frame.)

Flicker power command:

$P_{flicker}$ is simply obtained by filtering the measured P_w by means of a high-pass filter with a time constant τ_1 determined based on a cutoff frequency of 0.05 Hz (start of the flickering range), (4.17). $P_{flicker}$ represents the fluctuations in wind power that if injected into the connection network will result in a flicker contribution.

$$P_{flicker}(s) = P_w(s)\left(\frac{\tau_1 s}{1 + \tau_1 s}\right) \tag{4.17}$$

Management power command:

The purpose of this command is to ensure that the storage unit does not reach its capacity limits nor does it account for a flicker contribution from the storage management process. To achieve that, $P_{char-disch}$ is defined as a storage management command in which changes occur at a frequency below the start of the flickering range providing control of the storage unit state of charge (SoC) and avoiding interference with $P_{flicker}$. Generation of $P_{char-disch}$ can be realized through two stages: 1) a stage where the SoC of the storage unit and the amount of energy to be charged or discharged are determined, and 2) a low-pass filtering stage to restrict the management command to a prescribed range of frequencies.

To control the SoC of the storage unit, a threshold value of the supercapacitor voltage $V_{scthreshold}$ serves as a reference point to the management scheme to constantly maintain a corresponding level of stored energy $E_{scthreshold}$ in the storage unit based on the relation of (4.18). $E_{scthreshold}$ and therefore $V_{scthreshold}$ can be defined by the ratio of a likely positive wind power change (energy to be charged) to a likely negative wind power change (energy to be discharged).

$$SoC_{scthreshold} = \frac{E_{scthreshold}}{E_{res}} = \frac{V^2_{scthreshold} - V^2_{min}}{V^2_{max} - V^2_{min}} \tag{4.18}$$

Where V_{max} and V_{min} are the maximum and minimum operating voltages of the installed supercapacitor unit respectively. The pre-filtered management power command $P_{mang}(t)$ is in the form of (4.19), where 40 stands for the length of time over which the discharge/charge energy command is executed. A management frame of 40 s was found appropriate allowing changes of a maximum of 0.025 Hz to be seen in $P_{char-disch}$ utilizing a low-pass filter of time constant τ_2, (4.20).

$$P_{mang}(t) = (0.5 * C * (V^2_{sc}(t) - V^2_{scthreshold}))/40 \tag{4.19}$$

$$P_{char-disch}(s) = P_{mang}(s)(\frac{1}{1+\tau_2 s}) \tag{4.20}$$

The power control loop minimizes the error $e_p(s)$ between the combined active power command $(P_{flicker}(s) - P_{char-disch}(s))$ and the measured storage active power consumption $P_{scmes}(s)$, (4.21).

$$e_p(s) = P_{flicker}(s) - P_{char-disch}(s) - P_{scmes}(s) \tag{4.21}$$

The power control loop thus comprises two feedback signals (the measured consumption and the discharge command), both are derived from the measured supercapacitor current. A small-signal model can be developed for the power control loop by introducing small changes in the two signals (active power signals).

Neglecting the power consumed in the supercapacitor series resistance, (4.22) describes the active power consumption of the storage unit and by introducing a small signal change Δp_{scmes} in P_{scmes} and removing the DC terms and products of small signals, (4.23) describes the small-signal behavior of the first feedback signal.

$$P_{scmes}(t) = I_{sc}(t)V_{sc}(t) \tag{4.22}$$

$$P_{scmes} + \Delta p_{scmes}(t) = (I_{sc} + \Delta i_{sc}(t))(V_{sc} + \Delta v_{sc}(t)) \tag{4.23a}$$

$$\Delta p_{scmes}(t) = \Delta i_{sc}(t)V_{sc} + I_{sc}\Delta v_{sc}(t) \tag{4.23b}$$

The small-signal behavior of the second feedback loop can be derived by introducing a small change Δv_{sc} in V_{sc} in (4.19). This leads to a small change Δp_{mang} in P_{mang} described by (4.24).

$$\Delta p_{mang}(t) = \frac{2(0.5)(C)}{40} V_{sc}\Delta v_{sc}(t) \tag{4.24}$$

Transforming to the s-domain and substituting $\frac{1}{sC}\Delta i_{sc}(s)$ for $\Delta v_{sc}(s)$ in (4.23) and (4.24) and substituting in (4.20), the two feedback transfer functions can be written as (4.25).

$$\frac{\Delta p_{scmes}(s)}{\Delta i_{sc}(s)} = V_{sc} + \frac{I_{sc}}{sC} \tag{4.25a}$$

$$\frac{\Delta p_{char-disch}(s)}{\Delta i_{sc}(s)} = \frac{V_{sc}}{40s(1+\tau_2 s)} \tag{4.25b}$$

Therefore, the equivalent of the feedback signal is (4.26).

$$H_2(s) = V_{sc}(1 + \frac{1}{40s(1+\tau_2 s)}) + \frac{I_{sc}}{sC} \tag{4.26}$$

The power control loop is shown in Figure 4.7 and the detailed small-signal model is shown in Figure 4.8.

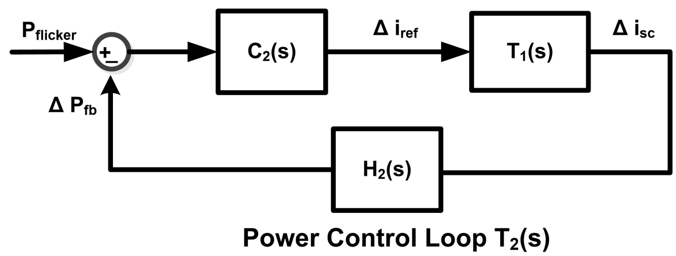

Figure 4.7: Power control loop.

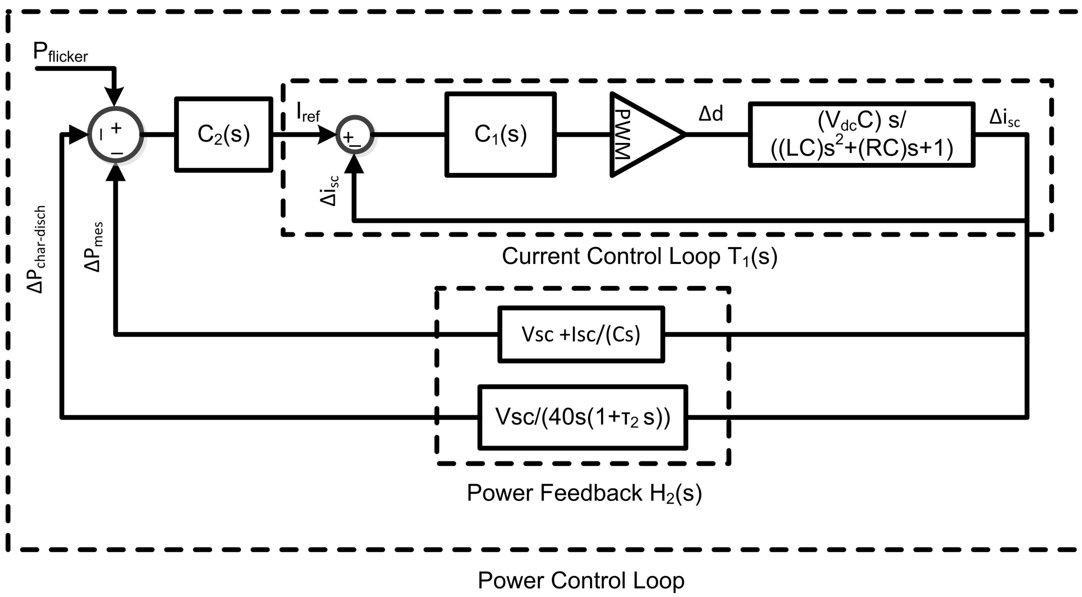

Figure 4.8: Storage system control small-signal model.

The characteristic equation for the power control loop is thus given by (4.27).

$$1 + H_2(s)T_1(s) = 0 \tag{4.27}$$

The full system transfer function after the addition of a power control loop controller C_2 is given by (4.28).

$$T_2(s) = \frac{C_2(s)T_1(s)}{1 + C_2(s)T_1(s)H_2(s)} \tag{4.28}$$

The small-signal model was verified by testing the response of the two systems (actual power system and derived small-signal model) for the same input power step reference, the results are shown in Sec.4.5.1 based on the system parameters given in the same section. The small-signal model is used in the controller design to ensure system stability for any frequency in the reference input to the storage control system $P_{flicker}$. This is illustrated by bode plots in Sec.4.5.1 as well.

4.4.3 Controller Limits and Design Procedure

A commercial supercapacitor cell [56] is the basis of the data presented in this work. The rated voltage of the cell is 400 V with a capacitance of 0.58 F and an equivalent series resistance (ESR) of 0.6 Ω. The different parameters of the storage unit and controls are specified as follows:

1. Voltage Limits: The maximum voltage is determined by the DC link voltage V_{dc} and the minimum voltage is controlled by the limits on the duty cycle and the converter and is determined in this work by limiting the maximum power loss in the ESR occurring at I_{max} to $0.1P_{res}$.

2. Current Limits: The maximum current I_{max} occurs as the rated power is delivered to the storage unit at the unit minimum voltage and is calculated as in (4.29).

$$I_{max} = \frac{P_{res}}{V_{min}} \tag{4.29}$$

3. Capacitance: The equivalent capacitance of all series and parallel cells is determined by the energy rating of the supercapacitor unit and the operating voltage limits, (4.30).

$$C = \frac{2E_{res}}{V_{max}^2 - V_{min}^2} \tag{4.30}$$

The proposed storage system performance is demonstrated in the next section on a single 2 MW DFIG unit as a base case and later on a multi-WG farm connected to the detailed test distribution network.

4.5 Simulation Results

Numerous simulations of the ESS were necessary in order to thoroughly verify the system performance and to conduct parametric studies for comparative analyses. More specifically, the following three sets of simulations were decided upon:

1. Simulations 1: Storage model performance verification on a single 2 MW DFIG unit connected to the simplified network equivalent representation as a base case and a design example.

2. Simulations 2: Parameter sensitivity analyses for the base case.

3. Simulations 3: Testing of three storage-equipped wind farm integration scenarios to the detailed distribution network by testing the storage-equipped integration for wind power capacities of 6 MW, 8 MW and 10 MW at Bus 16 of the detailed distribution network of Figure 2.4.

Given the length of the simulations (10 minutes for each run), some factors were taken into consideration in models preparation in order to carry-out time-efficient simulations as well as verify the results in a different platform (real-time simulations in that context). Those factors included the number of control and electric elements and presence of the storage switches in the simulation models. The decision was to use the average model of (4.1) in lieu of the storage converter switches for the parameter sensitivity analyses of Simulations 2 and to exclude those simulations from the real-time model simulations presented in Chapter 5 as no added purpose was severed.

4.5.1 Simplified Network/ Design Example (Simulations 1 and Simulations 2)

A weak distribution network is represented by its X/R ratio and short-circuit level as seen at the point of wind power connection. The connection point characteristics are 25 kV voltage level, 30 MVA short-circuit level, and an X/R ratio of 0.52. The ESS is connected to the low-voltage side of the MV/LV transformer at 575 V. The assumed wind speed characteristics at the installation site are an average wind speed of 10 m/s and turbulence intensity of 15 %. Figure 2.8 shows the temporal and power spectral density (PSD) plots of the 10-minute wind speed data applied at the turbine blades. The corresponding ESS parameters according to the proposed sizing and design procedure are summarized in Table 4.1.

Table 4.1: Storage System Parameters

Parameter	Symbol	Value	Unit
Power Rating	P_{res}	770	kW
Energy Rating	E_{res}	4.27	kWh
Maximum Voltage	V_{max}	1150	V
Minimum Voltage	V_{min}	345	V
Maximum Current	I_{max}	2.23	kA
Total Capacitance	C	25.58	F
Threshold Voltage	$V_{scthreshold}$	790	V
Number of Series cells	—	3	—
Number of parallel cells	—	133	—
Storage stack resistance	R	0.013	Ohm
Discharging inductor inductance	L	0.01	Henry

The linearized small-signal design was conducted at values of $V_{dc} = 1150$, V_{sc}=$V_{scthreshold} =$ 790, PWM_{gain} of 0.5, I_{sc} of 975 A (capacitor current at rated storage power and $V_{scthreshold}$) and the rest of parameters as per Table 4.1. The intent was to determine the type of controller to be used such that the system stability can be maintained. The characteristic equation of the current control loop (4.15) was used to specify the current controller desired transfer function by aid of its Bode plot. It is seen from Figure 4.9 that the open-loop transfer function presents an infinite gain margin and +90° phase margin and hence a pole introduced at the origin by a proportional-integral controller does not affect the system stability as long as its phase is cancelled by the introduced zero at higher frequencies. The values for the proportional and the integral controllers were set respectively at 2 and 10 such that the phase effect of the controller pole is cancelled at a break frequency of around 5 Hz, Figure 4.9 (b). Similarly, the characteristic equation for the power controller (4.27) was used to design the power loop controller. As can be seen from the Bode plot of Figure 4.10, a proportional-integral controller with a pole at the origin would result in an unstable operation by yielding a phase of $-180°$, a proportional controller rather maintains the loop stability under all conditions and is hence employed. A comparison of the small-signal model (transfer functions used for controller design) and the large-signal model (power system measurements) response under the proposed controllers is shown in Figure 4.11. The response of the small-signal model used in the storage control design was tested by applying a step power reference change of 0.2 pu of the WG rating to both the storage power system and the s-domain small-signal corresponding model. The current signal of the small-signal model and the current measurement of the storage unit were recorded. The agreement in behavior is demonstrated by the current plot in Figure 4.11 (b).

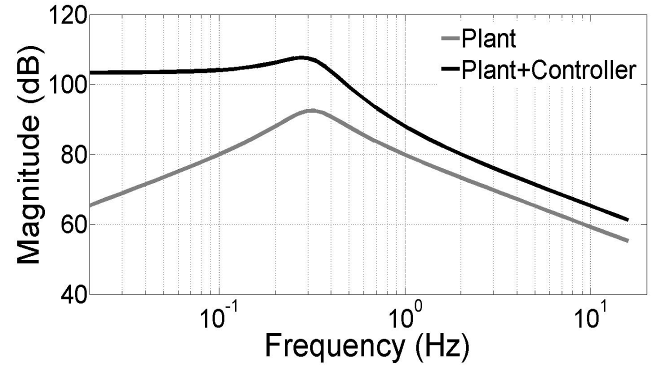

(a)

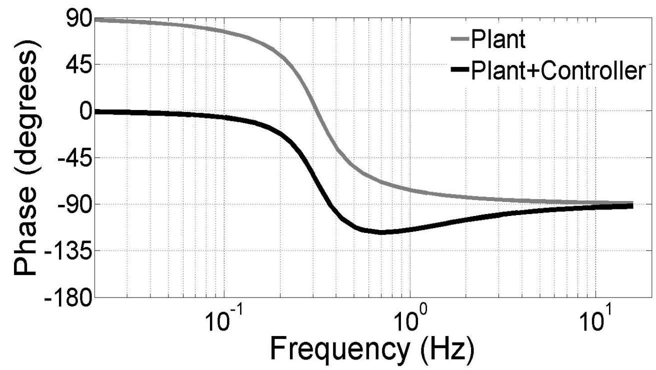

(b)

Figure 4.9: Bode plot of the current control loop: a) magnitude, b) phase.

On the supercapacitor side of the ESS, the system operation is illustrated by the plots of Figure 4.12 in pu of the storage base quantities. The corresponding operation on the VSC side (power system side) is shown in Figure 4.13. The conclusive impact of the ESS on smoothing wind power fluctuations is seen in both the active power injected from the WG into the network and the PCC RMS voltage waveform as seen in Figure 4.13(b) and Figure 4.13 (c). Figure 4.12 (b) and Figure 4.13 (a) demonstrate the change in the ESS current magnitude and direction of flow in correspondence with the flicker content in wind power generation shown in Figure 4.12 (a). The ESS ability in eliminating a target range of frequencies from the wind power generation is demonstrated by the PSD of the active power components shown in Figure 4.14 at the point of connection. The ESS power consumption is shown coinciding with that of wind power generation in the absence of the ESS in the targeted frequency range (flickering range). The presence of the ESS resulted in the elimination of a portion of the wind power frequency spectrum corresponding to the flicker-producing components in the wind speed spectrum shown

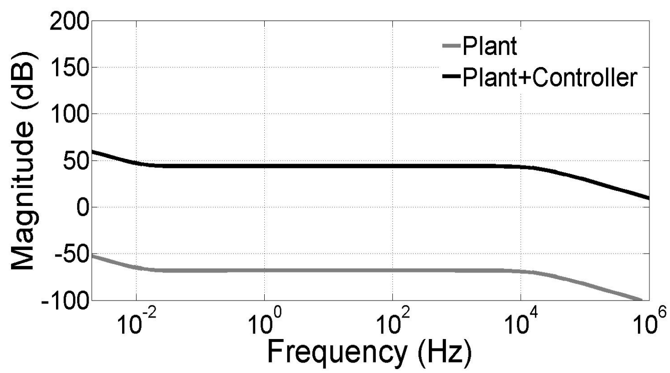

(a)

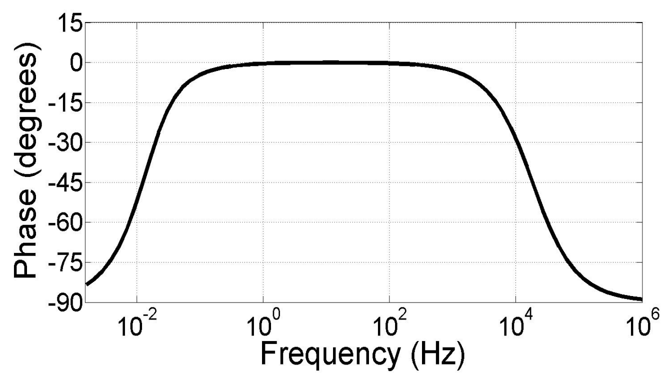

(b)

Figure 4.10: Bode plot of the power control loop: a) magnitude, b) phase.

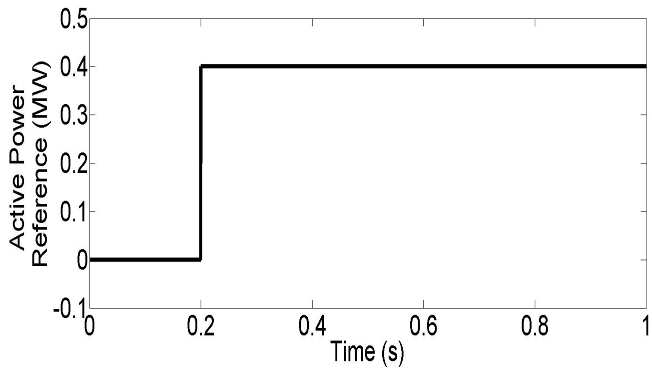

(a)

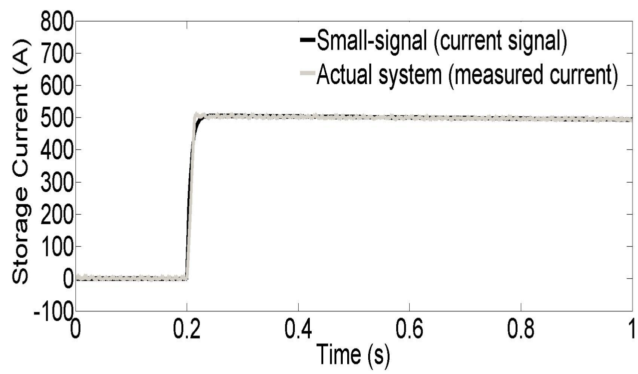

(b)

Figure 4.11: Small-signal model response: a) step change of storage active power reference, b) storage current.

in Figure 4.3 (a) and yielded wind power injection of PSD of lower amplitude in the flickering range. The ESS management power is shown to be conducted over a different range of frequencies with negligible PSD in the flicker frequency range. This is also demonstrated by the temporal plots in Figure 4.12 (d) and Figure 4.12 (e) in which the storage unit discharge command is seen to respond to the level of energy stored in the unit, yet with a less fluctuant profile due to the filtering effect in the management scheme. The efficacy of the proposed system is solidified by the alleviated flicker severity measured at the PCC and shown in Figure 4.15 in terms of instantaneous flicker level (IFL) and statistically calculated Pst.

A parametric sensitivity analysis was carried out on the ESS to determine the sensitivity of Pst to variations in the storage unit rating and management frame time length. The energy sizing of the storage unit was designed based on a 20 s charging duration under the power rating P_{res}. This was shown to be a conservative approach with a safety margin as the supercapacitor unit did not reach its capacity limits. Figure 4.16 shows the impact of reducing that rating to half and quarter its design values (2.13 and 1.07 kWh). It is seen that at half the design value, the storage unit did not reach its limits not impacting the Pst values. When the rating was further reduced, the storage unit reached its limits resulting in periods of saturation and uncompensated changes and therefore impaired flicker mitigation and higher Pst values. With respect to the management frame, a faster control of the SoC can be achieved by reducing the length of the management frame. Yet, the changes in $P_{char-disch}$ are shifted closer to the flickering range impacting the Pst values. This is demonstrated by the plots of Figure 4.17 in which the storage unit energy content and the Pst values are plotted under different lengths of the management frame (40 s, 30 s, 20 s and 10 s).

The parametric sensitivity analysis shows that both the storage energy rating and management frame length can be reduced if necessary at the expense of a potential decrease in the flicker mitigation capacity.

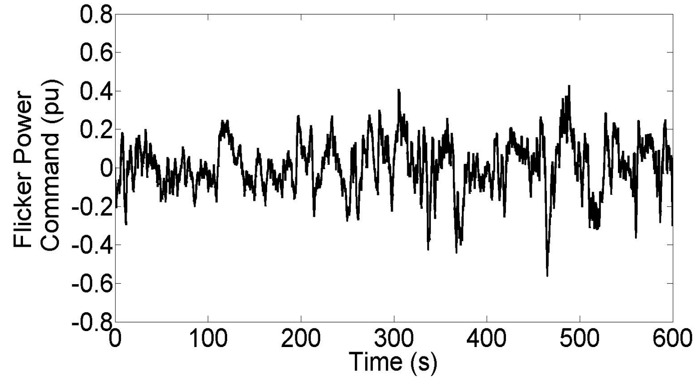
Flicker Power
Command (pu)
0.8
0.6
0.4
0.2
0
-0.2
-0.4
-0.6
-0.8
0
100
200
300
400
500
600
Time (s)

(a)

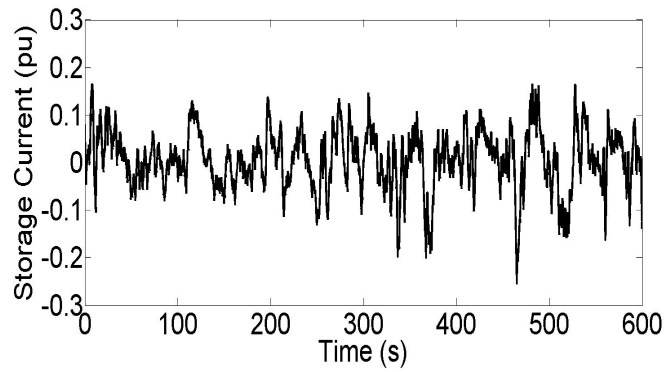
Storage Current (pu)
0.3
0.2
0.1
0
-0.1
-0.2
-0.3
0
100
200
300
400
500
600
Time (s)

(b)

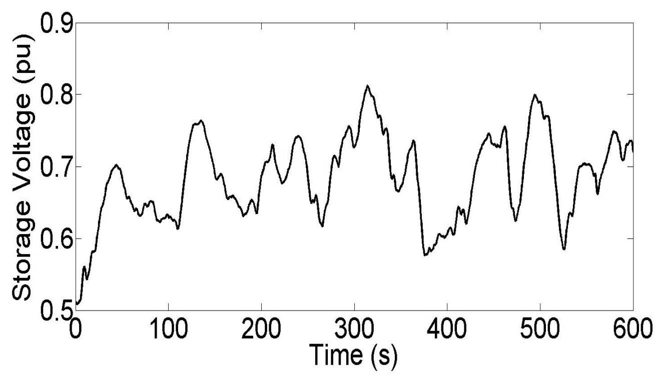
Storage Voltage (pu)
0.9
0.8
0.7
0.6
0.5
0
100
200
300
400
500
600
Time (s)

(c)

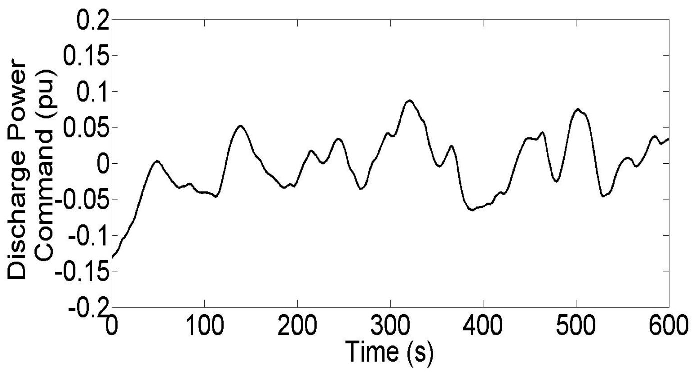

(d)

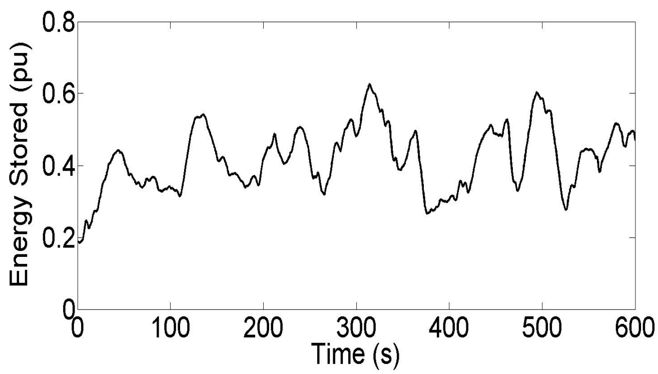

(e)

Figure 4.12: ESS operation (Supercapacitor side): (a) filtered flicker power command (b) supercapacitor current, (c) supercapacitor voltage, (d) storage management discharge power command,(e) energy content of the supercapacitor unit. Units in pu of storage base quantities in Table 4.1.

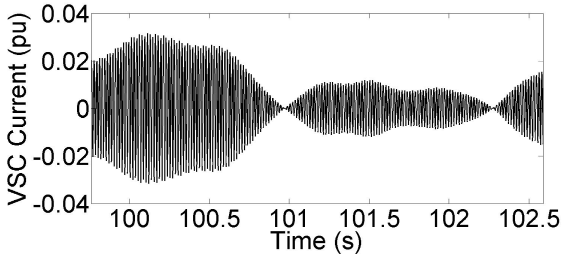

Short-term VSC current 1

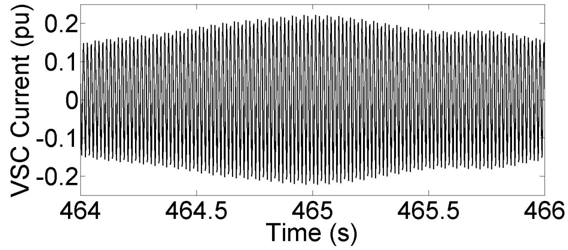

Short-term VSC current 2

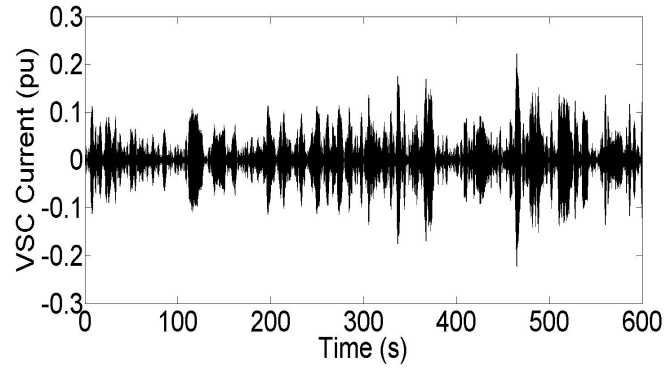

Long-term VSC current
(a)

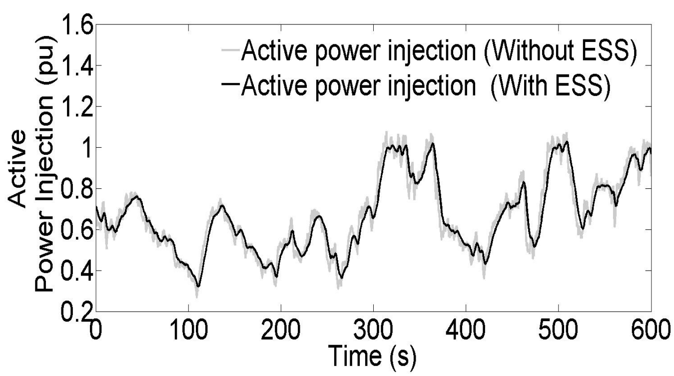

(b)

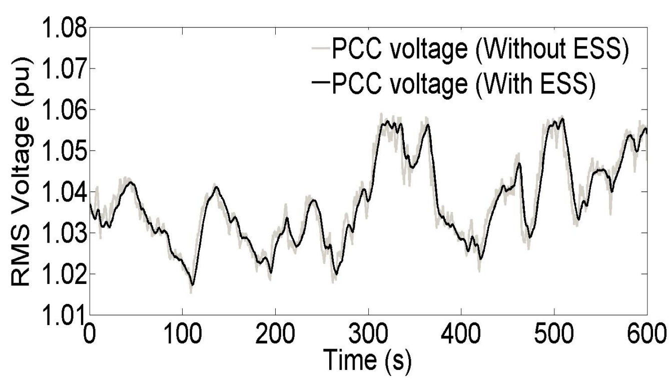

(c)

Figure 4.13: ESS operation (VSC side): (a) VSC current short-term and long-term plots, (b) injected active power, (c) PCC voltage profile. Units in pu of WG base quantities (2 MW, 575 V).

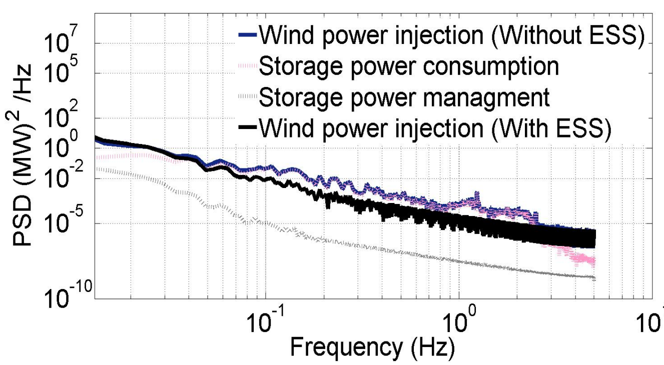

Figure 4.14: Power spectral density of active power components.

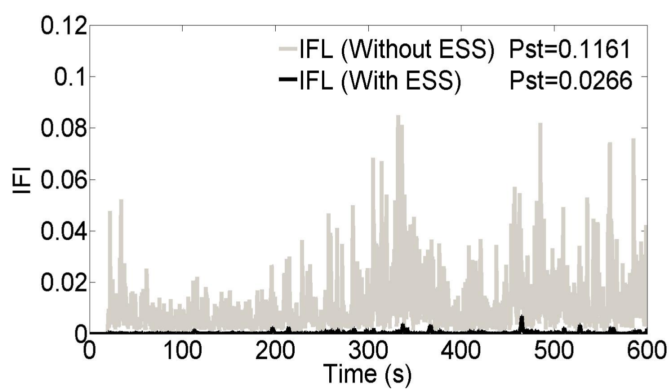

Figure 4.15: Flicker measurement at the PCC with and without the ESS.

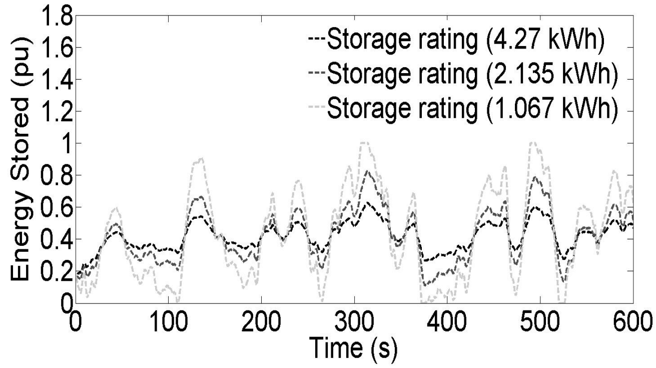

(a)

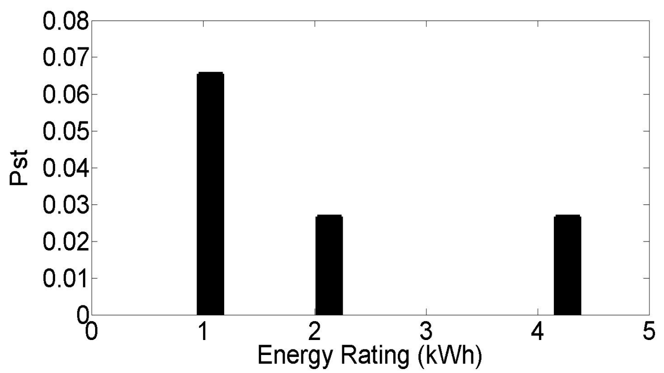

(b)

Figure 4.16: Pst sensitivity to energy rating: (a) energy stored, (b) Pst values (management frame of 40 s).

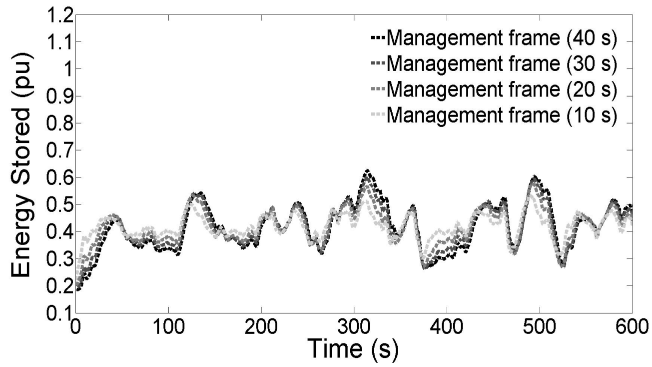

(a)

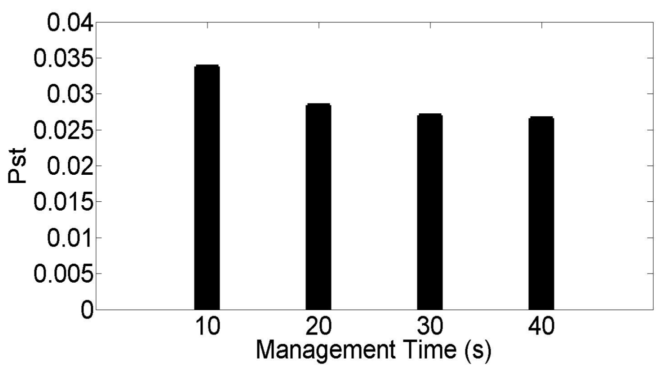

(b)

Figure 4.17: Pst sensitivity to management frame: (a) energy stored, (b) Pst values (4.27 kWh energy rating).

4.5.2 Detailed Distribution Network (Simulations 3)

An ESS is a likely resort to relieve flicker severity if reactive power control by WGs is not allowed by the grid code or contemplated by the generators. Yet, in other situations, where reactive power compensation is a potential solution, the reactive power consumed (a function of the network X/R ratio) along with the increase in line currents and losses could be weighed against the installation of an ESS taking the expected impact on flicker mitigation into consideration. To serve that purpose, storage-equipped wind power generation is compared to three salient flicker mitigation alternatives reported in literature, namely: 1) voltage control 2) fixed leading power factor control (continuous absorption of reactive power by the WGs) and 3) variable power factor control (steady-state unity power factor for low-frequency active power changes, and non-unity for higher-frequency flicker-producing active power changes), as described in Chapter 3 [53]). The flicker measurements are conducted at Bus 16 of the detailed distribution network of Figure 2.4. Three wind power rating scenarios were assumed in order to obtain results for different short-circuit capacity ratios. More specifically, the number of generators was increased by one unit at a time from 3 to 5 (6 MW to 10 MW) creating three short-circuit capacity ratios (5, 3.6 and 3). The Pst values were calculated for each case and were plotted in Figure 4.18 vs. the wind power capacity.

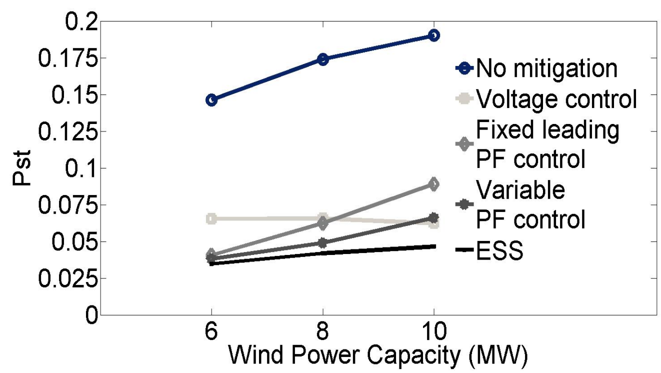

Figure 4.18: Pst values vs. wind power capacity at Bus 16 of the detailed network.

The prime observation regarding Figure 4.18 is that the mitigation capability of one scheme with respect to another changed by change of wind power capacity. The ESS resulted in the lowest Pst values under all scenarios and was approached by fixed leading power factor and variable power factor control as the wind power capacity decreased. The ESS and voltage control were the least sensitive approaches to wind power capacity changes with negligible variation in resulting Pst values as the wind power rating changed.

An explanation for the shown trends is traced by analysis of the equivalent two-bus system with Bus 16 being the sending end with voltage magnitude V_{se}, V_g being the receiving-end grid voltage, δ being the voltage vectors angle difference, P and Q being the active and reactive power flows at Bus 16 and R and X being the resistance and reactance of the equivalent impedance seen at Bus 16. Equations (4.31) and (4.32) respectively represent the real and imaginary parts of the power flow equation for such system.

$$V_{se}(V_{se} - V_g cos\delta) = PR + QX \tag{4.31}$$

$$V_g V_{se} sin\delta = PX - QR \tag{4.32}$$

As δ diminishes to approach negligible values, as assumed in distribution networks and explained in Chapter 3, (4.31) is approximated by (4.33) to represent the change in voltage magnitude between the two buses. Equation (4.33) is the basis of voltage changes compensation by power factor control at the PCC (fixed leading power factor and variable power factor control). Equation (4.33) assumes a negligible value of δ and the value of δ increases by both the increase of active wind power generation as well as the increase in reactive power absorption by the WG, Figure 4.19.

$$V_{se} - V_g \approx \frac{PR + QX}{V_{se}} \tag{4.33}$$

In fixed leading power factor, reactive power compensates the entire wind power, while in variable power factor control, (4.33) is split into two spectra, one outside the flicker frequency range (average wind power generation and slow changes of high magnitude) and the other covering the flicker range (faster wind power changes with lower magnitude), thus treating the steady-state voltage level and flicker independently. The total wind power generation (Figure 4.13 (b)) is essentially a non-flicker producing active power quantity over which a flicker-producing content is superimposed (Figure 4.12 (a)). Assuming the total wind power generation to be P_1, and the amplitude of a flicker-producing change to be P_2, then $P1 \geq P2$. Therefore, when the flicker component is treated independently (without resorting to a leading power factor), a smaller value of δ is involved in (4.33), as compared to the case of fixed leading power factor, increasing the validity of (4.33) and leading to variable power factor maintaining superior performance over fixed leading power factor for all cases. Both schemes are seen to have a decreasing flicker mitigation capacity as the wind power capacity increases, this is again due to the increasing value of δ and the consequent impaired validity of (4.33). The mitigation capability of the ESS is approached by mitigation techniques based on (4.33) as δ approaches zero and higher accuracy of (4.33) (3 units case). $\delta = 1.02°$ under leading power factor control for the 3 units case and increases to $7.09°$ for the 5 units case.

The Pst values under voltage control and the ESS were the least sensitive to wind

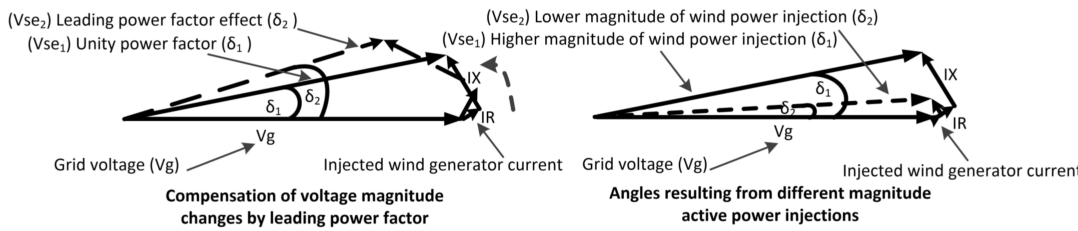

Figure 4.19: Vector diagram of voltage changes after active power injection.

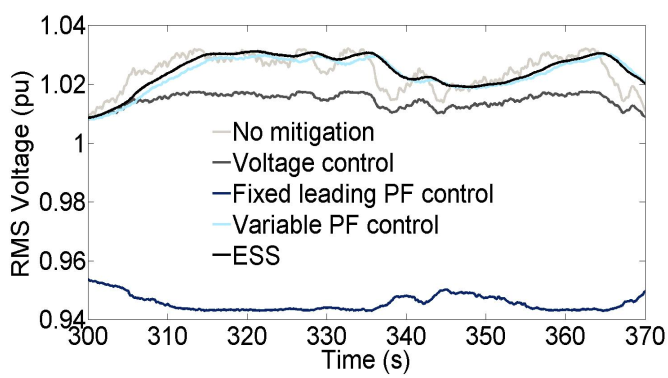

Figure 4.20: Short-term profile of Bus 16 RMS voltage under different flicker mitigation approaches (6 MW rating scenario).

power size changes due to the voltage feedback nature of the voltage control process (non-existent in power factor control) and the independence of the ESS control of the distribution line parameters and approximations. The mitigation capability of both methods is expected to be sensitive to the voltage controller gain (defined voltage/reactive power droop characteristics) and the storage control gains.

A short-term RMS voltage profile under all the mitigation alternatives for the case of 6 MW wind power rating is shown in Figure 4.20.

4.6 Conclusion

In this chapter, a supercapacitor-based ESS was proposed as a solution to the voltage flicker problem in weak distribution networks with wind power integration. It was shown that a power sizing methodology based on wind speed average and turbulence intensity is appropriate for alleviating the voltage impacts of the flicker-producing changes in the generated wind power. Filtering-based control algorithms were shown effective in both alleviating the wind power flicker severity and properly managing the ESS. When compared with other flicker mitigation approaches, the ESS was found to have superior flicker mitigation capability. Nevertheless, the degree of superiority that the ESS presented was shown to be related to the connected wind power capacity at the given connection point and subsequently the validity of approximations assumed in power-factor-based flicker mitigation approaches. The choice of a flicker mitigation approach should thus be contemplated in light of the planned wind power capacity and taking the network impedance and the operative grid code requirements into consideration.

Chapter 5

Verification of Real-Time Performance and Flicker Mitigation Planning Solutions

5.1 Introduction

In this chapter, the work done on a real-time simulator is described and the details of the implementation are outlined. This chapter serves two main purposes: 1) the utilization of a real-time simulator as a performance testing environment to verify the results obtained from the offline simulations (power system simulation package simulations) in Chapter 3 and Chapter 4; and 2) investigation of planning solutions that a distribution network operator can opt for to alleviate the flicker impacts of a wind farm. The main objective with respect to results verification is to verify that the system behavior and controllers effectiveness are preserved in real-time when the simulations are conducted at a smaller time step and synchronized with a real-time clock. While with respect to flicker mitigation planning solutions, the superior computational capabilities of the real-time environment are utilized to conduct numerous computationally-exhaustive flicker mitigation planning solutions in a time-efficient manner. The proposed planning solutions include tightening of the bandwidth of direct voltage control stipulated by the network operator and implemented by the distributed wind farm, MV/HV substation transformer increased rating, series line compensation and finally, the change of the wind farm connection point.

A parametric study of the effect of wind speed conditions on a wind farm flicker emission was also conducted on the real-time simulator for illustration and completeness purposes, the results are demonstrated in Appendix I.

5.2 Real-Time Simulation Models

In order to both verify the results of Chapter 3 and Chapter 4 as well as test the flicker mitigation planning solutions, two wind farm integration scenarios to the detailed distribution network were under investigation (6 MW and 10 MW wind farms). The decision was to employ one generation scenario of a farm connection to the detailed 25 kV distribution network and apply all investigated flicker mitigation approaches and compare the results with those obtained from the offline simulations. The case of 3 WGs was used as the simulation scenario. Similarly, the case of 5 WGs was chosen for investigation of flicker planning solutions as well as for carrying out the parametric studies demonstrated in Appendix I.

The developed real-time models had to be adapted for real-time simulations as the rules of RT-LAB (real-time digital simulation software) necessitate. RT-LAB is the software that loads the simulation models prepared offline on the simulator processors. To do so, RT-LAB requires the power system to be segregated in a number of subsystems, each standing for a grouping of a number of control blocks and power system elements. The rules for segregation necessitate the following:

1. The model has to have only one master subsystem and could have several slave subsystems.

2. The number of power system elements that can be processed in one subsystem governs the segregation of the model into a number of subsystems to encompass all elements.

3. The subsystems (master and slaves) need to communicate through the RT-LAB communication rules for model separation, these include:

    - use of distributed parameter lines to connect power system elements separated in two subsystems
    - use of delays or sample and hold blocks to process control signals relayed from one subsystem to another

4. Each subsystem is simulated on a dedicated processor on the real-time simulator (OPAL-RT Techologies simulator)

Given the above mentioned rules, model segregation into subsystems was conducted with the utmost purpose of resulting in the least possible alteration to the original offline power system model. It was however imperative to have a slightly altered distribution network and test system after the segregation process due to both the insertion of distributed parameter lines and the delay communications signals. The implemented system according to the above mentioned rules and bearing in mind the available number of processors was constructed as follows:

1. Distribution network: 2 subsystems (The master subsystem and a slave subsystem).

2. WGs: 2 slave subsystems.

3. WGs reactive power controls: 1 slave subsystem.

4. ESS control and management algorithm (DC/DC converter side): 1 slave subsystem

5. Online flickermeters were placed at the buses of interest in the distribution network subsystems.

The implementation as conducted in the RT-LAB environment is shown in Figure 5.1 and Figure 5.2.

5.3 Real-Time Simulations Results of Chapter 3 and Chapter 4 Control Schemes

In the context of real-time performance, the following has been conducted and verified on the real-time simulator:

1. A comparison of all reactive power flicker mitigation approaches (voltage control, leading power factor and variable power factor) on a wind farm scale.

2. The short-term ESS operation, control and management algorithms.

3. On-line real-time flicker measurement and voltage signal processing.

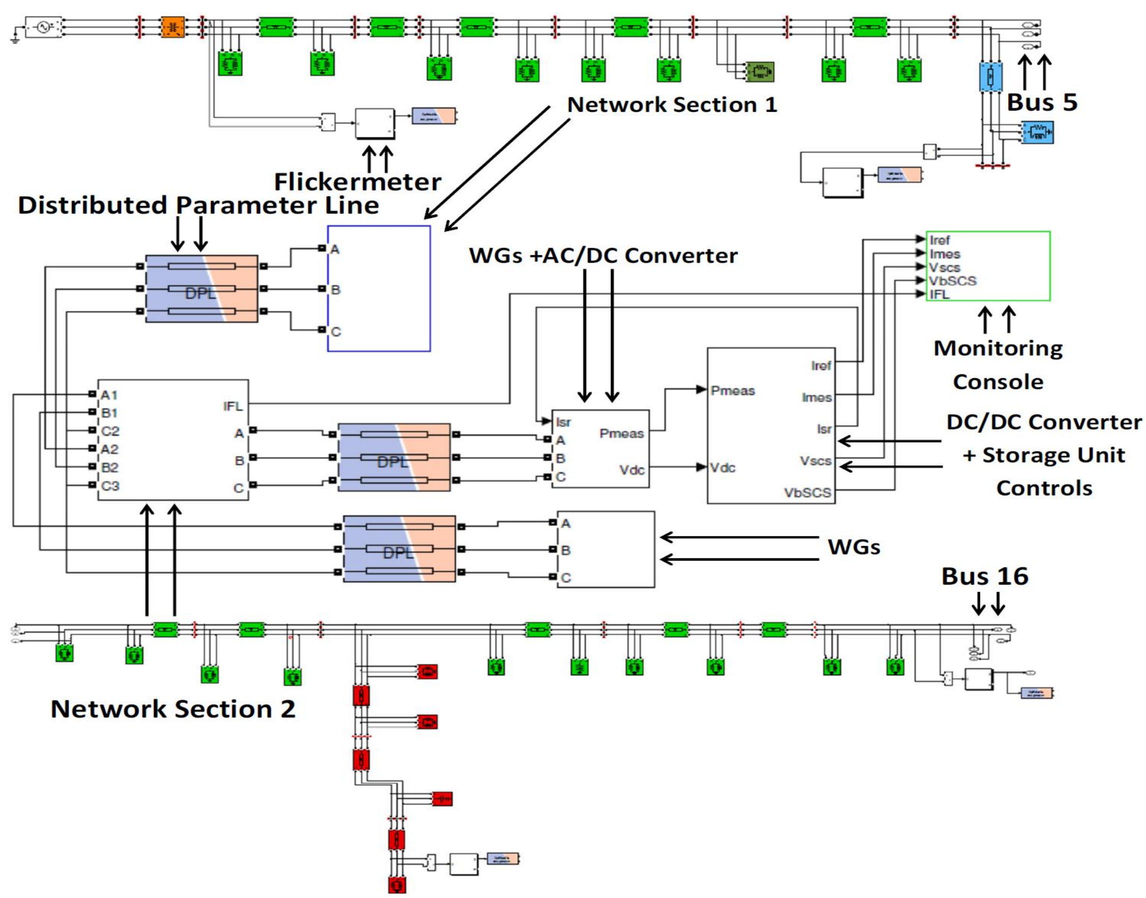

Figure 5.1: Wind farm distribution network segregation in RT-LAB (ESS case).

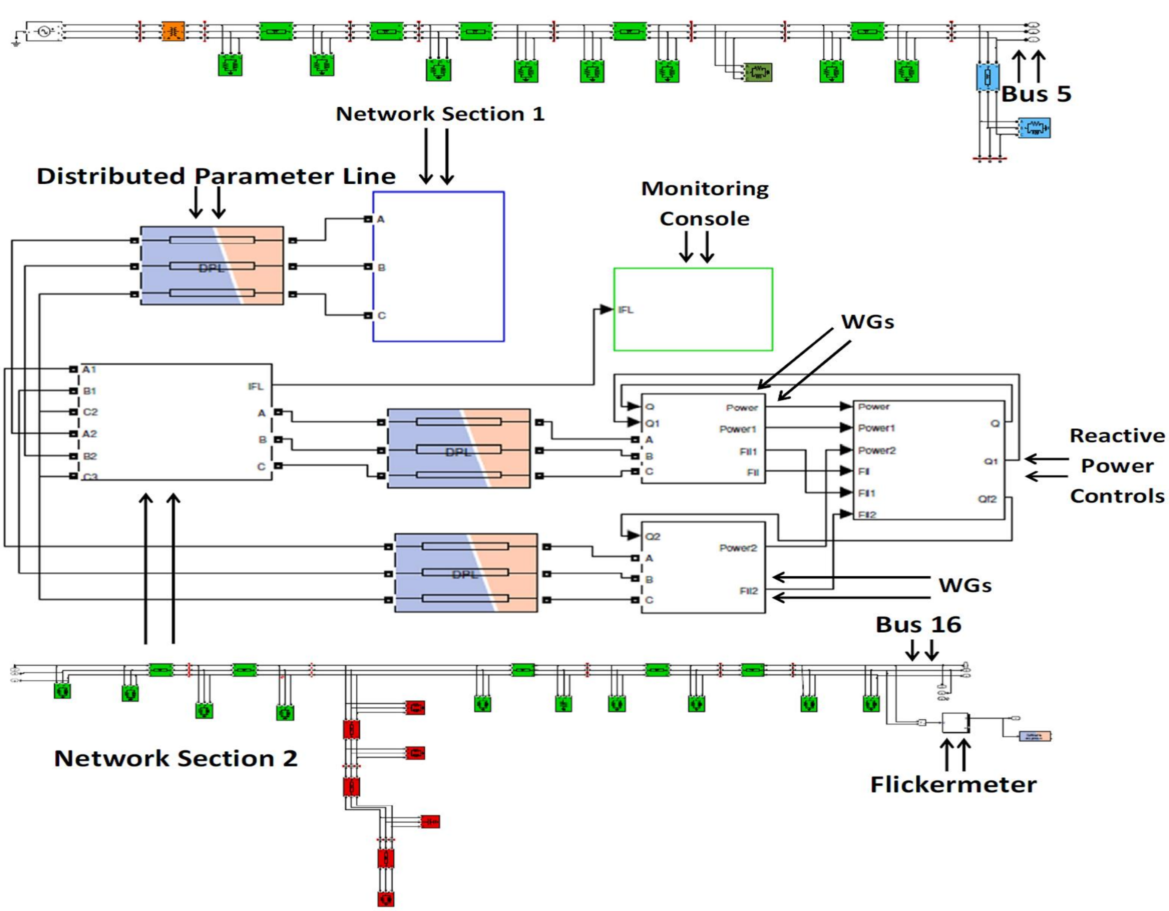

Figure 5.2: Wind farm distribution network segregation in RT-LAB (Reactive power control cases).

The obtained results will be the corresponding results to the enclosed points in Figure 5.3 (presented in Chapter 4) in reference to the network of Figure 2.4.

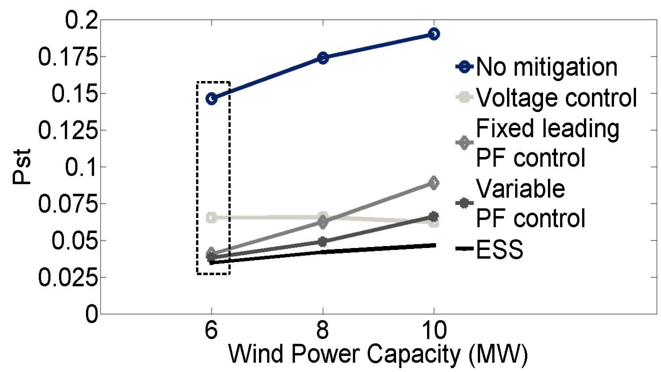

Figure 5.3: Sample Pst values and cases for real-time simulations.

5.3.1 Real-Time Simulations Results of Investigated Mitigation Approaches

The flicker measurement results for the verified cases by the real-time model are shown in Figure 5.4. By investigating Figure 5.4, the same trend of results is seen to be obtained from the real-time simulation model except that the base flicker severity without flicker mitigation is slightly lower than that obtained from the offline simulations (0.121 from the real-time simulation model and 0.146 from the offline simulation for the base case), and similarly for the mitigation approaches (for instance 0.028 for the ESS from the real-time simulation model and 0.0347 from the offline simulation). This can be attributed to an inevitable variation in the network structure introduced by distributed parameter lines whose presence was dictated by the rules of the real-time simulation to separate the subsystems whose number was in turn dictated by the imposed limits on the number of network elements simulated on one processor core.

The flicker mitigation capacity of both the reactive power control approaches as well as the ESS is seen to be preserved in real time. The ESS is shown to provide the highest flicker mitigation capacity.

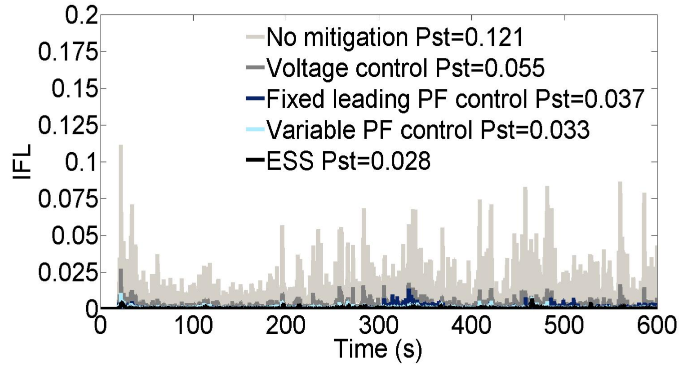

Figure 5.4: IFL and Pst (real-time simulations, 6 MW scenario).

5.3.2 Real-Time Simulations Results of the ESS Control Algorithm

The ESS control performance was observed by recording the ESS active power components as well as the tracking error fed to the power controller. Similarly, the current measurements were performed in the supercapacitor branch as well as one phase of the VSC, the results are shown in Figure 5.5.

In Figure 5.5 (a), the flicker power command, the discharge power command and the measured storage power are shown. The tracking error to the power controller is shown in in Figure 5.5 (b). The impact of the storage control algorithm on the current withdrawn by the ESS is demonstrated by the short-term plots of the ESS VSC phase current and the supercapacitor unit current in Figure 5.5 (c) and Figure 5.5 (d) respectively.

5.3.3 Real-Time Simulations Results of the Network Flicker Profile with the ESS

The impact of the ESS on the network flicker profile is demonstrated by conducting flicker measurements starting at the wind farm connection bus (Bus 16) and going further upstream to the MV/HV transformer (Bus 1). The ESS impact on alleviating the flicker severity across the distribution network is show in Figure 5.6. The impact of the ESS is more conspicuously seen at buses closest to the WGs connection bus reducing flicker severity by as high as 77 % at Bus 16 and as low as 68 % at Bus 1.

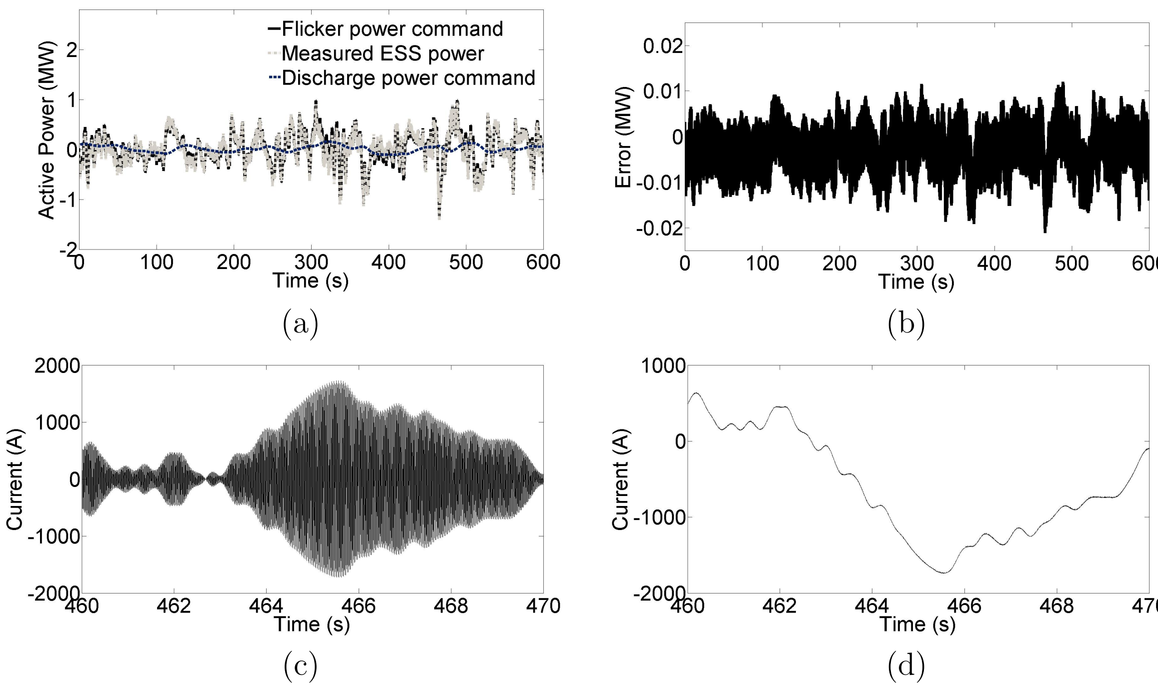

Figure 5.5: ESS control real-time performance (6 MW rating scenario): a) storage power commands and measurement, b) storage power tracking error, c) short-term ESS VSC phase current, d) short-term supercapacitor current.

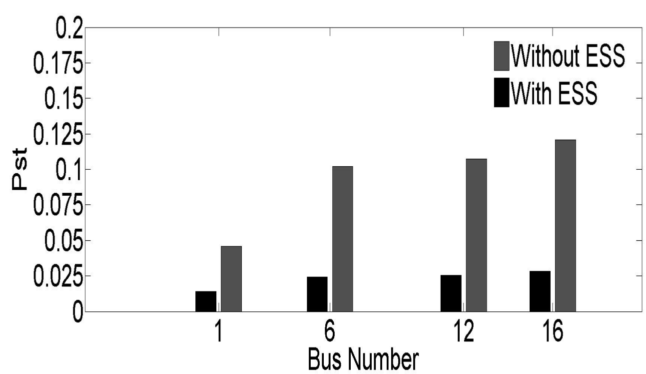

Figure 5.6: Network flicker profile with the ESS (real-time simulation, 6 MW rating scenario).

5.4 Mitigation Planning solutions

5.4.1 Stipulated Bandwidth of the WG Voltage Controller

The conventional voltage control scheme is by droop characteristics, the methodology is based on predefining a characteristic curve that assigns the reactive power setpoint of the WG in response to voltage measurement at the control point (point of connection in this work as described in Chapter 3), (3.14). The range of permissible voltage changes determines the value of the droop gain, the impact of that gain on flicker severity of a wind farm was investigated by testing for four possible ranges of allowed voltage changes assumed in the industry, namely: ± 5 %, ± 6 %, ± 8 % and ± 10 % of V_r, Figure 5.7. The droop gains for the specified voltage bands and an assumed maximum reactive power consumption of 0.48 pu (equivalent to that at a maximum power factor of 0.9) are (9.6, 8, 6 and 4.8) respectively. The sensitivity of the flicker results to the droop gain changes are shown in Figure 5.8.

As can be seen from Figure 5.8, as the bandwidth of allowed voltage changes is tightened, the flicker mitigation capacity of the voltage control approach is increased. Flicker severity (Pst) decreased from 0.17 to 0.079 (46 % of original values) for a ± 10 % voltage control band while it decreased to 0.055 (32 % of original values) for a ± 5 % voltage control band.

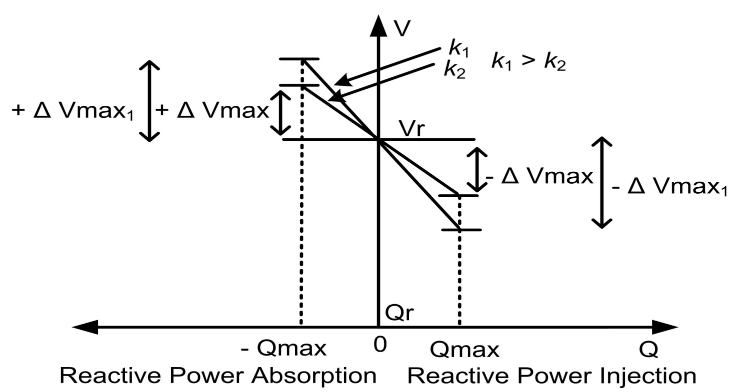

Figure 5.7: Voltage control droop curve for different permissible bandwidths of voltage changes.

The steady decrease in flicker severity by the increase of the droop gains shows that an appropriate solution to provide the sought flicker mitigation, if voltage control as stip-

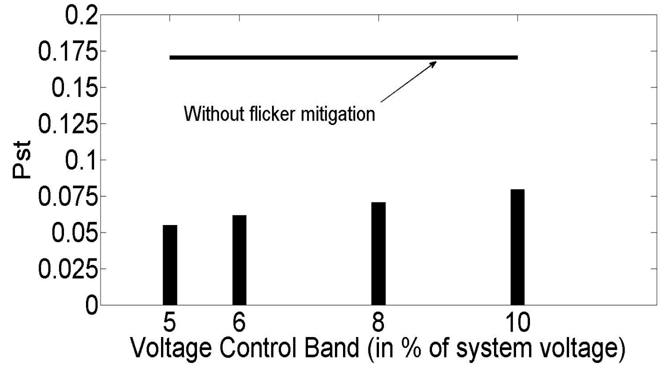

Figure 5.8: Pst vs. the bandwidth of the wind farm voltage controller.

ulated in the grid code falls short of doing so, is to tighten the voltage control bandwidth within its stability limits. Nevertheless, this choice will be associated with an increase in the wind farm consumption of reactive power.

5.4.2 MV/HV Transformer Size Increase

A planning approach that a distribution network operator can consider is the upgrading of its assets in the form of increased rating of the MV/HV substation transformer. This decision results in decreased network impedance (Z_l) and will hence increase the short-circuit level (MVA_{sc}) at the point of connection ($MVA_{sc} = \frac{V^2}{Z_l}$) where V is the system voltage. The MV/HV transformer MVA rating was increased from 15 MVA to 30 MVA to 45 MVA and flicker severity was measured for each case across the network buses. The short-circuit level seen at the point of connection changed from 30 MVA for a MV/HV transformer of 15 MVA to 38 MVA for a MV/HV transformer of 45 MVA for the given network. The Pst values across the network buses are shown for all cases in Figure 5.9. It can be seen from Figure 5.9 that the flicker severity decreased at all buses by increase of the MV/HV transformer MVA rating, decreasing at the point of connection from 0.17 for a MV/HV transformer size of 15 MVA to 0.147 for a MV/HV transformer of 30 MVA to 0.139 for a MV/HV transformer size of 45 MVA. The corresponding Pst values at other network buses decreased in a similar fashion. By considering the percentage decrease in the Pst values, it is seen that only a decrease of 18 % is observed for an increase of 200 % in the MV/HV transformer size.

This approach leads to decreased flicker severity, yet, the achieved flicker mitigation

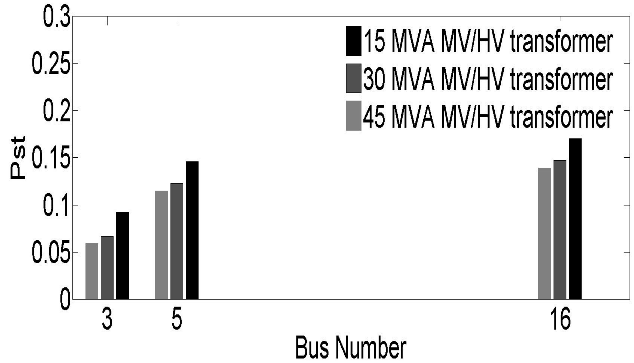

Figure 5.9: Pst values across the network buses for different MV/HV transformer MVA ratings.

does not seem to provide a justification for the incurred costs of upgrading the MV/HV transformer. A MV/HV transformer-based solution that results in decreased system impedance without extra costs could be the use of two existing MV/HV transformers in parallel as described below.

5.4.3 Two MV/HV Transformers in Parallel

MV/HV substations are usually equipped with two identical MV/HV transformers as shown in Figure 5.10 of which only one transformer is in operation and the other is standby for increased system reliability. It is therefore possible to have the two transformers operate in parallel in order to reduce the equivalent impedance of the substation and consequently increase the short-circuit level at the point of connection. The Pst values across the network buses are shown for such operation in Figure 5.11.

The Pst values are seen to be exactly those obtained from the case of increasing the size of the main MV/HV transformer from 15 MVA to 30 MVA seen in Figure 5.9. This equal impact is attributed to the equal impact this approach has on the transformer impedance and hence on the short-circuit level at the point of connection. This approach seems to be a more feasible approach than doubling the size of one MV/HV transformer and can be implemented at no additional cost, yet does not provide significant flicker mitigation when compared to the control options presented in Chapter 3 and Chapter 4.

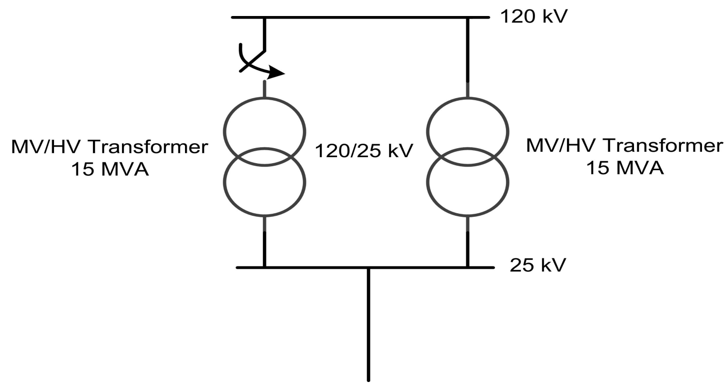

Figure 5.10: Typical MV/HV substation transformers configuration.

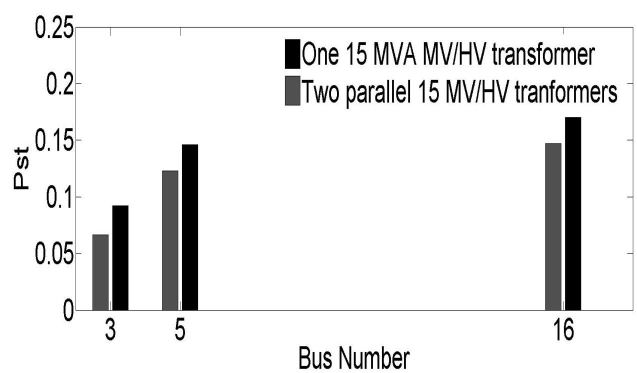

Figure 5.11: Pst values across the network buses for two identical MV/HV substation transformers of 15 MVA operating in parallel.

5.4.4 Distribution Feeder Series Compensation

Distribution feeder compensation is another planning option that a distribution network operator can opt for. Distribution feeder compensation is common in distribution networks and is occasionally resorted to for voltage compensation purposes [70]. The conventional approach is by series compensation of the feeder, the value of the added impedance varies considerably in literature [71]. Conventional compensation of feeders is done by a series capacitor, but this is under the conventional unidirectional flow of power from the grid to the loads in absence of DG and the presence of a low voltage level at the end of the feeder [72]. In case of DG and especially as the the network X/R ratio decreases, the voltage drop over the feeder is already compensated by the reverse feed of power from the DG units. In that case, a series reactance can be of interest to increase the network X/R ratio and hence decrease the flicker severity as well as improve the feeder voltage profile by avoiding voltage rise problems. The values of the series reactors investigated were 25 %, 50 % and a 100 % series compensation (of line reactance). The Pst values are shown in Figure 5.12. The Pst value is shown to decrease to 0.118 (69 % of its original value) for 50 % series reactive compensation of the network (placed at the point of connection) and further increases beyond that as the reactance increases to a 100 % reactive compensation. Based on Figure 5.12, this approach needs to be seen taking into consideration the two opposing impacts of short-circuit level at the point of connection and network X/R ratio on flicker severity (flicker severity will increase by increase of system impedance and will decrease by increase of the network X/R ratio). A properly calculated compensation ratio serves to mitigate the flicker severity as well as the voltage rise problem.

5.4.5 Change of Connection Point

It is possible that a network operator also resorts to a change of the connection point. The 10 MW wind farm connection point was changed by moving across the distribution network from the weakest point (Bus 16) up to the MV/HV substation (increasing network strength). The three connection points were Bus 16, Bus 5 and Bus 3 and with short-circuit levels of 30 MVA, 40 MVA and 65 MVA. The Pst values across the network buses are shown for all cases in Figure 5.13. It is clear from Figure 5.13 that considerable decrease in wind farm flicker emission at the point of connection can be achieved by connection to a stronger grid point. Nevertheless, it is shown that the flicker severity

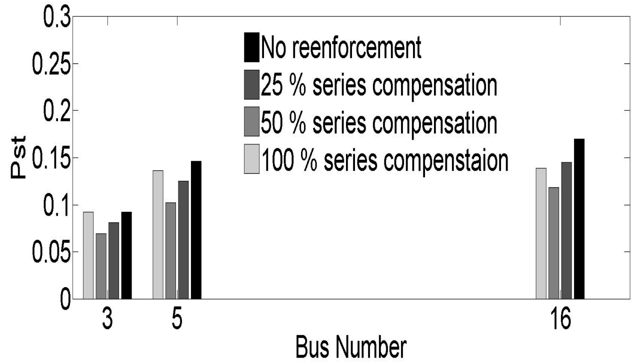

Figure 5.12: Pst values across the network buses for different levels of series reactive compensation.

at certain buses (Bus 5 for instance) might not be affected by the change of connection point (from Bus 16 to Bus 5 in that case). In the first case (connection at Bus 16), the flicker severity at Bus 5 is governed by the flicker attenuation factor between Bus 16 and Bus 5 [73, 74, 75], while in the second case (connection at Bus 5), it is governed by the network strength at Bus 5.

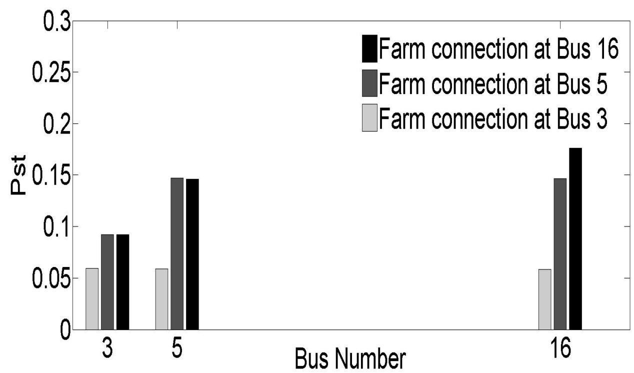

Figure 5.13: Pst values across the network buses for different connection points.

In reality, several flicker sources will exist at the different network buses and the ultimate goal is to make sure the collective flicker severity (from all sources at all the network buses) abides by the global flicker limits of the distribution level [73] and hence the change of the connection point will have to be seen from that perspective. For instance, if Bus 5 already has a flicker source connected, Bus 16 (a weaker and worse point of connection for wind power) can be a more appropriate point of connection as seen from a global network perspective (flicker transfer coefficients will attenuate the impact on other network buses). Accordingly, this approach needs to be contemplated taking into consideration the buses of interest at which flicker severity is desired to be mitigated and whether other flicker sources are connected to those buses and how the global flicker levels are affected.

5.5 Conclusion

In this chapter, the real-time performance of the proposed flicker mitigation schemes in this thesis was investigated. The trend of results obtained from the real-time model was coherent with those obtained from the power system offline simulations except for minor discrepancies in the absolute flicker values attributed to an inevitable alteration to the test distribution network structure. The proposed active and reactive power control algorithms demonstrated real-time functionality and highly alleviated flicker severity. Mitigation planning solutions were also investigated, the different presented planning solutions were shown to have varying flicker mitigation capacities and can be considered for implementation based on the cost of implementation, the stipulations of the operative grid code and the flexibility of the wind farm placement site.

Chapter 6

Conclusions and Future Work

6.1 Summary

The work of this thesis researched the flicker emission of wind power integrated to distribution networks and proposed solutions to overcome the problem and allow for higher capacity integration of wind power at the distribution level. Voltage flicker was assessed in accordance with accepted IEC and IEEE standards. With the work being dedicated to distribution networks, the work of this thesis considered a wide spectrum of connection points characteristics typical of distribution networks and quantified the flicker emission in terms of flickermeter-produced flicker indices. In order to cover such a wide range of connection points (characterized by their short-circuit level and X/R ratio), both simplified and detailed representations of distribution networks were utilized in the conducted studies. The work thoroughly studied and identified the anticipated impact of WGs reactive power control variants on flicker severity. In terms of grid-code compliance and flicker mitigation solutions, a modified reactive power control scheme, an energy storage control algorithm and wind farm integration planning solutions were proposed with the ultimate purpose being the accommodation of increased penetration of wind power in distribution networks. The proposed solutions and supporting analyses are anticipated to help serve that purpose and are applicable to other intermittent-resource DG units. In order to verify the applicability of the proposed solutions to real-life scenarios, different sizes of distributed wind farms were considered and the proposed control schemes were tested on a real-time simulator.

6.2 Conclusions

The work of this thesis was motivated by the voltage flicker problem encountered by utilities upon the integration of WGs to their distribution networks and therefore the conclusions of this body of work are viewed from that perspective and are broken down by subject with respect to the visited research areas. The conclusions are summarized in bullet points in the following subsections.

6.2.1 Impact of Reactive Power Control on Flicker Emission

- Voltage control and fixed leading power factor control can be identified as straightforward flicker mitigation schemes, the feasibility of which and hence the preference of one over the other is connection-point, wind-farm-size and utility-regulation dependent.

- Under conventional power factor control, flicker severity reaches a minimum value at a reactive power compensation value of approximately $Q = -PR/X$, beyond which, and contrary to the behavior of the steady-state voltage level, higher flicker values are observed. This is due to overcompensated voltage changes and the resulting negative voltage fluctuations rather than nullified changes. In that regard, the steady-state voltage rise and voltage flicker are not necessarily simultaneously alleviated by fixed leading power factor operation of the WGs.

- It is possible to achieve flicker mitigation under all the possible reactive power requirements on the WG (injection, absorption or no requirement), if the flicker-producing changes in active power are dealt with irrespective of the nonflicker-producing changes (compensated at a different reactive power ratio of the active power magnitude of change). This can be achieved by filtering schemes and proper control gains representing the network X/R ratio and the desired reactive behavior of the WG.

6.2.2 Impact of an ESS on Flicker Emission

- An ESS sized based on short-term wind speed average and turbulence intensity at the installation site provides a reasonable power sizing approach for flicker mitigation purposes.

- A short-term ESS has a superior impact on flicker mitigation when compared to any reactive power control approach. This is attributed to the direct flicker mitigation, achieved by elimination of the entire flicker content, in the WGs output, from the active power injected into the distribution network.

- Flicker mitigation approaches based on power factor control exhibit varying flicker mitigation abilities as the size of a wind farm changes. This is attributed to the fact that those methods are open-loop methods that assume an approximation of the voltage changes equation over the distribution network. The approximation assumes negligible voltage angle difference between the wind farm integration bus and a constant-voltage receiving-end bus. As that angle increases, those methods exhibit a decreasing flicker mitigation ability.

- The feedback feature of the voltage control approach and the independence of the ESS approach of the line parameters render those two methods less dependent on the size of the wind farm and the characteristics of the grid connection point.

6.2.3 Real-Time Simulations

- Real-time simulations provide an efficient way of conducting lengthy simulations of power system models with a large number of power system and control elements. Those simulations are very computationally exhaustive and time-consuming in power system simulation packages. The models simulated on a real-time simulator also benefit from the ability to run simulations at smaller time steps and therefore higher accuracy than those simulated offline.

- As the number of power system elements increases, inevitable alterations to the original models are necessary due to limitations on the number of elements simulated in one subsystem of the adapted models.

- Control signals should be taken into consideration before embarking on the model separation process, those signals should not be transmitted between separate subsystems as time delays are necessary and the control action is somehow altered.

6.2.4 Wind Farm Planning Solutions

- Wind farm planning solutions can be utilized to reduce the expected flicker emission of a wind farm. Typically, this would depend on the distribution network operator flexibility with the binding grid code, the economic feasibility of network upgrading schemes and the other purposes served by the networking upgrading schemes (possibly voltage rise mitigation).

6.3 Recommendations for Future Work

The work of this thesis proposed solutions to alleviate the flicker emission severity of distributed wind power. The solutions were viewed from an operational perspective based on the level of flicker severity attenuation. The following point is thought of as a sound continuation of this work:

- Financial assessment of the cost of implementation, especially in terms of ESS deployment and network upgrading solutions. This will provide wind farm planners with both a technical and an economical assessment of a potential flicker mitigation solution.

The voltage flicker problem was also viewed in this work from a supplementary-control perspective, in the sense that control strategies were conceived to facilitate the integration process of WGs to distribution networks. The same problem could be viewed from a completely different perspective, in which case, the following point could provide a fruitful research area:

- Optimal wind farm layout, given the stochastic nature of wind speed profiles, aiming for the maximal smoothing of net active power production and hence smoothed active power injections into distribution networks and alleviated voltage fluctuations.

The quantification of the flicker impact in this work was made through the utilization of the standard IEC flickermeter. The flickermeter measurements are based on the eye-brain response to light flickering induced in incandescent lamps. This being said, that sort of flicker metrology is best suited for incandescent lamps but is not suitable for quantifying flicker induced in other sorts of lamps and evoked by interharmonic components. In that regard, the following points could be promising points of research:

- Modifications to the current flickermeter to accommodate the capability of quantifying flicker induced in other sorts of lamps.
- Research of flicker compatibility and planning levels and whether they should be relaxed with the recent restrictions on the use of incandescent lamps imposed and planned in several countries.

Appendix A

Wind Speed Data

The raw wind data time-series employed in this work were selected based on weibull distribution fitting [76] and is the same as that used previously in the works of [77, 78]. The wind data were scaled to have different means and the standard deviation of the data set was varied to control the turbulence intensity of the wind profile, making it suitable for use in the conducted parametric studies presented in Appendix I. The weibull fitting as well as the cumulative distribution function for the used wind data at a wind speed average of 10 m/s are shown in Figure A.1.

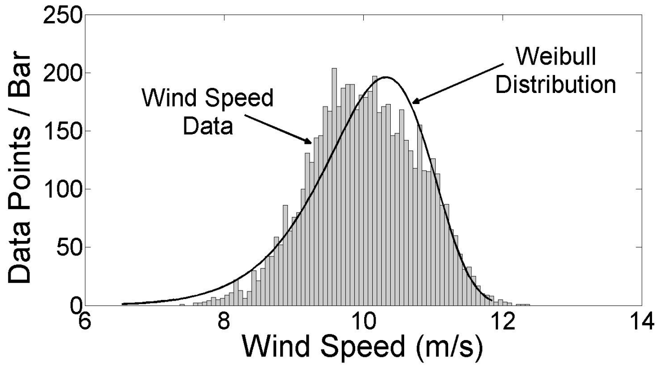

(a)

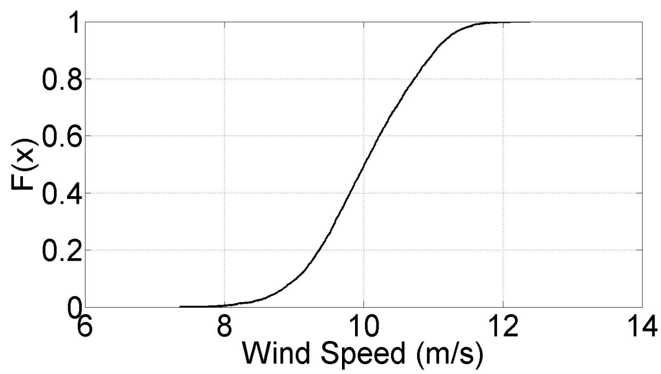

(b)

Figure A.1: Weibull-distributed 10-minute wind speed profile: a) weibull distribution fitting, b) cumulative distribution function.

Appendix B

Tower Shadow and Wind Shear Mathematical Model

To accurately represent the dynamics of the wind turbine and the impact on the generated active power profile, the wind speed data used in the simulations constituted of three components (B.1). The first of the three components V_H was a 10-minute window of raw wind speed data sampled at 0.1 s and amounting to 6000 data points. This component was mathematically modified to include the impact of the cyclic tower shadow V_{ts} and wind shear V_{ws} effects. The mathematical model used for the torque shadow component was of the form of (B.2) and the wind shear component of the form of (B.3) as proposed in [41],

$$V_{eq} = V_H + V_{ts} + V_{ws} \tag{B.1}$$

$$V_{ts} = \frac{(1 + \frac{\alpha(\alpha-1)r^2}{8H^2})V_H}{3r^2} \sum_{n=1}^{3} (\frac{a^2}{\sin^2\theta_n} ln(\frac{r^2\sin^2\theta_n}{x^2} + 1) - \frac{2a^2r^2}{r^2\sin^2\theta_n + x^2}) \tag{B.2}$$

$$V_{ws} = V_H(\frac{\alpha(\alpha-1)r^2}{8H^2} + \frac{\alpha(\alpha-1)(\alpha-2)r^3}{60H^3}\cos 3\theta) \tag{B.3}$$

where α is the wind shear exponent, H is the hub height, r is the rotor blade radius, a is the tower radius, θ_n is the angle of the blade and x is the distance from the blade origin to the tower midline. A three-bladed wind turbine was assumed and one angle θ_1 was obtained from the integral of the meaured turbine rotational speed and the two other angles calculated by shifts of $2\frac{\pi}{3}$ and $4\frac{\pi}{3}$ respectively. The used parameters in the mathematical model are shown in Table. B.1.

Table B.1: Assumed Wind Turbine Parameters

Parameter	Value	unit
Hub height H	90	m
Rotor radius r	40	m
Tower radius a	2	m
Distance from blade origing to tower midline x	3	m
Wind shear exponent α	0.3	–

Appendix C

Sample Results on the Full-Converter Synchronous Generator

The WG model used to obtain the results documented in this thesis was of the DFIG type, sample tests were conducted using a full-converter synchronous WG of the same size (2 MW) as described in Appendix D. The aim was to demonstrate that similar flicker mitigation behavior is anticipated under the proposed controls. Figure C.1 shows the generator operation under both unity power factor control and variable power factor control centered around zero reactive power consumption for two sample cases. It is clear that similar trends as those obtained in Sec.3.6 for the DFIG are obtained. Similarly, the impact of the use of the ESS proposed in Chapter 4 is demonstrated in Figure C.2 for the power system parameters described in Sec.4.5.1. The ESS proves its effectiveness in case of the full-converter synchronous WG as it did for the DFIG topology. This shows that the proposed flicker mitigation controls are expected to work in a similar fashion for both two types of WG topologies.

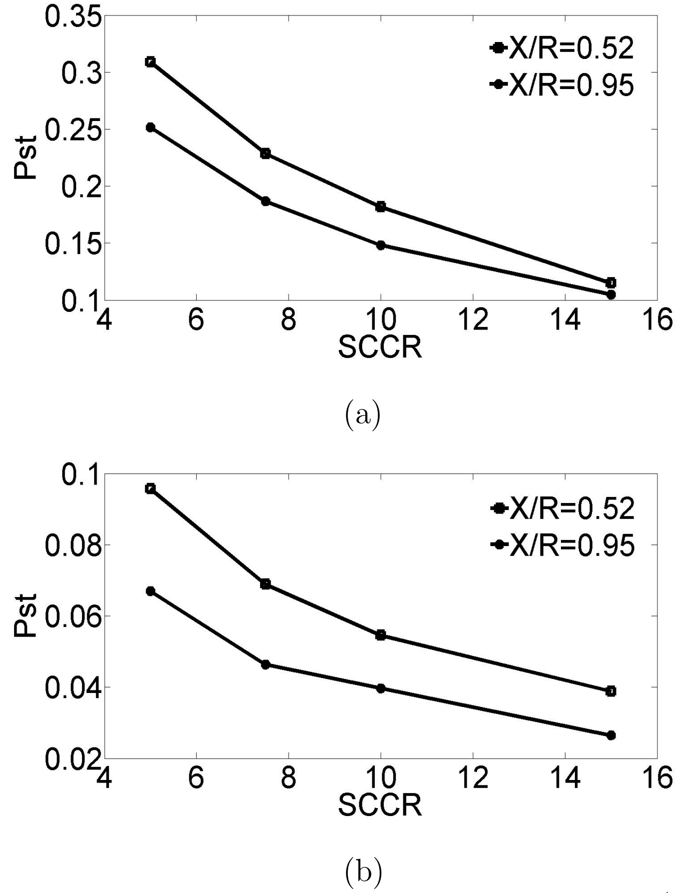

Figure C.1: Pst vs. SCCR, full-converter synchronous generator :(a) unity power factor, (b) decoupled reactive power control.

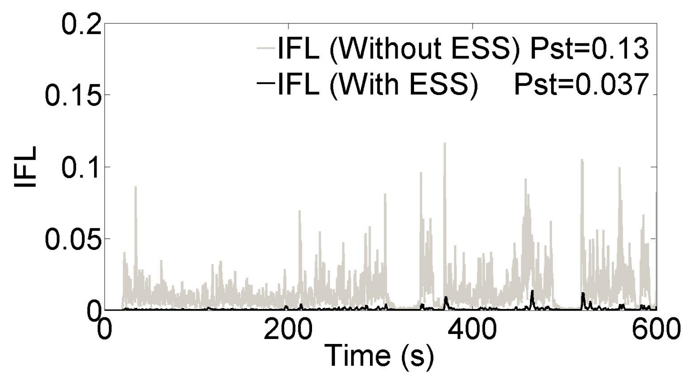

Figure C.2: Flicker measurement at the PCC with and without the ESS, full-converter synchronous generator.

Appendix D

Electric Generator Control

D.0.1 DFIG

The DFIG consists of an induction machine to which connection is made to the rotor windings through the Rotor-Side (RS) converter. The Grid-Side (GS) converter connects the stator to a DC-link that is connected on the other side to the RS converter. By controlling the currents in the rotor, the machine speed can be adjusted to achieve the MPPT operation. The machine model used employs conventional two-coordinate decoupled dq control. Under such control, the control of reactive power becomes independent of the machine MPPT algorithm, and therefore, the reactive power can be controlled independently by the quadrature-axis currents of both converters.

The GS converter control aims at maintaining a constant DC link voltage. The machine stator and rotor voltage and current quantities V_s, I_s and V_r, I_r respectively are measured to estimate the active power output of the machine P_{ref} and the machine speed ω_{ref} is set accordingly based on the adopted $P-\omega$ characteristics. The error between the desired speed ω_{ref} and the machine rotational speed ω_{rot} is used to set the reference direct-axis current for the RS control. The GS direct-axis current is set in a similar manner but based on the deviation of the DC link voltage V_{dcmes} from the desired reference V_{dcref}. The quadrature-axis current reference of both controls is set based on the adopted Q control scheme. Figure D.1 shows a schematic of the complete machine model in use.

The GS converter is a voltage source converter (VSC) whose primary control task is to maintain its DC link voltage constant. Considering Figure D.2, (D.1) describes the relation between the voltage at the PCC and the voltages at the converter terminals, where R_{gs} and L_{gs} are the values of resistance and inductance in the connecting branches.

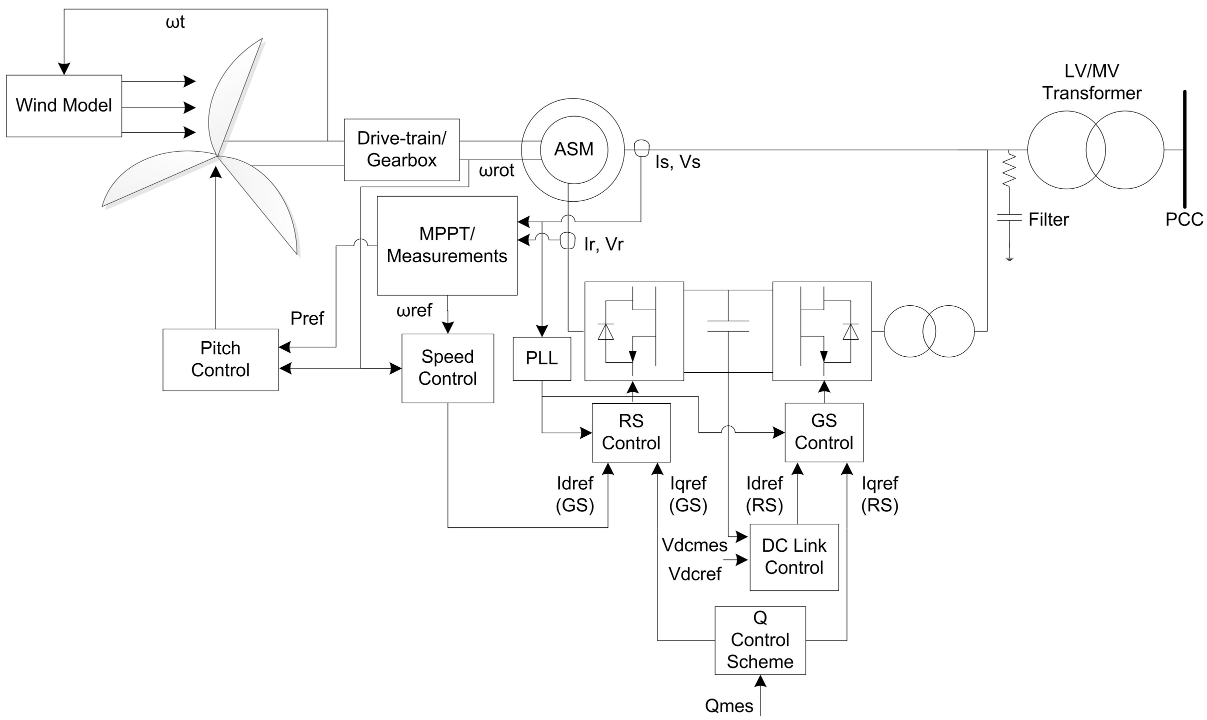

Figure D.1: DFIG control schematic.

$$V_a = R_{gs} i_a + L_{gs} \frac{di_a}{dt} + V_a^{'} \tag{D.1a}$$

$$V_b = R_{gs} i_b + L_{gs} \frac{di_b}{dt} + V_b^{'} \tag{D.1b}$$

$$V_c = R_{gs} i_c + L_{gs} \frac{di_c}{dt} + V_c^{'} \tag{D.1c}$$

By using the conventional Parks transformation, (D.1) can be transformed in two coordinates in the dq frame. The resulting equations in the dq frame are in the form of (D.2).

$$V_d = R_{gs} i_d + L_{gs} \frac{di_d}{dt} + \omega L_{gs} i_q + V_d^{'} \tag{D.2a}$$

$$V_q = R_{gs} i_q + L_{gs} \frac{di_q}{dt} - \omega L_{gs} i_d + V_q^{'} \tag{D.2b}$$

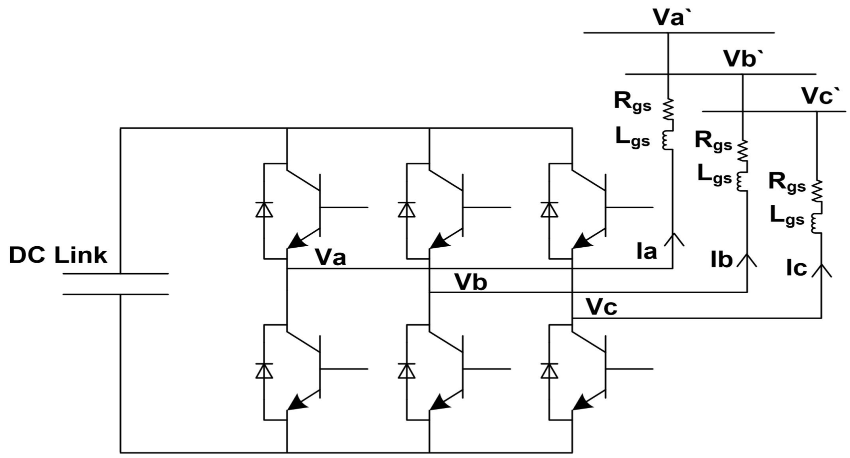

Figure D.2: Voltage source converter.

The angular position required for transformation is found by integrating the system rotational speed as calculated in a phase-locked loop (PLL) processing the system voltage at the point of connection, (D.3). The active and reactive power of the machine delivered through the GS converter expressed in the *dq* frame take the form of (D.4).

$$\theta = \int \omega dt \tag{D.3}$$

$$P = V_d i_d + V_q i_q \tag{D.4a}$$

$$Q = V_q i_d - V_d i_q \tag{D.4b}$$

When the direct-axis component of the rotating frame is aligned with the stator voltage, the resultant voltage quadrature-axis component nullifies and the direct-axis voltage becomes constant. Consequently, the active and reactive power of either the stator or the rotor are controlled independently through the adjustment of the direct-axis and quadrature-axis currents respectively (D.5). Utilizing equations (D.1)-(D.5), the control scheme for the GS converter is realized, Figure D.3.

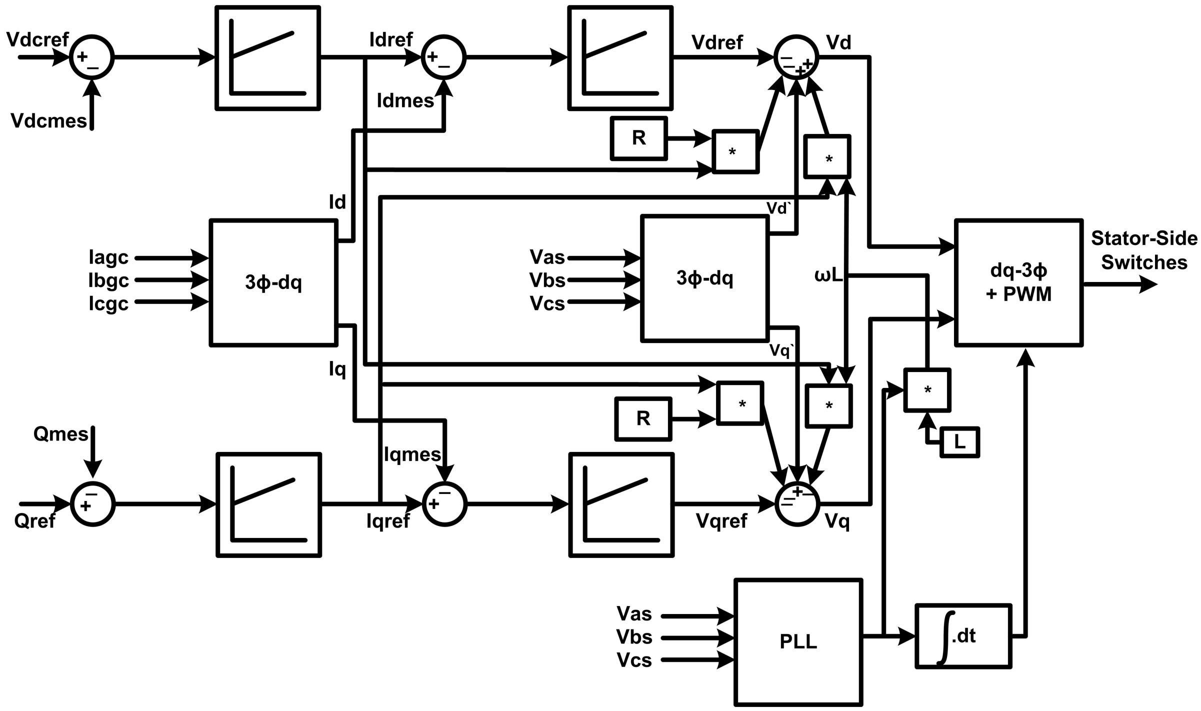

Figure D.3: Grid-side converter control block diagram.

$$P = V_d i_d \tag{D.5a}$$

$$Q = -V_d i_q \tag{D.5b}$$

Similarly, and according to Appendix E and using (E.7), the rotor voltage equations can be used to control the machine speed (active power) and the rotor reactive power. The RS control realization is shown in Figure D.4.

The overall performance of the wind-turbine-generator unit modeled as described in the above sections is demonstrated by the plots of Figure D.5. Figure D.5 features plots of the machine active power generation with and without the 3p torque oscillations, the frequency of the 3p torque oscillations for varying wind speed averages, the active power generation for varying levels of turbulence intensity of the wind speed regime, and machine speed variations for varying levels of turbulence intensity.

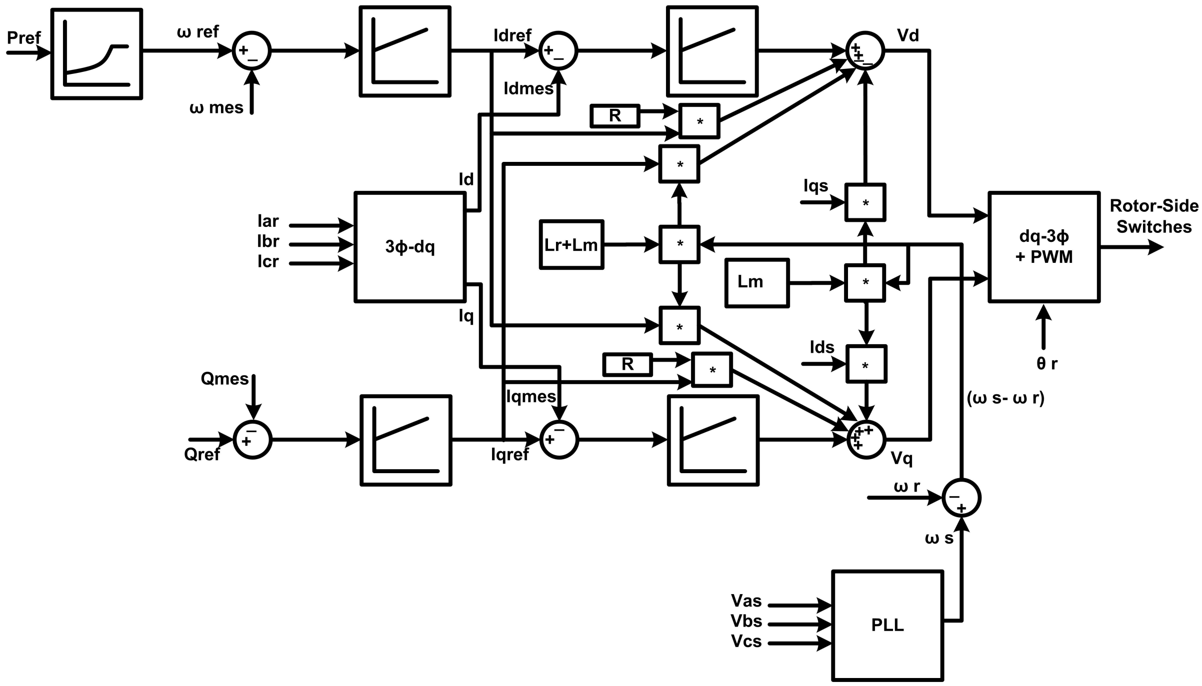

Figure D.4: Rotor-side converter control block diagram.

D.0.2 Full-Converter Synchronous Machine WG

The full-converter synchronous generator topology consists of a synchronous generator and a fully-rated converter through which all the active power generation of the WG is delivered to the grid. The active power is unidirectional in the GS converter from the machine to the grid as opposed to the bidirectional flow in the DFIG. The generic configuration of this WG topology is shown in Figure 2.1 (c). The machine-side converter can also be replaced by a three-phase rectifier bridge and a DC/DC converter as shown in Figure D.6 and as implemented in the model in use in this work. The GS converter is controlled in the same manner as that of the DFIG with the objective of maintaining a fixed DC-link voltage, Figure D.3. The DC output of the rectifier bridge is controlled by a DC/DC converter that feeds the DC-link. Therefore, the output power and the speed of the machine are controlled by control of the machine stator currents by means of the DC/DC converter control. The speed control is applied utilizing speed and current measurements as shown in Figure D.7.

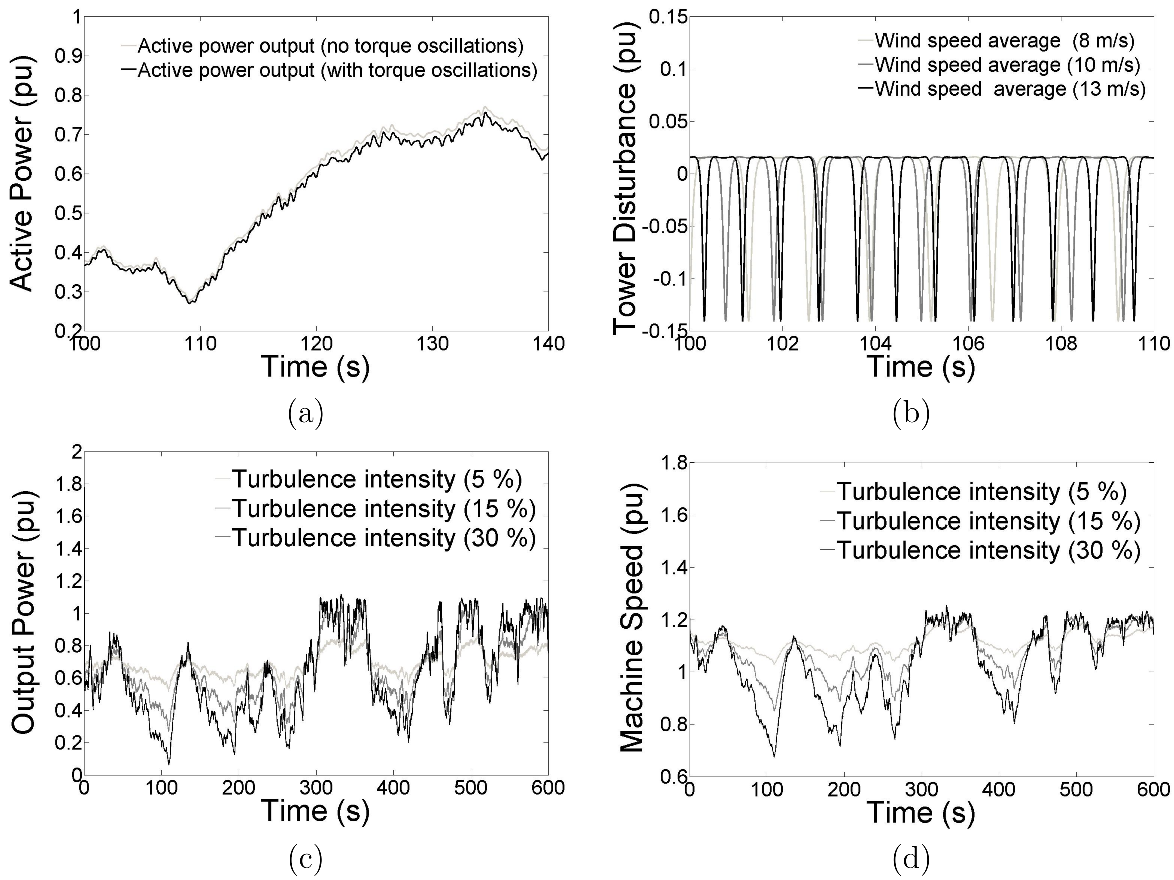

Figure D.5: Overall performance of the DFIG unit: (a) active power generation with and without the 3p torque oscillations (10 m/s), (b) 3p torque oscillations frequency at different wind speeds,(c) active power generation at different levels of turbulence intensity (10 m/s), (d) machine rotational speed at different levels of turbulence intensity (10 m/s).

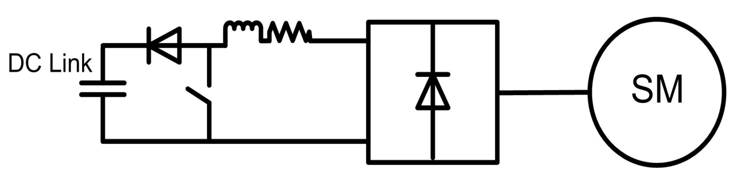

Figure D.6: Machine-side converter, full-converter synchronous generator.

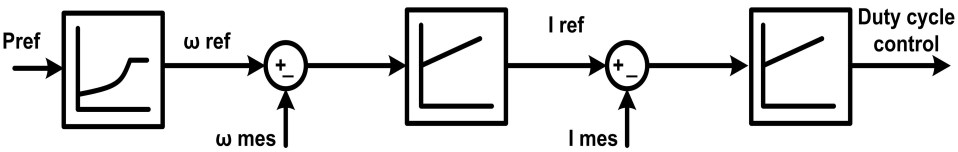

Figure D.7: Machine-side control, full-converter synchronous generator.

Appendix E

DFIG Rotor-Side Converter Control

The DFIG RS converter is responsible for achieving the adherence to the MPPT algorithm and its control is achieved in a decoupled dq frame and based on the induction machine flux equations. The basic flux equations for the induction machine are (E.1) and (E.2).

$$\Lambda_{as} = i_{as}L_{aa} + i_{bs}L_{ab} + i_{cs}L_{ac} \tag{E.1a}$$
$$\Lambda_{bs} = i_{as}L_{ab} + i_{bs}L_{bb} + i_{cs}L_{bc} \tag{E.1b}$$
$$\Lambda_{cs} = i_{as}L_{ac} + i_{bs}L_{bc} + i_{cs}L_{cc} \tag{E.1c}$$

$$\Lambda_{ar} = i_{ar}L_{aa} + i_{br}L_{ab} + i_{cr}L_{ac} \tag{E.2a}$$
$$\Lambda_{br} = i_{ar}L_{ab} + i_{br}L_{bb} + i_{cr}L_{bc} \tag{E.2b}$$
$$\Lambda_{cr} = i_{ar}L_{ac} + i_{br}L_{bc} + i_{cr}L_{cc} \tag{E.2c}$$

For a balanced three-phase system, the sum of the phase currents adds to zero and the equation for each phase after carrying out a number of substitutions can be written in terms of the phase currents in the stator and the rotor as in (E.3);

$$\Lambda_{as} = i_{as}L_s + i_{ar}L_m \tag{E.3}$$

where L_s is the equivalent stator self-inductance and L_m is the mutual inductance between the stator and the rotor. The stator and rotor terminal voltages are written as in (E.4).

$$V_s = R_s i_s + \frac{d\Lambda_s}{dt} \tag{E.4a}$$

$$V_r = R_r i_r + \frac{d\Lambda_r}{dt} \tag{E.4b}$$

By transformation to the *dq* frame and solving in a synchronous frame, (E.5) and (E.6) can be obtained from (E.3) and (E.4) [79].

$$V_{ds} = R_s i_{ds} + \frac{d\Lambda_{ds}}{dt} - \omega_s \Lambda_{qs} \tag{E.5a}$$

$$V_{qs} = R_s i_{qs} + \frac{d\Lambda_{qs}}{dt} + \omega_s \Lambda_{ds} \tag{E.5b}$$

$$V_{dr} = R_r i_{dr} + \frac{d\Lambda_{dr}}{dt} - (\omega_s - \omega_r)\Lambda_{qr} \tag{E.5c}$$

$$V_{qr} = R_r i_{qr} + \frac{d\Lambda_{qr}}{dt} + (\omega_s - \omega_r)\Lambda_{dr} \tag{E.5d}$$

$$\Lambda_{ds} = i_{ds} L_s + i_{dr} L_m \tag{E.6a}$$

$$\Lambda_{qs} = i_{qs} L_s + i_{qr} L_m \tag{E.6b}$$

$$\Lambda_{dr} = i_{dr} L_r + i_{ds} L_m \tag{E.6c}$$

$$\Lambda_{qr} = i_{qr} L_r + i_{qs} L_m \tag{E.6d}$$

Differentiating and substituting (E.6) into (E.5), an expression for the quadrature-axis and direct-axis voltages can be obtained in terms of the quadrature-axis and direct-axis currents (E.7).

$$V_{ds} = R_s i_{ds} + L_s \frac{di_{ds}}{dt} + L_m \frac{di_{dr}}{dt} - \omega_s (L_s i_{qs} + L_m i_{qr}) \tag{E.7a}$$

$$V_{qs} = R_s i_{qs} + L_s \frac{di_{qs}}{dt} + L_m \frac{di_{qr}}{dt} + \omega_s (L_s i_{ds} + L_m i_{dr}) \tag{E.7b}$$

$$V_{dr} = R_r i_{dr} + L_r \frac{di_{dr}}{dt} + L_m \frac{di_{ds}}{dt} - (\omega_s - \omega_r)(L_r i_{qr} + L_m i_{qs}) \tag{E.7c}$$

$$V_{qr} = R_r i_{qr} + L_r \frac{di_{qr}}{dt} + L_m \frac{di_{qs}}{dt} + (\omega_s - \omega_r)(L_r i_{dr} + L_m i_{ds}) \tag{E.7d}$$

Appendix F

IEC Flickermeter Details

The IEC flickermeter is a measuring apparatus that processes a voltage waveform and yields a statistically-calculated index P_{st} that reflects the severity of the flicker content contained in the processed voltage waveform. The apparatus as described by standard IEC 61000-4-15 is a combination of the following two main modules [44]:

1. Simulation of the response of the lamp-eye-brain chain.

2. On-line statistical analysis of the flicker signal and presentation of results.

To achieve those tasks, the flickermeter consists of five main blocks and are classified as follows (with reference to Figure F.1):

1. Calibration and scaling: scales the measured voltage signal to a reference voltage level to be processed by the flickermeter independent of the power system voltage level (Block 1).

2. Squaring Multiplier: recovers voltage fluctuations by squaring the voltage signal simulating the behavior of a lamp (Block 2).

3. Weighting Filters: consists of a cascade of two filtering modules; the first filtering module consists of both a first-order high-pass (F.1) and a sixth-order butterworth low-pass (F.2) filters and eliminates the DC and the double mains frequency components from the processed demodulator output; the second filtering module is a weighting filter that simulates the frequency response of the human visual system to sinusoidal voltage changes in an incandescent lamp. The response function is based

on experimental studies on the perceptibility threshold found at each frequency by 50 % of the tested humans (Block 3).

$$F_1(s) = \frac{\tau_{lp} s}{1 + \tau_{lp}} \tag{F.1}$$

$$F_2(s) = \frac{1}{(\frac{s}{\omega_f})^2 + as + 1} \frac{1}{(\frac{s}{\omega_f})^2 + bs + 1} \frac{1}{(\frac{s}{\omega_f})^2 + cs + 1} \tag{F.2}$$

$$F_3(s) = \frac{k\omega_1 s}{s^2 + 2\lambda s + \omega_1^2} \frac{(1 + \frac{s}{\omega_2})}{(1 + \frac{s}{\omega_3}) + (1 + \frac{s}{\omega_4})} \tag{F.3}$$

The constants involved in the above equations have the values shown in Table F.1.

Table F.1: Flickermeter Filters Constants

Parameter	Value
τ_{lp}	3.1831
ω_f	263.8938
a	1.9614e-3
b	5.358e-3
c	7.32e-3
λ	26.1820
ω_1	57.0325
ω_2	18.4663
ω_3	8.7588
ω_4	108.7934

4. Squaring and Smoothing: consists of a squaring multiplier and a low-pass filter to simulate the nonlinear eye-brain perception (Block 4). The output of this block is the instantaneous flicker level/sensation (IFL).

5. On-line Statistical Analysis: consists of a microprocessor that performs statistical

analysis on the IFL data and translates it into flicker indices. The purpose of this block is to separate the measured IFL points (sampled at a predetermined frequency) into a number of classes for the processed time frame thus indicating the percentage time the IFL fell into each of the designated classes. The formula of (F.4) applies for the calculation of the short-term flicker index P_{st}.

$$P_{st} = \sqrt{0.0314P_{0.1} + 0.0525P_{1s} + 0.0657P_{3s} + 0.28P_{10s} + 0.08P_{50s}} \qquad \text{(F.4)}$$

where $P_{0.1}$, P_{1s}, P_{3s}, P_{10s} and P_{50s} are the flicker levels being exceeded for 0.1 %, 1 %, 3 %, 10 % and 50 % of the time. The subscript s stands for probability percentiles that should be obtained from smoothing formulae and further percentage calculations according to (F.5).

$$P_{50s} = \frac{P_{30} + P_{50} + P_{80}}{3} \qquad \text{(F.5a)}$$

$$P_{10s} = \frac{P_{6} + P_{8} + P_{10} + P_{13} + P_{17}}{5} \qquad \text{(F.5b)}$$

$$P_{3s} = \frac{P_{2.2} + P_{3} + P_{4}}{3} \qquad \text{(F.5c)}$$

$$P_{1s} = \frac{P_{0.7} + P_{1} + P_{1.5}}{3} \qquad \text{(F.5d)}$$

The long term index is calculated from a number of consecutive short-term flicker measurements according to (F.6);

$$P_{lt} = \sqrt[3]{\frac{1}{N}\sum_{k=1}^{N} P_{stk}^{3}} \qquad \text{(F.6)}$$

where N is the number of short-term 10-minute measurements needed for the long-term frame (typically 12).

A block diagram of the IEC flickermeter is shown in Figure F.1. More on the implementation of the IEC flickermeter in power system simulation packages can be found in [80, 81].

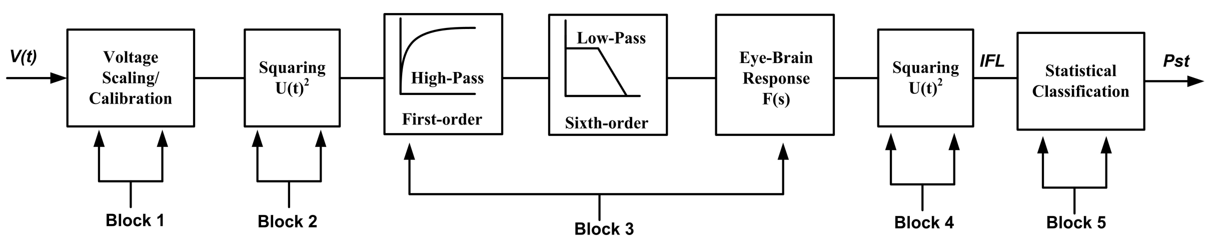

Figure F.1: IEC flickermeter block diagram.

Appendix G

IEC Flickermeter Model Validation

There is a number of extensive tests to be performed on the flickermeter based on the flickermeter intended use and application as outlined in [44]. The most salient of those tests were performed to ensure the compliance of the developed model. More specifically, the following tests were conducted: 1) test of response characteristic of the filters and scaling parameters ($Pinst$) and 2) test of classifier and statistical evaluation (Pst). The tests were performed by synthesizing a flicker-modulated voltage waveform undergoing voltage amplitude changes at different frequencies and corresponding amplitude variations and feeding it to the flickermeter. The modulation is done at different required depths depending on the frequency of modulation (smallest depth at the central frequency of 8.8 Hz). The first test is required to be done for both sinusoidal and rectangular modulation of the voltage waveform while the second is only required for rectangular modulation of the voltage waveforms. The test results and percentage errors are shown in Table G.1 and Table G.2 for the two tests respectively and with respect to the guidelines of [44]. The percentage error in the conducted tests is required to be less than 5 % in order to ensure the compliance of the flickermeter model.

Table G.1: Test of Response Characteristic of the Flickermeter Filters and Scaling Parameters

Hz	Percentage Voltage Fluctuation (Sinusoidal) ($\Delta V/V\%$)	Error in Conducted Test (%)	Percentage Voltage Fluctuation (Rectangular) ($\Delta V/V\%$)	Error in Conducted Test (%)
0.5	2.453	2.6108	0.598	1.5606
1	1.465	2.1289	0.548	1.4789
1.5	1.126	1.7597	0.503	1.4615
2	0.942	1.6445	0.469	1.3996
2.5	0.815	1.4740	0.439	1.2393
3	0.717	1.3750	0.419	1.1500
3.5	0.637	1.2907	0.408	1.1780
4	0.57	1.1893	0.394	1.4671
4.5	0.514	1.3037	0.373	1.4299
5	0.466	1.1707	0.348	1.0805
5.5	0.426	1.1660	0.324	1.0283
6	0.393	1.1887	0.302	1.1201
6.5	0.366	0.9481	0.283	0.9129
7	0.346	1.1290	0.269	0.8067
7.5	0.332	1.3197	0.258	0.7679
8	0.323	1.0064	0.253	0.7201
8.8	0.321	1.1343	0.252	1.4231
9.5	0.329	0.8724	0.258	0.8024
10	0.341	1.3907	0.266	1.4674
10.5	0.355	0.9152	0.278	0.9257
11	0.373	0.9263	0.292	0.6979
11.5	0.394	1.0778	0.308	1.2644
12	0.417	1.0201	0.324	1.0908
13	0.469	0.9841	0.367	0.9744

14	0.528	1.1383	0.411	0.9895
15	0.592	1.1088	0.457	0.9304
16	0.66	0.8443	0.509	0.7831
17	0.734	1.0719	0.575	1.0881
18	0.811	0.9786	0.626	0.9509
19	0.892	0.8812	0.688	0.8904
20	0.977	0.8059	0.746	0.8053
21	1.067	0.9301	0.815	0.9357
21.5	–	–	0.837	0.9748
22	1.160	0.8628	0.851	0.7663
23	1.257	0.8043	0.946	0.8334
24	1.359	0.8730	1.067	0.8737
25	1.464	0.7844	1.088	0.7995
25.5	–	–	1.072	0.9300
28	–	–	1.383	0.7374
30.5	–	–	1.602	0.8566
33.33	2.57	0.7791	1.823	0.8288
37	–	–	1.304	1.1134
40	4.393	0.8119	3.451	0.8846

Table G.2: Tests of Classifier and Statistical Evaluation

Rectangular Changes per Minute CPM	Percentage Voltage Fluctuation for One Unit of Pst ($\Delta V/V\%$)	Pst	Error in Conducted Test (%)
1	3.181	0.9835	-1.6517
2	2.564	0.9995	-0.0501
7	1.694	1.0013	0.1281
39	1.04	1.0003	0.0328
110	0.844	1.0049	0.4888
1620	0.548	1.0051	0.5087
4000	–	–	–
4800	4.837	1.0038	0.3794

By investigating the percentage error in the conducted tests, the IEC flickermeter developed model is seen to have fulfilled the IEC compliance requirements.

Appendix H

Standard Flicker Limits and Grid Codes

In Chapter 2, the standard WG flicker measurement procedure was outlined. This procedure provides an index representative of the measured flicker severity. That index helps the utilities identify the potential for a flicker problem. Yet, the measure of flicker severity from a utility perspective is physically the customer complaints signifying the presence of the problem. Those complaints seem to be received at slightly varying levels of flicker severity in different countries [82], but a general threshold of compatibility limits is assumed to be that indicated by both the IEEE and IEC standards. The MV compatibility levels provided in IEEE and IEC standards [13, 73] are shown in Table H.1. The compatibility level refers to the flicker severity at a point of customer supply above which customer complaints are received. The compatibility level of Table H.1 is assumed to be the same for all networks as it stands for the level that when exceeded, customer complaints are likely to be received, this is the level on which all planning levels and consequently wind farms emissions are implicitly based [83]. The limits and how they are assigned can be found in [73, 84, 74]. Conversely, the farm emission limit is network-specific and can vary between grid codes as long as the total flicker severity at electric power consumers ends respects the compatibility level. The generic limit recommended for an individual wind farm emission (as measured at the PCC) is given by the emission limits in Table H.2, [73].

Table H.1: Flicker Compatibility Levels

Pst	Plt
≤ 1	≤ 0.8

Table H.2: Emission Limits (Individual Wind Farm)

Pst	Plt
≤ 0.35	≤ 0.25

H.0.3 Wind Farm Flicker Limit Allocation

The flicker severity limit allocation to new wind farms is grid-code dependent and different approaches are observed in different countries regarding how flicker from new wind farms is dealt with. Some grid codes impose a maximum emission limit of that proposed in [73], others enforce stricter or looser limits. The Swedish guideline, for example, enforces the limits of Table H.3, [85].

Table H.3: Emission Limits in Sweden

Number of Wind Farms/Feeder	Emission Limit (Plt)
One farm	≤ 0.1
Several wind farms/ one feeder (maximum contribution)	≤ 0.25

Other grid codes adopt voltage-dependent limits. Denmark is a good example of relaxed limit on wind farm flicker emission in low-voltage networks, Table H.4, [86].

Table H.4: Emission Limits in Denmark

Interconnection Voltage (kV)	Emission Limit (Plt)
≤ 35	0.5
> 35	0.35

It is also possible that a size-dependent flicker allocation approach is implemented. This helps relieve the size constraints on the wind farm with regard to power quality regulations. An example of that is the situation observed in France, the French distribution network operators enforce the emissions of [73] up to a wind farm rating of 5 MW, above which a linear increase in flicker permissible limits is allowed up to a rated value of 12 MW above which a maximum level of Pst of 0.44 must be maintained, Table H.5, [87].

Table H.5: Emission Limits in France

Size of Wind Farm (MW)	Emission Level (Pst)
≤ 5	≤ 0.35
> 5	Linear increase with a maximum limit of 0.44

The limit on the flicker emission of new wind farms can therefore be theoretically relaxed or tightened as long as customer complaints are to be avoided by respecting the compatibility limits at points of electric power consumers connection. In other words, the flicker absorption capacity of a given network can be regarded as a pie of a permissible flicker quantity of which both flicker-emitting loads and generators have their shares and based on which the need for flicker mitigation at a flicker source point of connection is ascertained, Figure H.1. Figure H.1 shows two situations (assuming a linear addition of Pst for ease of illustration) in which wind power can be admitted without the request for flicker mitigation (a), and with the request for flicker mitigation (b) where the connected flicker sources already have a significant share of the network flicker absorption capacity.

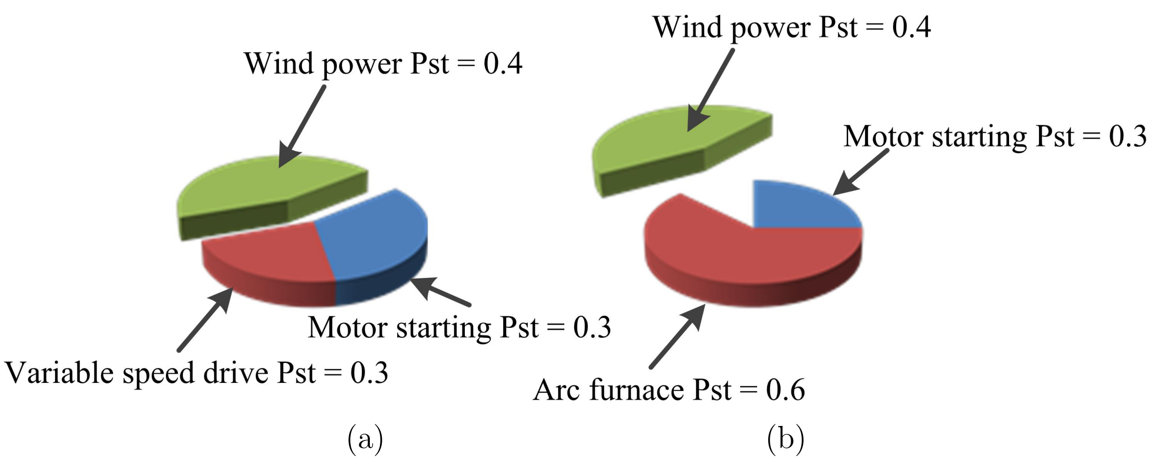

Figure H.1: Flicker limit allocation pie (Pst is assumed to have a linear addition for ease of illustration): (a) network flicker sources allow for the wind power flicker contribution to be accommodated, (b) network flicker sources do not allow for the wind power flicker contribution to be accommodated while maintaining the compatibility levels.

Appendix I

Grid-Integration Parametric Studies

Utilizing the superior computational capabilities of the real-time simulator, the site characteristics and the assumed wind farm layout impact on Pst values were evaluated on the real-time model for the integration of 10 MW of wind power at Bus 16 of the detailed distribution network of Figure 2.4. More specifically, the following studies were performed:

1. Study of the effect of wind turbines spacing and the equivalent impact on wind speed turbulence and corresponding generated active power and flicker severity. The intention here was just to show how the flicker values may be affected by the layout of the wind farm. Figure I.1 shows the impact of spacing the wind turbines by 100 m on equivalent wind speed, assuming a wind speed average of 10 m/s and shifting the wind speed data at each turbine by the time it takes to travel from one turbine to another. The resultant wind speed (average summation of wind data at all individual turbines) is shown to be of increasingly lower dispersion (standard deviation) as the number of turbines increases. The calculated equivalent turbulence intensity reduces from 0.15 for lumped production of 10 MW (five turbines) to 0.095 with the assumed spatial displacement of the turbines. The total active power production from the wind farm is shown in Figure I.2 for both cases and the Pst values are shown for all simulated cases as the number of turbines increases in Figure I.3.

2. Study of the increase of the size of connected wind power capacity. This is shown for both cases of lumped and spaced wind power production in Figure I.3. The

increase in Pst values is shown to be subtler in case of the spaced turbines when compared to lumped wind power production fed by a single wind speed profile.

3. Study of the change of wind turbulence intensity. The impact of changing wind turbulence intensity and assuming lumped production of wind power was studied for four different values of turbulence intensity (0.1, 0.15, 0.25 and 0.3). The effect of varying the wind turbulence intensity is reflected on the wind power production profiles as seen in Figure I.4. The resulting Pst values are shown in Figure I.5.

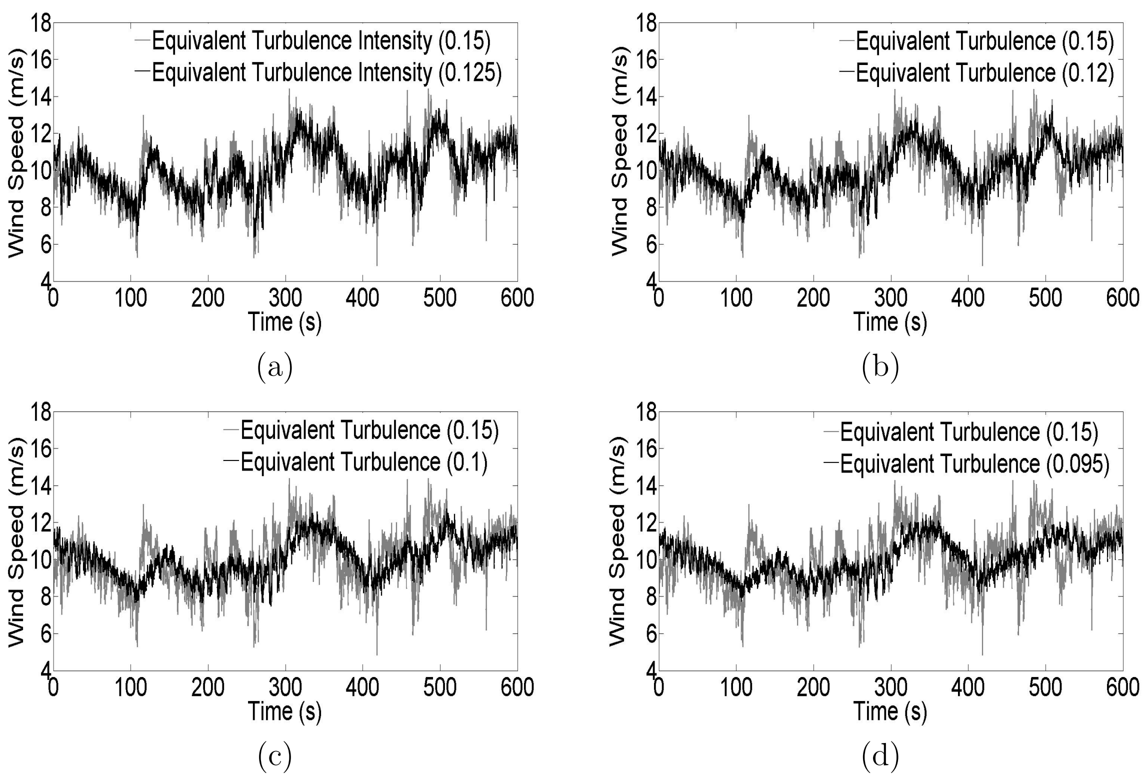

Figure I.1: Effect of wind turbines spacing on equivalent wind speed and turbulence intensity (lumped production vs. spaced production): (a) two turbines, (b) three turbines, (c) four turbines, (d) five turbines.

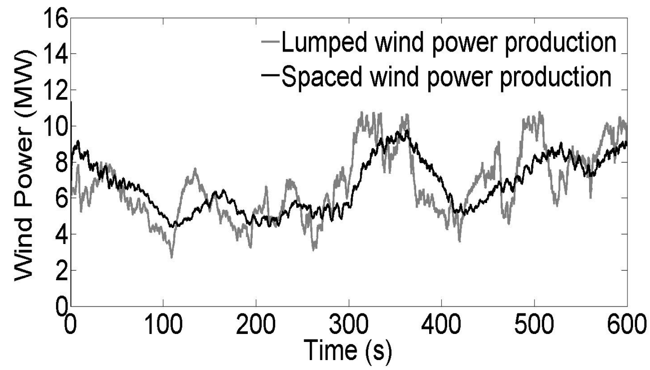

Figure I.2: Active power generation for a 10 MW wind farm (lumped vs. spaced wind power production).

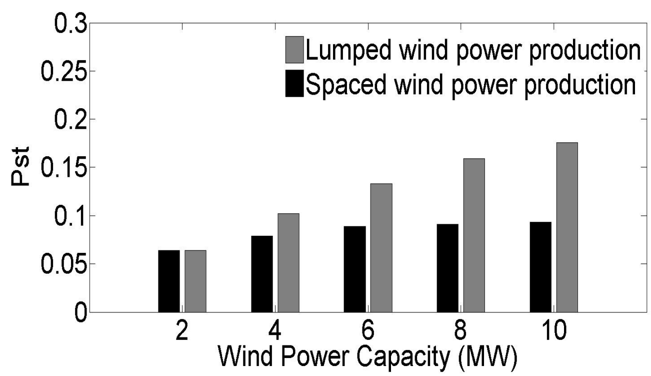

Figure I.3: Pst values for lumped and spaced wind power production.

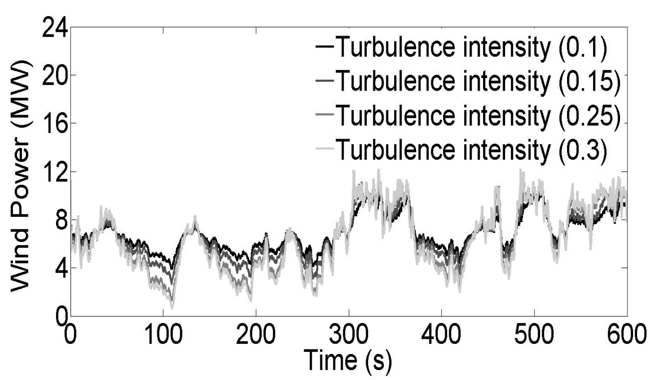

Figure I.4: Wind power production under varying levels of turbulence intensity.

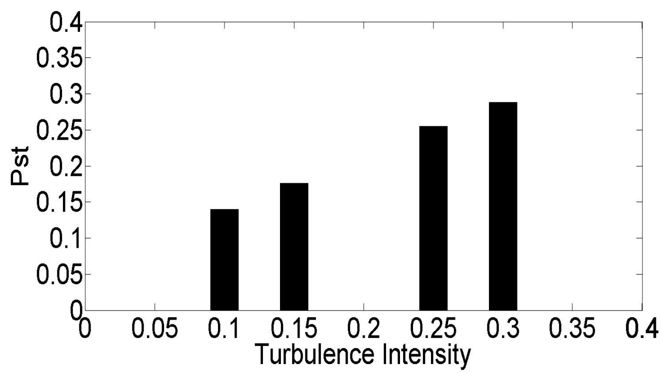

Figure I.5: Pst values at the connection bus as the turbulence intensity changed.

Appendix J

Publications

Journal Papers

- Moataz Ammar, Geza Joos, “A short-term energy storage system for voltage quality improvement in distributed wind power,” *IEEE Trans. Energy Convers,* vol. 29, no. 4, pp. 997-1007, Dec., 2014.

- Moataz Ammar, Geza Joos, “The impact of distributed wind generators reactive power behavior on flicker severity,” *IEEE Trans. Energy Convers,* vol. 28, no. 2, pp. 425-433, Jun., 2013.

Conference Papers

- Moataz Ammar, Geza Joos, “Flicker Mitigation Planning Solutions in Distributed Wind Power: A Real-Time Simulation Analysis,” *in Proc. IEEE International Conference on Renewable Energy Research and Applications (ICRERA)*, 2014.

- Moataz Ammar, Geza Joos, “Combined active/reactive power control for flicker mitigation in distributed wind power,” *in Proc. IEEE Energy Conversion Congress and Exposition (ECCE)*, 2012, pp. 3161-3167.

- Moataz Ammar, “Flicker emission of distributed wind power: a review of impacts, modeling, grid codes and mitigation techniques,” *in Proc. IEEE PES General Meeting*, 2012, pp. 1-7.

- Moataz Ammar, Philippe Venne, Chad Abbey, Geza Joos, “A methodology for assessing the impact of distributed wind power on voltage flicker,” *Cigre International Symposium on the Electric Power System of the Future*, 2011.

Bibliography

[1] J. Lopes, N. Hatziargyriou, J. Mutale, P. Djapic, and N. Jenkins, "Integrating distributed generation into electric power systems: A review of drivers, challenges and opportunities," *Electric Power Systems Research*, vol. 77, no. 9, pp. 1189–1203, 2007.

[2] A. Keane and M. O'Malley, "Impact of distributed generation capacity on losses," in *Power Engineering Society General Meeting, IEEE*, 2006.

[3] "*http://www.wwindea.org/*," World Wind Energy Association, 2014.

[4] N. Hadjsaid, J.-F. Canard, and F. Dumas, "Dispersed generation impact on distribution networks," *Computer Applications in Power, IEEE*, vol. 12, no. 2, pp. 22–28, 1999.

[5] L. Tang, A. Yan, L. Marti, and J. Fuerth, "Hydro one distribution voltage performance design criteria and power distance test in enabling distributed generation," in *2012 IEEE PES Transmission and Distribution Conference and Exposition (T&D)*, pp. 1–8, IEEE, 2012.

[6] P. P. Barker and R. W. de Mello, "Determining the impact of distributed generation on power systems. i. radial distribution systems," in *Power Engineering Society Summer Meeting, 2000. IEEE*, vol. 3, pp. 1645–1656, IEEE, 2000.

[7] J. Peas Lopes, "Integration of dispersed generation on distribution networks-impact studies," in *Power Engineering Society Winter Meeting, 2002. IEEE*, vol. 1, pp. 323–328, IEEE, 2002.

[8] F. D. Kanellos and N. Hatziargyriou, "The effect of variable-speed wind turbines on the operation of weak distribution networks," *IEEE Transactions on Energy Conversion*, vol. 17, no. 4, pp. 543–548, 2002.

[9] A. De Moura and A. De Moura, "Analysis of injected apparent power and flicker in a distribution network after wind power plant connection," *IET Renewable Power Generation*, vol. 2, no. 2, pp. 113–122, 2008.

[10] T. Ackermann, A. Ellis, J. Fortmann, E. Muljadi, R. Piwko, P. Pourbeik, E. Quitmann, U. H. Sorensen, P., and B. Zavadil, "Code shift: grid specifications and dynamic wind turbine models," *IEEE Power and Energy Magazine*, vol. 11, no. 6, pp. 72–82, 2013.

[11] J. von Appen, T. Stetz, M. Braun, and A. Schmiegel, "Local voltage control strategies for pv storage systems in distribution grids," *IEEE Transactions on Smart Grids*, vol. 5, no. 2, pp. 1002–1009, 2014.

[12] H. Sugihara, K. Yokoyama, O. Saeki, K. Tsuji, and T. Funaki, "Economic and efficient voltage management using customer-owned energy storage systems in a distribution network with high penetration of photovoltaic systems," *IEEE Transactions on Power Systems*, vol. 28, no. 1, pp. 102–111, 2013.

[13] "*IEEE Recommended Practice-Adoption of IEC 61000-4-15:2010 Electromagnetic Compatibility (EMC)-Testing and Measurement Techniques-Flickermeter-Functional and Design Specifications*," IEEE Standard 1453-2011, 2011.

[14] T. Abdel-Galil, E. EL-Saadany, and M. Salama, "Online tracking of voltage flicker utilizing energy operator and hilbert transform," *IEEE Transactions on Power Delivery*, vol. 19, no. 2, pp. 861–867, 2004.

[15] S. Bhattacharyya, S. Cobben, J. Myrzik, and W. Kling, "Flicker propagation and emission coordination study in a simulated low voltage network," *European Transactions on Electrical Power*, vol. 20, no. 1, pp. 52–67, 2010.

[16] S. Bhattacharyya, J. Myrzik, W. Kling, and S. Cobben, "Estimation of the planning levels for flicker in the dutch networks," in *10th International Conference on Electrical Power Quality and Utilisation, 2009. EPQU 2009.*, pp. 1–6, IEEE, 2009.

[17] R. Cai, J. Cobben, J. Myrzik, J. Blom, and W. Kling, "Flicker responses of different lamp types," *IET Generation, Transmission & Distribution*, vol. 3, no. 9, pp. 816–824, 2009.

[18] L. Peretto, L. Rovati, G. Salvatori, R. Tinarelli, and A. E. Emanuel, "Investigation on the response of the human eye to the light flicker produced by different lamps," in *Proceedings of the IEEE Instrumentation and Measurement Technology Conference, 2006. IMTC 2006.*, pp. 37–42, IEEE, 2006.

[19] T. Dionise, "Assessing the performance of a static var compensator for an elecric arc furnace," *IEEE Transactions on Industry Applications*, vol. 50, no. 3, pp. 1619–1629, 2014.

[20] T. Sun, Z. Chen, and F. Blaabjerg, "Flicker mitigation of grid connected wind turbines using statcom," in *Second International Conference on Power Electronics, Machines and Drives (PEMD 2004), 2004.*, pp. 175–180, IET, 2004.

[21] R. Walling, K. Clark, N. Miller, and J. Sanchez-Gasca, "Advanced controls for mitigation of flicker using doubly-fed asynchronous wind turbine-generators," in *18th International Conference and Exhibition on Electricity Distribution, 2005. CIRED 2005.*, pp. 1–5, IET, 2005.

[22] J. Duval, G. Delille, J.-L. Fraisse, and X. Guillaud, "Contribution of local voltage regulation to a better insertion of dg in distribution grids," in *20th International Conference and Exhibition on Electricity Distribution-Part 1, 2009. CIRED 2009.*, pp. 1–4, IET, 2009.

[23] T. Sun, Z. Chen, and F. Blaabjerg, "Flicker study on variable speed wind turbines with doubly fed induction generators," *IEEE Transactions on Energy Conversion*, vol. 20, no. 4, pp. 896–905, 2005.

[24] Y.-S. Kim and D.-J. Won, "Mitigation of the flicker level of a dfig using power factor angle control," *IEEE Transactions on Power Delivery*, vol. 24, no. 4, pp. 2457–2458, 2009.

[25] M. Kayikci and J. V. Milanovic, "Reactive power control strategies for dfig-based plants," *IEEE Transactions on Energy Conversion*, vol. 22, no. 2, pp. 389–396, 2007.

[26] R. Aghatehrani and R. Kavasseri, "Reactive power management of a dfig wind system in microgrids based on voltage sensitivity analysis," *IEEE Transactions on Sustainable Energy*, vol. 2, no. 4, pp. 451–458, 2011.

[27] L. Meegahapola, B. Fox, and D. Flynn, "Flicker mitigation strategy for dfigs during variable wind conditions," in *Power and Energy Society General Meeting, 2010 IEEE*, pp. 1–8, IEEE, 2010.

[28] W. Hu, Z. Chen, Y. Wang, and Z. Wang, "Flicker mitigation by active power control of variable-speed wind turbines with full-scale back-to-back power converters," *IEEE Transactions on Energy Conversion*, vol. 24, no. 3, pp. 640–649, 2009.

[29] A. Uehara, A. Pratap, T. Goya, T. Senjyu, A. Yona, N. Urasaki, and T. Funabashi, "A coordinated control method to smooth wind power fluctuations of a pmsg-based wecs," *IEEE Transactions on Energy Conversion*, vol. 26, no. 2, pp. 550–558, 2011.

[30] Y. Zhang, Z. Chen, W. Hu, and M. Cheng, "Flicker mitigation by individual pitch control of variable speed wind turbines with dfig," *IEEE Transactions on Energy Conversion*, vol. 29, no. 1, pp. 20–28, 2014.

[31] A. Larsson, "Flicker emission of wind turbines during continuous operation," *IEEE Transactions on Energy Conversion*, vol. 17, no. 1, pp. 114–118, 2002.

[32] H. Emanuel, M. Schellschmidt, S. Wachtel, and S. Adloff, "Power quality measurements of wind energy converters with full-scale converter according to iec 61400-21," in *10th International Conference on Electrical Power Quality and Utilisation, 2009. EPQU 2009.*, pp. 1–7, IEEE, 2009.

[33] E. Muljadi, N. Samaan, V. Gevorgian, J. Li, and S. Pasupulati, "Different factors affecting short circuit behavior of a wind power plant," *IEEE Transactions on Industry Applications*, vol. 49, no. 1, pp. 284–292, 2013.

[34] T. Thiringer, T. Petru, and S. Lundberg, "Flicker contribution from wind turbine installations," *IEEE Transactions on Energy Conversion*, vol. 19, no. 1, pp. 157–163, 2004.

[35] "*Wind turbine grid connection and interaction, European communities,*," Deutsches Windenergie-Institut GmbH Germany, Tech-wise A/S Denmark, DM Energy United Kingdom, Tech. Rep., 2001.

[36] "*Wind Turbine Generator Systems Part 21: Measurement and Assessment of Power Quality Characteristics of Grid Connected Wind Turbines*," IEC Standard 614000-21, 2001.

[37] B. Ni and C. Sourkounis, "Influence of wind-energy-converter control methods on the output frequency components," *IEEE Transactions on Industry Applications*, vol. 45, no. 6, pp. 2116–2122, 2009.

[38] B. Ni and C. Sourkounis, "Energy yield and power fluctuation of different control methods for wind energy converters," *IEEE Transactions on Industry Applications*, vol. 47, no. 3, pp. 1480–1486, 2011.

[39] V. Akhmatov, H. Knudsen, and A. H. Nielsen, "Advanced simulation of windmills in the electric power supply," *International Journal of Electrical Power & Energy Systems*, vol. 22, no. 6, pp. 421–434, 2000.

[40] I. P. Girsang, J. S. Dhupia, E. Muljadi, M. Singh, and L. Pao, "Gearbox and drive-train models to study dynamic effects of modern wind turbines," *IEEE Transactions on Industry Applications*, vol. PP, no. 99, p. 1, 2014.

[41] D. S. Dolan and P. W. Lehn, "Simulation model of wind turbine 3p torque oscillations due to wind shear and tower shadow," *IEEE Transactions on Energy Conversion*, vol. 21, no. 3, p. 717, 2006.

[42] X. Kong, Z. Zhang, X. Yin, and M. Wen, "Study of fault current characteristics of the dfig considering dynamic response of the rsc," *IEEE Transactions on Energy Conversion*, vol. 29, no. 2, pp. 278–287, 2014.

[43] J. Hu, J. Zhu, and D. Dorrell, "A new control method of cascaded brushless doubly fed induction generators using direct power control," *IEEE Transactions on Energy Conversion*, vol. 29, no. 3, pp. 771–779, 2014.

[44] "*Electromagnetic Compatability (EMC) Part 4: Testing and Measurement Techniques-Section 15: Flickermeter Functional and Design Specifications*," IEC Standard 61000-4-15, 2003.

[45] A. Hooshyar and E. F. El-Saadany, "Development of a flickermeter to measure non-incandescent lamps flicker," *IEEE Transactions on Power Delivery*, vol. 28, no. 4, pp. 2103–2115, 2013.

[46] G. Wiczynski, "Inaccuracy of short-term light flicker p_{st} indicator measuring with a flickermeter," *IEEE Transactions on Power Delivery*, vol. 27, no. 2, pp. 842–848, 2012.

[47] C. Chen, Y. Chen, Y. Chang, and Y. Lee, "An accurate solution procedure for calculation of voltage flicker components," *IEEE Transactions on Industrial Electronics*, vol. 61, no. 5, pp. 2370–2377, 2014.

[48] C. Albistur, P. Aravena, L. Moran, and J. Espinoza, "A simple predictive method to estimate flicker," in *2013 IEEE Industry Applications Society Annual Meeting*, pp. 1–7, IEEE, 2013.

[49] A. Hooshyar, M. A. Azzouz, and E. F. El-Saadany, "Addressing iec flickermeter deficiencies by digital filtration inside a sliding window," *IEEE Transactions on Instrumentation and Measurement*, vol. 62, no. 9, pp. 2476–2491, 2013.

[50] A. Keane, L. F. Ochoa, E. Vittal, C. J. Dent, and G. P. Harrison, "Enhanced utilization of voltage control resources with distributed generation," *IEEE Transactions on Power Systems*, vol. 26, no. 1, pp. 252–260, 2011.

[51] "*Requirements for the Interconnection of Distributed Generation to the Hydro-Qubec Medium-Voltage Distribution System*," Hydro Québec Distribution, 2009.

[52] M. Sujod, I. Erlich, and S. Engelhardt, "Improving the reactive power capability of the dfig-based wind turbine during operation around the synchronous speed," *IEEE Transactions on Energy Conversion*, vol. 28, no. 3, pp. 736–745, 2013.

[53] M. Ammar and G. Joós, "Impact of distributed wind generators reactive power behavior on flicker severity," *IEEE Transactions on Energy Conversion*, vol. 28, no. 2, pp. 425–433, 2013.

[54] F. Sharkey, J. MacEnri, E. Bannon, M. Conlon, and K. Gaughan, "Resource-induced voltage flicker for wave energy converters- assessment tools," *IET Renewable Power Generation*, vol. 7, no. 6, pp. 623–630, 2013.

[55] G. O. Cimuca, C. Saudemont, B. Robyns, and M. M. Radulescu, "Control and performance evaluation of a flywheel energy-storage system associated to a variable-speed wind generator," *IEEE Transactions on Industrial Electronics*, vol. 53, no. 4, pp. 1074–1085, 2006.

[56] W. Li, G. Joós, and J. Bélanger, "Real-time simulation of a wind turbine generator coupled with a battery supercapacitor energy storage system," *IEEE Transactions on Industrial Electronics*, vol. 57, no. 4, pp. 1137–1145, 2010.

[57] C. Abbey and G. Joos, "Supercapacitor energy storage for wind energy applications," *IEEE Transactions on Industry Applications*, vol. 43, no. 3, pp. 769–776, 2007.

[58] A. M. Gee, F. V. Robinson, and R. W. Dunn, "Analysis of battery lifetime extension in a small-scale wind-energy system using supercapacitors," *IEEE Transactions on Energy Conversion*, vol. 28, no. 1, pp. 24–33, 2013.

[59] P. Thounthong, "Model based-energy control of a solar power plant with a supercapacitor for grid-independent applications," *IEEE Transactions on Energy Conversion*, vol. 26, no. 4, pp. 1210–1218, 2011.

[60] D. Recalde Melo and L.-R. Chang-Chien, "Synergistic control between hydrogen storage system and offshore wind farm for grid operation," *IEEE Transactions on Sustainable Energy*, vol. 5, no. 1, pp. 18–27, 2014.

[61] W. Li and G. Joós, "Performance comparison of aggregated and distributed energy storage systems in a wind farm for wind power fluctuation suppression," in *IEEE Power Engineering Society General Meeting, 2007.*, pp. 1–6, IEEE, 2007.

[62] L. Qu and W. Qiao, "Constant power control of dfig wind turbines with supercapacitor energy storage," *IEEE Transactions on Industry Applications*, vol. 47, no. 1, pp. 359–367, 2011.

[63] T. K. Brekken, A. Yokochi, A. Von Jouanne, Z. Z. Yen, H. M. Hapke, and D. A. Halamay, "Optimal energy storage sizing and control for wind power applications," *IEEE Transactions on Sustainable Energy*, vol. 2, no. 1, pp. 69–77, 2011.

[64] Q. Li, S. Choi, Y. Yuan, and D. Yao, "On the determination of battery energy storage capacity and short-term power dispatch of a wind farm," *IEEE Transactions on Sustainable Energy*, vol. 2, no. 2, pp. 148–158, 2011.

[65] J. Slootweg, S. De Haan, H. Polinder, and W. Kling, "General model for representing variable speed wind turbines in power system dynamics simulations," *IEEE Transactions on Power Systems*, vol. 18, no. 1, pp. 144–151, 2003.

[66] C. Nichita, D. Luca, B. Dakyo, and E. Ceanga, "Large band simulation of the wind speed for real time wind turbine simulators," *IEEE Transactions on Energy Conversion*, vol. 17, no. 4, pp. 523–529, 2002.

[67] J. P. Barton and D. G. Infield, "Energy storage and its use with intermittent renewable energy," *IEEE Transactions on Energy Conversion*, vol. 19, no. 2, pp. 441–448, 2004.

[68] C. Abbey, K. Strunz, and G. Joós, "A knowledge-based approach for control of two-level energy storage for wind energy systems," *IEEE Transactions on Energy Conversion*, vol. 24, no. 2, pp. 539–547, 2009.

[69] A. Esmaili, B. Novakovic, A. Nasiri, and O. Abdel-Baqi, "A hybrid system of li-ion capacitors and flow battery for dynamic wind energy support," *IEEE Transactions on Industry Applications*, vol. 49, no. 4, pp. 1649–1657, 2013.

[70] R. Wamkeue, N. Kandil, J. East, and Y. Boisclair, "Series compensation for a hydro-quebec long distribution line," in *International Conference on Renewable Energies Power Quality (ICREPQ)*, pp. 9–11, 2004.

[71] T. Orchi, M. Hossain, H. Pota, and M. Rahman, "Impact of distributed generation and series compensation on distribution network," in *2013 8th IEEE Conference on Industrial Electronics and Applications (ICIEA)*, pp. 854–859, IEEE, 2013.

[72] A. Pashaie, B. Zahawi, and D. Giaouris, "Distributed static series compensation for distribution network line voltage profile improvement," in *2011 2nd IEEE PES International Conference and Exhibition on Innovative Smart Grid Technologies (ISGT Europe)*, pp. 1–4, IEEE, 2011.

[73] "*Electromagnetic compatibility (EMC) - Part 3-7: Limits - Assessment of emission limits for the connection of fluctuating installations to MV, HV and EHV power systems*," IEC Standard 61000-3-7, 1996.

[74] S. Tennakoon, L. Perera, D. Robinson, and S. Perera, "Flicker transfer in radial power systems," in *Australasian Universities Power Engineering Conference (AUPEC 2004)*, 2004.

[75] S. Perera, D. Robinson, S. Elphick, D. Geddey, N. Browne, V. Smith, and V. Gosbell, "Synchronized flicker measurement for flicker transfer evaluation in power systems," *IEEE Transactions on Power Delivery*, vol. 21, no. 3, pp. 1477–1482, 2006.

[76] S. Heier, *Grid Integration of Wind Energy Conversion Systems.* New York, USA: Wiley Sons, 2006.

[77] W. Li, G. Joós, and C. Abbey, "Attenuation of wind power fluctuations in wind turbine generators using a dc bus capacitor based filtering control scheme," in *Conference Record of the 2006 IEEE Industry Applications Conference, 2006. 41st IAS Annual Meeting.*, vol. 1, pp. 216–221, IEEE, 2006.

[78] W. Li, G. Joós, and C. Abbey, "Wind power impact on system frequency deviation and an ess based power filtering algorithm solution," in *IEEE PES Power Systems Conference and Exposition, 2006. PSCE'06.*, pp. 2077–2084, IEEE, 2006.

[79] J. A.E. Fitzgerald, Charles Kingsley and S. D. Umans, *Electric Machinery.* New York, USA: McGraw-Hill, 2003.

[80] L. W. White and S. Bhattacharya, "A discrete matlab–simulink flickermeter model for power quality studies," *IEEE Transactions on Instrumentation and Measurement*, vol. 59, no. 3, pp. 527–533, 2010.

[81] A. Bertola, G. Lazaroiu, M. Roscia, and D. Zaninelli, "A matlab-simulink flickermeter model for power quality studies," in *11th International Conference on Harmonics and Quality of Power, 2004.*, pp. 734–738, IEEE, 2004.

[82] M. Halpin, R. Cai, E. De Jaeger, I. Papic, S. Perera, and X. Yang, "A review of flicker objectives related to complaints, measurements, and analysis techniques," in *20th International Conference and Exhibition on Electricity Distribution-Part 1, 2009. CIRED 2009.*, pp. 1–4, IET, 2009.

[83] R. Horton and T. A. Haskew, "Effect of transfer coefficients on mv and lv flicker levels," *IEEE Transactions on Power Delivery*, vol. 26, no. 2, pp. 632–639, 2011.

[84] "*Electromagnetic compatibility (EMC) -Part 2-2: Environment Compatibility levels for low-frequency conducted disturbances and signalling in public low-voltage power supply systems*," IEC Standard 61000-2-2, 2002.

[85] A. Ekberg and J. Hasselstrom, "Design critera for electrical networks upon installation of wind power production," in *20th International Conference and Exhibition on Electricity Distribution-Part 1, 2009. CIRED 2009.*, pp. 1–4, IET, 2009.

[86] "*Technical regulation for a power 3.2.5 for wind power plants with a power output greater than 11 kW*," Energinet, 2010.

[87] X. Yang and J. Gauthier, "How can flicker level be determined before a customer is connected to the electric grid," in *IEEE Power & Energy Society General Meeting, 2009. PES'09.*, pp. 1–6, IEEE, 2009.